


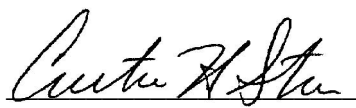
A Numerical Study of the Sensitivity of Cloudy-Scene Bidirectional Reflectivity Distribution Functions to Variations in Cloud Parameters


by
Pierre V. Villeneuve

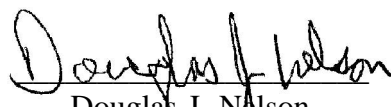
Dissertation submitted to the Faculty of the
Virginia Polytechnic Institute and State University
in partial fulfillment of the requirements for the degree of
Doctor of Philosophy
in
Mechanical Engineering

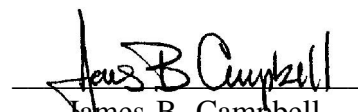
APPROVED


J. Robert Mahan, Chairman


Curtis H. Stern


Elaine P. Scott


Douglas J. Nelson


James B. Campbell

June 28, 1996
Blacksburg, Virginia

**A Numerical Study of the Sensitivity of Cloudy-Scene
Bidirectional Reflectivity Distribution Functions
to Variations in Cloud Parameters**

by

Pierre V. Villeneuve

J. Robert Mahan, Chairman

Mechanical Engineering

(Abstract)

The goal of this research has been to characterize the sensitivity of the earth's shortwave bidirectional reflectivity distribution function (BRDF) to variations in cloud parameters. The BRDF is a remote sensing tool used to predict the flux reflected from a given earth scene from a satellite-based measurement of the reflected intensity. The BRDF is necessary in order to account for the anisotropic nature of the shortwave radiation field. A shortwave atmospheric radiation Monte-Carlo ray-trace model has been developed as part of this research to predict the earth-reflected radiation field at the top of the atmosphere. This model was developed while paying special attention to clouds including realistic three-dimensional cloud fields characterized by fundamental physical properties. This model was used to predict the BRDF for various cloud fields where a single cloud parameter was varied as part of the sensitivity analysis. The results show that the shortwave BRDF is very sensitive to changes in cloud vertical thickness and mean cloud size. This sensitivity is also strongly dependent on the direction from which the scene is observed. In a related analysis, a study was done of the error associated with using a BRDF from one scene to retrieve fluxes from a second scene. The model was also used to predict images of cloud fields for comparison with experimental data from the Rutherford Appleton Laboratories satellite-based Along Track Scanning Radiometer (ATSR). Finally the output from the radiation model was integrated with the end-to-end radiative electrothermal model of a practical earth radiation budget instrument. This integrated model was used to predict the instrument response to scanning a realistic partly-cloudy earth scene.

Acknowledgements

I would like to thank Professor J. Robert Mahan for being my research advisor and friend through the years of my education in Blacksburg. His enthusiasm and openness have made my graduate studies a very rewarding experience.

I would also like to thank the other members of my advisory committee who have invested time and interest in my work over the years. Professors Elaine Scott, Douglas Nelson, and James Campbell have all helped me with advice on the various research problems I have encountered. I would especially like to thank Curt Stern for serving on my Ph.D. committee. He was my advisor for my M.S. degree and has given me invaluable counsel as I continued on with my doctoral work. I also want to thank Lou Smith who was both my mentor and backyard neighbor during the summer I worked at NASA Langley Research Center.

I am deeply indebted to my fellow graduate students who have enriched my life. Rob Bongiovi, Tai Nguyen, Kory Priestley, Jeff Turk, Michael Walkup and Stephanie Weckmann have been great friends and office-mates. I thank Martial Haeffelin for being my friend in Blacksburg and in France. I also thank Edward Nelson for being an excellent friend and co-worker since the very beginning.

None of this would have been possible without my family. I thank my mother and my father for the encouragement they have freely given and the confidence they have instilled in me over the years. I thank my brothers and my sister for being my life-long companions. I have never laughed so hard as when I was with them.

Table of Contents

Abstract	ii
Acknowledgements	iii
Table of Contents	iv
List of Tables	viii
List of Figures	ix
Nomenclature	xii
Chapter 1 Introduction	1
1.1 The Global Environment	1
1.2 The Nature of the Earth's Radiation Budget	2
1.3 Earth Radiation Budget Measurement History	5
1.3.1 Pre-Satellite Era	5
1.3.2 Early Satellite Missions	5
1.3.3 Earth Radiation Budget Experiment (ERBE)	7
1.3.4 Clouds and the Earth's Radiant Energy System (CERES) Experiment	8
1.4 Remote Sensing Issues	9
1.4.1 What is the Bidirectional Reflectivity Function?	10
1.4.2 ERBE and CERES Scene Types	11
1.5 BRDF Sensitivity Analysis	14
Chapter 2 Literature Review	15
2.1 Clouds and Climate	15
2.2 Cloud Modeling Efforts	17
2.3 Radiation Field Anisotropy	19
Chapter 3 Atmospheric Radiation Theory	21
3.1 Gaseous Radiative Heat Transfer	21

3.1.1	Attenuation of Radiation by Absorption and Scattering	21
3.1.2	Emission of Radiation by a Gaseous Medium	22
3.1.3	Augmentation of Radiation by Scattering	23
3.1.4	Equation of Radiative Heat Transfer	23
3.2	Application to Shortwave Atmospheric Radiation Problems	26
3.2.1	Atmospheric Absorption	27
3.2.2	Rayleigh Scattering	27
3.2.3	Mie Scattering	28
3.2.4	Aerosols	30
3.2.5	Scattering by Ice Crystals in High-Altitude Cirrus Clouds	30
3.2.6	Surface Absorption and Reflection	31
3.2.7	Equation of Radiative Transfer Applied to Shortwave Atmospheric Radiation	32
3.3	Review of Various Solution Methods	33
3.3.1	The P-N (Differential) Method	33
3.3.2	The Discrete Ordinate Method	34
3.3.3	The Finite Element Method	35
3.3.4	The Monte-Carlo Ray-Trace Method	35
Chapter 4	Model Description	38
4.1	Grid Systems	38
4.1.1	Atmospheric Grid	38
4.1.2	Top-of-the-Atmosphere Spatial Grid	39
4.1.3	Top-of-the-Atmosphere Angular Grid	40
4.2	The Earth's Surface	40
4.2.1	Surface Absorption	41
4.2.2	Surface Reflection	42
4.3	Cyclic Boundary Conditions	44
4.4	Rayleigh Scattering	44
4.4.1	Extinction Coefficient	45
4.4.2	Phase Function	45

4.5 Clouds	47
4.5.1 Cloud Shape Array	48
4.5.2 Cloud Element Scattering Phase Function	48
4.5.3 Cloud Morphology from Landsat Data	52
4.6 TOA Radiation Field from Ray-Trace Results	52
4.7 Model Validation	53
4.7.1 TOA Flux Convergence	53
4.7.2 BRDF Convergence	54
4.7.3 Cloud Control Volume Optimum Size	56
4.8 Spectral Limitations	58
4.9 Random Number Generator	59
4.10 Computer Requirements	59
 Chapter 5 Acceleration Techniques	 61
5.1 Line-Surface Intersections	61
5.1.1 Intersection Point of a Line with an Infinite Surface	61
5.1.2 Does an Intersection Point Exist Within a Finite Surface?	63
5.2 Earth Surface Reflection Evaluation	64
5.3 Fractional Absorption	65
5.4 Cloud Element Phase Function Evaluation	67
5.5 Cloud Bounding Box Intersection	69
5.6 Cloud Placement Pre-Processing	71
 Chapter 6 Results	 74
6.1 Cloud Size Sensitivity Analysis	74
6.1.1 Cloud Size Variation	74
6.1.2 Albedo Sensitivity	77
6.1.3 BRDF Sensitivity	78
6.2 Optical Thickness Sensitivity Analysis	80
6.2.1 Albedo Sensitivity	80

6.2.2 BRDF Sensitivity	82
6.3 Scene Misidentification Error	83
6.3.1 Misidentified Cloud Size	84
6.3.2 Misidentified Cloud Optical Thickness	84
6.4 Model Comparison with the Along Track Scanning Radiometer	85
6.4.1 ATSR Data Sets	86
6.4.2 Reproduction of Cloud Field from ATSR Nadir View	87
6.4.3 Model Results and Comparison with ATSR Forward View	87
6.5 Integration of the Atmospheric Radiation Model with the CERES	
End-to-End Dynamic Electrothermal Instrument Model	90
6.5.1 Mosaic Scene Construction	91
6.5.2 Scene Analysis for Input into Instrument Model	93
6.5.3 Instrument Response	95
Chapter 7 Conclusions and Recommendations	97
7.1 Conclusions	97
7.2 Recommendations for Future Work	99
7.2.1 Model Improvements	99
7.2.2 Further Studies	100
Tables	103
Figures	118
References	163
Vita	173

List of Tables

Table 1	The ERBE 12-scene classification scene	104
Table 2	Typical cloud water droplet size characteristics	105
Table 3	Ray-trace model acceleration technique results	106
Table 4	Cloud element media property variation for cloud thickness sensitivity study	107

List of Figures

Figure 1.1	Schematic of the earth-atmosphere system showing the major components of the earth radiation budget	109
Figure 1.2	Spherical coordinate system defining the position of an observer relative to the solar plane	110
Figure 3.1	Intensity normally incident on an absorbing and scattering volume elements of thickness dS	111
Figure 3.2	Rayleigh scattering phase function versus scattering angle	112
Figure 3.3	Mie scattering phase function versus scattering angle	113
Figure 4.1	Monte-Carlo ray-trace model of the atmosphere including three-dimensional clouds, the ocean surface and atmospheric scattering	114
Figure 4.2	Three-dimensional atmospheric grid system	115
Figure 4.3	Top of the atmosphere (TOA) two-dimensional spatial grid system	116
Figure 4.4	TOA angular grid system with divisions in zenith (θ) and azimuth (ϕ) angular directions	117
Figure 4.5	Ocean surface albedo as a function of incident zenith angle and wind speed	118
Figure 4.6	Ocean surface BRDF for wind speed of 5 m/s with solar zenith angles of (a) 30 deg and (b) 60 deg	119
Figure 4.7	Example of cyclic boundary condition at side walls of atmosphere showing ray copied from point 1 to point 2 with change in direction	120
Figure 4.8	Rayleigh scattering coefficient versus altitude in the atmosphere.	121
Figure 4.9	Single-scattering event local coordinate system defined by incoming vector	122
Figure 4.10	Typical three-dimensional cloud composed of a large number of identical cubic elements, or cloud building blocks	123

Figure 4.11	Two-dimensional representation of cloud element angular discretization showing (a) the incoming bins and (b) the outgoing bins	124
Figure 4.12	Cloud element multiple-scattering phase function showing the proportion of energy leaving the six faces for two different incident angles (a) and (b) corresponding to the similarly labelled vectors in (c)	125
Figure 4.13	A typical ray trace through filled and empty cloud elements . . .	126
Figure 4.14	Typical Landsat data showing cloud optical thickness	127
Figure 4.15	Example of four clouds extracted from the Landsat image data of Figure 4.14	128
Figure 4.16	Cloud field used for TOA flux, BRDF symmetry, and cloud element size convergence	129
Figure 4.17	Albedo convergence as a function of the number of rays traced for ten separate sets of random number generator seeds .	130
Figure 4.18	BRDF convergence as a function of the number of rays traced for ten separate sets of random number generator seeds .	131
Figure 4.19	Convergence of the scene albedo as the cloud element size is refined	132
Figure 5.1	Basis vector definition for determining whether or not a point exists within the boundaries of a finite surface	133
Figure 5.2	Convergence comparison between discrete ray absorption and fractional ray absorption	134
Figure 5.3	Definition of (a) the sphere around CBB and (b) vector geometry for cloud-ray intersection acceleration technique	135
Figure 5.4	Atmospheric 3 by 3 grid system superimposed on the cloud field of Figure 4.16 for cloud placement acceleration technique	136
Figure 5.5	Illustration of (a) the number of clouds per atmospheric control volume and (b) the corresponding model performance	137
Figure 6.1	The eight scenes used in the cloud size sensitivity study with	

	35 percent cloud cover and 45 deg solar zenith angle	138
Figure 6.2	An example of the extremes in cloud size variation with (a) maximum and (b) minimum cloud-to-cloud interaction	139
Figure 6.3	Extraction of cloud morphology from Landsat imagery and simplification to eliminate horizontal variations of vertical thickness	140
Figure 6.4	Cloud number density distribution for various mean cloud diameters	141
Figure 6.5	Albedo versus mean cloud diameter for 35 percent cloud cover, 45 deg solar angle and an ocean surface	142
Figure 6.6	BRDF results for variation of mean cloud size for 35 percent cloud cover, 45 deg solar angle and an ocean surface	143
Figure 6.7	Limb brightening implies that view B is "brighter" than view A	144
Figure 6.8	(a) BRDF sensitivity to cloud size and (b) correlation coefficient for 35% cloud cover, 45 deg solar zenith angle and ocean surface	145
Figure 6.9	Scene (a) albedo and (b) albedo sensitivity to optical thickness as a function of mean cloud optical thickness for 35 percent cloud cover, 45 deg solar angle and an ocean surface	146
Figure 6.10	BRDF results for variation in mean cloud optical thickness for 35 percent cloud cover, 45 deg solar angle and an ocean surface	147
Figure 6.11	(a) BRDF sensitivity parameter and (b) correlation coefficient for 35 percent cloud cover, 45 deg solar angle and an ocean surface	148
Figure 6.12	Flux retrieval error with cloud size variation for 35 percent cloud cover, 45 deg solar angle and an ocean surface	149
Figure 6.13	Flux retrieval error for cloud optical thickness variation for 35 percent cloud cover, 45 deg solar angle and an ocean surface . .	150
Figure 6.14	The ATSR earth-viewing geometry	151
Figure 6.15	ATSR imager data showing (a) cloud height from 11 μ m thermal	

	channel and (b) the forward view from the 0.55 μm channel . .	152
Figure 6.16	Construction of a cloud from ATSR cloud-top height information	153
Figure 6.17	The (a) ATSR cloud field and (b) the corresponding model cloud field showing cloud bounding boxes (CBB)	154
Figure 6.18	Predicted reflected flux distribution from ATSR model cloud field	155
Figure 6.19	Virtual screen geometry showing (a) ray passing through screen pixel and (b) arriving at the TOA grid through (c) a radiation field angular bin (c)	156
Figure 6.20	Comparison of (a) ATSR forward view with (b) corresponding model-predicted view (b)	157
Figure 6.21	Five cloud scenes used to create larger mosaic scene	158
Figure 6.22	Mosaic scene constructed from sequences of individual scenes .	159
Figure 6.23	Schematic representation of a radiometer scanning a 500-km earth scene from three different 800 km altitude orbital positions	160
Figure 6.24	Power fields incident to instrument aperture from TOA position of 425 km input to the CERES optical model from orbits (a) 1 and (b) 3	161
Figure 6.24	(a) Equivalent incident intensity and (b) calibrated instrument response	162

Nomenclature

Symbols:

ATSR	Along track scanning radiometer
BRDF	Bidirectional reflectivity distribution function
CBB	Cloud bounding box
D	Mean cloud diameter (km)
D_{ij}	Distribution factor from element i to element j
FEM	Finite element method
i	Intensity or radiance ($\text{W}/\text{m}^2/\text{sr}$)
I	Radiation source term
L	Path length (m)
P	Phase function, Ray point of emission
Q	Flux (W/m^2), Ray point of absorption
R	Bidirectional reflectivity distribution function
r_{eff}	Mie scattering particle distribution effective radius (μm)
TOA	Top of the atmosphere
u	Optical thickness
v_{eff}	Mie scattering particle distribution effective variance
V	Ray vector

Greek:

θ	Zenith angle (deg)
λ	Wavelength (μm)
σ	Extinction coefficient ($1/\text{m}$)
ϕ	Azimuth angle (deg)
Φ	Phase function
ω	Albedo
Ω	Single-scattering albedo

Subscripts

i	Zenith angle index (incident)
j	Azimuth angle index (incident)
k	Zenith angle index (outgoing)
l	Azimuth angle index (outgoing)
n	Cloud index number
surf	Cloud element face number

Chapter 1 Introduction

1.1 The Global Environment

Our civilization has been the single most important force in recent geologic history to affect changes on our planet. Many of the problems we see today in the environment can be directly or indirectly linked to some form of industrialization. It is now well established among the international earth science community that adequate understanding of the long-term impact of such problems can only be achieved through multi-disciplinary studies of the earth. Engineers and scientists must recognize that the oceans and atmosphere play critical roles in the earth's ecosystem in order to fully comprehend the impact of interlocking natural and human processes on the present and future global environment.

Ahrens (1991) discusses some general issues relating climate and the earth's radiation budget. In spite of inaccuracies that plague earth temperature measurements, several studies indicate that for the past one-hundred years or so, the earth has undergone a slight warming of about 0.5°C. Modern general circulation models predict that if such warming should continue unabated, we are irrevocably committed to some measure of climate change, possibly a shifting of the world's wind patterns that steer the rain-producing storms across the globe.

Some scientists believe that the main cause for such global warming is the increasing concentration of the greenhouse gas carbon dioxide (CO₂). This increase is due in part to the burning of fossil fuels and deforestation. However, in recent years, increasing concentrations of other gases, such as methane (CH₄), nitrous oxide (N₂O), and chlorofluorocarbons (CFCs), has been shown to have an effect equal to that of increasing CO₂. A particular CFC (CFC-12) absorbs very strongly in the atmospheric window between 8 and 11 μm. In terms of its absorption impact on infrared radiation, Ahrens (1991) also concludes that the addition of a single CFC-12 molecule to the atmosphere is equivalent to adding 10,000 molecules of CO₂.

Presently, the concentration of CO_2 in a volume of air near the surface is about 0.03 percent by volume of dry atmosphere. Various climate models predict that doubling this amount will cause the earth's average surface temperature to rise between about 2 K and 5 K. These models also predict that rising ocean temperatures will cause an increase in evaporation rates. This added water vapor (the primary greenhouse gas) will enhance the atmospheric greenhouse effect and enhance the temperature rise in a positive feedback effect. This increased water vapor will also result in more clouds, which are potentially the largest and least understood feedback system in the earth's climate. Clouds vary in size, shape, thickness, and physical properties simultaneously with climatic changes. Studies indicate that clouds in general have an overall cooling effect on the earth's climate, as they reflect and radiate away more energy than they absorb. Thus an increase in atmospheric water vapor might bring about an increase in global cloudiness, and an increase in global cloudiness might thereby offset some of the global warming brought on by an enhanced atmospheric greenhouse effect. The net effect of all these changes in both the atmosphere and clouds is not well understood.

1.2 The Nature of the Earth's Radiation Budget

It is important to understand that the sole manner in which the earth can realize a change in temperature is through a radiative exchange of energy with its surroundings. No media exist beyond the earth to allow for conduction or convection heat transfer. Thus radiation transfer between the earth and the hot sun or between the earth and cold outer space are the only potential mechanisms for change in the earth's mean temperature. The large difference in the earth's effective temperature of 255 K and the sun's temperature of 5800 K enables the earth radiation budget (ERB) components to be viewed in two separate regions of the electromagnetic spectrum. The solar energy absorbed and reflected by the earth occurs primarily in the shortwave region between the wavelengths 0.1 and 5.0 μm , with a peak at 0.55 μm . This includes the visible spectrum. The earth-emitted thermal energy is concentrated in the thermal spectrum between 5.0 and 120 μm , with a peak at 10 μm . Other sources of energy such as geothermal energy are negligible when compared to the incident solar radiation and earth-emitted thermal radiation (Kandel, 1994).

The earth radiation budget is a balance between three components, as indicated in Figure 1.1. The solar radiation arriving at the earth in the shortwave spectrum is the primary component. A fraction of the solar energy is absorbed by clouds, the atmosphere and the surface of the earth. The fraction of solar radiation reflected and scattered back into space is the second component. The third component is the fraction of thermal energy emitted by clouds and the earth's surface which escapes to space. The sum of the reflected-solar and earth-emitted components must equal the incident solar radiation in order to achieve a balanced budget. If the budget is not balanced, then the earth's mean temperature will either increase or decrease.

The three earth radiation budget components may be affected by various factors. The flux of solar energy arriving at the earth is known as the solar constant, q_0 , and its value is currently accepted to be 1367.9 W/m^2 . However the solar constant is not truly a constant. The actual value of the solar flux is strongly affected by the 11-year sun spot cycle which can cause variations of up to several percent. Little observational basis exists and inadequate theoretical tools are available for accurately estimating the variability of the sun over very longer time scales. This is a recognized source of uncertainty in attempts to understand the past or to predict the future and for this reason it is important to continuously measure the solar flux. The fraction of the solar energy reflected back to space (and thus also the fraction absorbed by the earth) is greatly affected by a range of atmospheric and surface properties. The most important of these are the changes associated with the variations of clouds. Clouds are very reflective of solar energy, and any significant change in the earth's cloud field distribution will have a corresponding impact on the earth radiation budget. The earth-emitted thermal radiation component is also very sensitive to cloud cover since the cloud temperature, and thus the amount of emitted radiation, varies quite significantly with cloud altitude. Low fair-weather cumulus clouds will be only slightly cooler than the earth's surface, whereas high-altitude cirrus clouds will be extremely cold and will emit only a small fraction of the thermal radiation emitted by the low clouds. As a result of all this, cloud variations are the dominant force affecting variations in the earth radiation budget.

An example of the sensitivity of the earth's mean temperature to the earth's ability to reflect and absorb radiation is given by Barkstrom (1982). We may qualitatively assume that the earth is a painted iron ball, for which the absorbed shortwave radiation P_{abs} , is given by

$$P_{abs} = \pi R^2 (1 - \omega) q_o, \quad (1-1)$$

and the emitted thermal radiation, $P_{emitted}$, is given by

$$P_{emitted} = 4 \pi R^2 \sigma T^4. \quad (1-2)$$

In these expressions, R is the radius of the earth, ω is the global mean albedo, q_o is the solar constant, T is an equilibrium temperature of the earth, and σ is the Stefan-Boltzmann constant. If the absorbed power is equated to emitted power in the above equations, then the equilibrium temperature is calculated to be about 255 K. Further, a one percent increase in the solar constant produces a 0.25-percent increase in the equilibrium temperature (0.64 K). Likewise, an increase in the global mean albedo of one percent produces a 0.36-percent decrease in equilibrium temperature (0.91 K). To a certain extent these sensitivities give an indication of how accurately the reflected and emitted components of the earth's radiation budget must be measured.

However the connection between the earth's surface temperature and the equilibrium temperature just considered is quite complex. One indication of this complexity is provided by the fact that the mean temperature of the earth's surface is considerably higher than the equilibrium temperature calculated above. In fact, this equilibrium temperature corresponds to an atmospheric temperature at an altitude of about 5 km.

1.3 Earth Radiation Budget Measurement History

1.3.1 Pre-Satellite Era

At the beginning of the 1960's (Hunt et al., 1986), the advent of the space age, we had reached the position where radiative models were capable of providing estimates of the global and zonally averaged components of the radiation budget. The accuracy of these results was, of course, dependent upon the accuracy of the data describing the physical parameters used in the model, associated with the clouds, solar radiation, and the gaseous atmospheric absorbers. In the 60 years since the early 1900's estimates of the global albedo had been reduced from 89 to 30 percent, but major uncertainties still existed in the estimated parameters. Presumptuously, the energy from the sun had been named the solar constant. However, the determination of the precise value, which is crucial for the radiation budget studies, was still far too inaccurate. Early researchers were also aware of the critical importance of the effect of clouds. For example, Abbot (1920) remarked the following regarding the matter of clouds and the earth radiation budget: "The matter is so fundamental to the proper understanding of the temperature of the world and its dependence on the balance of radiations of the sun and the earth that it warrants careful attention. It is hardly possible to overestimate the importance of this neglected branch of meteorology."

1.3.2 Early Satellite Missions

Liu (1992) discusses the history of early satellite observation of the earth radiation budget. The ERB at the top of the atmosphere has been derived from satellite observations since the beginning of the meteorological satellite era. Four factors have influenced the evolution of ERB instrumentation: (1) spacecraft limitations of power, data storage, mode of stabilization, and attitude control; (2) viewing angles of nonscanning and scanning medium- and high-resolution radiometers; (3) spectral band-pass requirements; and (4) on-board calibration. The first-generation ERB instruments included black and white hemispherical sensors using thermistor

detectors to measure the sensor temperature on board the first U.S. meteorological satellite, Explorer 6, launched February 17, 1959 (Suomi, 1957).

In the second generation of satellite missions during the 1960's and 1970's, sun-synchronous orbits became possible with more powerful rockets, and provided the opportunity for daily global coverage of the earth. The duration of spacecraft measurements extended to several years. Flat nonscanning radiometers were installed on several early research and operational satellites and, later, medium and wide field-of-view radiometers were also deployed on the National Oceanographic and Atmospheric Administration (NOAA) satellites. Medium- and high-resolution infrared radiometers were used on Nimbus 2 (1966) and 3 (1969) and contained five-channel medium resolution scanning radiometers. These provided the first observations of the ERB for the entire globe. The aperture field-of-view of the Nimbus radiometers is about 2.5 deg, resulting in a spatial resolution of about 50 km at nadir and about 110 km at a viewing zenith angle of 40 deg. Spectral band-pass filters for these radiometers were 0.3 to 4.0 μm for shortwave and 5 to 50 μm for longwave. The computation of outgoing fluxes from measured radiances required conversion of measured filtered intensities to intensities covering the entire solar and thermal infrared spectra, integration over all angles of measurements using bidirectional reflectivity distribution functions (BRDF), and estimation of the average flux over a twenty-four-hour period using diurnal models. The NOAA polar orbiting satellites performed scanning measurements in the visible and infrared window regions. The transformation of these narrow-spectral-interval data into broadband flux estimates required numerous assumptions and models. Valuable data sets have been constructed from the narrowband measurements of ERB components.

The third generation of satellite observational systems led to the development of ERB instruments that measured direct incident shortwave solar radiation, reflected shortwave radiation, and emitted longwave radiation. The Nimbus 6 (1975) and 7 (1978) satellites contained wide field-of-view and scanning radiometers that provided valuable observations of the ERB. The scanning measurements observed the bidirectional and directional reflecting and emitting properties of the earth-atmosphere system varying in both time and space. These were also

important in developing bidirectional and directional models for the conversion of observed intensities to fluxes.

The longest record of solar constant measurements was assembled from Nimbus 7 observations. The sun-synchronous polar-orbiting satellites observed each earth location at a fixed local sun time. As a consequence, the observations were insufficient to provide a more detailed quantitative estimate of the temporal and spatial sampling errors. Studies of the ERB using data from geostationary satellites were especially useful, because they provided a regular sample of the atmospheric diurnal cycle. This enabled a wide range of spatial and temporal radiation variations to be investigated. Observations from GOES and METEOSAT satellites have been used in numerous studies of the ERB. Radiometers on board geostationary satellites were confined to narrow spectral bands and had spatial nadir resolutions that varied from about 0.5 km to 10 km.

1.3.3 Earth Radiation Budget Experiment (ERBE)

The fourth generation of ERB studies involved the Earth Radiation Budget Experiment (ERBE) (Barkstrom et al., 1982). This experiment consists of a series of three satellites to monitor the monthly ERB in detail and to complete our understanding of the diurnal variation. The design strategy of the experiment incorporated both old and new technology concepts. The Earth Radiation Budget Satellite (ERBS) was launched into a prograde orbit that precessed westward daily. Observations from ERBS completed a diurnal cycle of sampling at a given latitude every 36 days. The NOAA-9 and NOAA-10 satellites complement the ERBS measurements in their sun-synchronous orbits with both afternoon and morning equator crossings during the daytime period.

The ERBE platforms comprise two instrument suites. One contains a scanner with three detectors to measure shortwave radiation (0.2 to 5.0 μm), longwave (5 to 50 μm), and total radiation (0.2 to 50 μm) (Kopia and Lee, 1990). The detectors of these instruments are thermistor bolometers located just behind the focal plane of a Caissegrain telescope. The field-

of-view is hexagonal, with an angular size of 3×4.5 deg, or 30×45 km on the surface of the earth at nadir. The scanning motion is from limb to limb in the plane perpendicular to the orbit track. The scanner instruments operated, respectively, until January, 1987, on NOAA-9; May, 1989, on NOAA-10; and February, 1990, on ERBS, providing more than two years of overlapping data with two satellites and four months with three satellites. The second ERBE instrument suite contains four nonscanning earth-viewing detectors. Two of these are wide field-of-view, observing the earth from limb to limb, and two are medium field-of-view, observing a circular footprint approximately 1000 km in diameter. For each of the two fields of view, there is a shortwave channel (0.2 - 5.0 μm) and a total channel (0.2 - 50 μm). The longwave component is obtained from the difference between these two channels.

1.3.4 Clouds and the Earth's Radiant Energy System (CERES) Experiment

The next generation of ERB satellite missions, the Clouds and the Earth's Radiant Energy System (CERES) experiment, is one of the highest priority scientific satellite instruments being developed for NASA's Mission to Planet Earth Program. This observation program is critical for providing a scientific understanding of ongoing natural and human-induced global changes and for providing a sound scientific basis for developing global environmental policies. CERES will measure both earth-reflected solar energy and earth-emitted thermal energy. A primary objective will be the determination of cloud properties including amount, height, thickness, particle size, and water phase with help from simultaneous measurements by other instruments. All of these measurements are critical for understanding cloud-radiation climate change and improving the ability to predict global warming using climate models.

As discussed in Section 1.2, clouds can cause either cooling or heating of the earth. Much more information is needed about clouds and radiation and their role in climate change. The largest uncertainty in climate prediction models is how to characterize and parameterize the radiative and physical properties of clouds. Cloud modeling is one of the weakest links in the chain of current climate models used to predict potential global climate change.

Four important objectives of the CERES program are:

1. Provide a continuation of the ERBE record of radiative fluxes at the top of the atmosphere (TOA), analyzed using the same algorithms that produced the existing ERBE data product.
2. Double the accuracy of radiative flux estimates at the TOA and at the earth's surface.
3. Provide the first long-term global estimates of the radiative fluxes within the earth's atmosphere.
4. Provide cloud property estimates which are consistent with the radiative fluxes from the earth's surface to the TOA.

CERES flight plans include a launch on the Tropical Rainfall Measuring Mission (TRMM) in 1997, followed by a launch on the Earth Observing System (EOS)-AM satellite in 1998 and the EOS-PM satellite in 2000. Follow-up CERES satellite missions are planned to create a continuous 15-year history of highly accurate radiation and cloud data for climate analyses.

1.4 Remote Sensing Issues

This section deals with an important remote sensing tool necessary for interpreting satellite measurements of earth reflected shortwave energy. The work to be described in this dissertation concerns the shortwave (0.1 - 5.0 μm) portion of the electromagnetic spectrum. Thus any later discussion about intensity or flux should be assumed to be shortwave unless otherwise noted.

1.4.1 What is the Bidirectional Reflectivity Distribution Function?

The scanning radiometers used in each of the earth radiation budget missions discussed above measure the intensity, or radiance, i ($\text{W}/\text{m}^2/\text{sr}$) of radiation arriving at the instrument from a particular scene on the surface of the earth. This reflected intensity will vary quite significantly with the direction from which the scene is observed, which poses a problem since the quantity needed for ERB studies is the reflected flux q (W/m^2) of radiation leaving the scene. It is important to realize that the flux represents the energy reflected from a scene in all directions of hemispherical space, and that the intensity is a measure only of the energy passing through a limited solid angle. The flux reflected from a scene can be determined by integrating the reflected intensity over all observing angles of the hemispherical space above the scene,

$$q(\theta_o) = \int_0^{2\pi} \int_0^{\pi/2} i(\theta_o, \theta, \phi) \cos \theta \sin \theta d\theta d\phi, \quad (1-3)$$

where θ_o is the solar zenith angle, θ is the viewing zenith angle measured from the vertical, and ϕ is the relative azimuth angle between the observer and the sun. These angles are defined in Figure 1.2, which shows the observing direction in relation to the sun. Note that the measured intensity i is a function of both viewing angles as well as the solar zenith angle. An anisotropic function R is defined as

$$R(\theta_o, \theta, \phi) \equiv \frac{i(\theta_o, \theta, \phi)}{q(\theta_o)/\pi}, \quad (1-4)$$

which is also a function of the solar and viewing zenith angles, and the relative azimuth angle. This quantity is also known as the Bidirectional Reflectivity Distribution Function (BRDF) and is used to characterize the relative anisotropy of the reflected radiation field. The BRDF may be considered the intensity i reflected in a particular direction normalized by the intensity a diffuse surface reflecting the same hemispherical power would have reflected in the same direction.

The BRDF is an important remote sensing tool used to predict the shortwave flux reflected from a scene based on a measurement of the intensity reflected in a particular satellite viewing direction. A measurement of the intensity i can be processed to the scene-reflected flux as

$$q(\theta_o) = \frac{\pi i(\theta_o, \theta, \phi)}{R(\theta_o, \theta, \phi)}. \quad (1-5)$$

Thus, in order to obtain reflected flux results from a particular scene intensity measurement, an *a priori* BRDF is needed for that particular scene. This is a very important concept, since the earth's surface and its atmosphere are infinite in the number of possible scene types they can produce. However, for any type of earth observation experiment, the earth can only be represented with a limited number of scene types which attempt to take into account the different reflecting properties between land, ocean and snow. Also, the condition of the atmosphere, in particular the clouds in the atmosphere, plays the most important role of all in defining the shortwave reflecting characteristics of the earth-atmosphere system.

1.4.2 ERBE and CERES Scene Types

In early satellite missions (Hunt et al., 1986), the BRDF was assumed to be isotropic and the radiation field was assumed to be homogenous across large areas of the earth. Later, new observations and more advanced modelling efforts broadened the knowledge and understanding of the angular properties of reflected shortwave radiation fields and allowed better estimates of the BRDF. The range of errors resulting from the isotropic approximation may be estimated by examining the variation of the BRDF. Nimbus 7 ERB observations indicated that the variation of the BRDF is quite large and that the range in BRDF increases significantly as the solar zenith angle increases. For example, at a 60-deg zenith angle the BRDF ranges from 0.65 to 1.35 for an average azimuth angle of view but increases from 0.60 to 2.25 in the forward scattering plane. Thus current-generation BRDFs may be in error by a factor of two or more when used to

determine shortwave fluxes. Accurate bidirectional models are clearly needed for the interpretation of remote intensity measurements by scanning radiometers.

Table 1 shows the scene classification scheme used for ERBE. The BRDFs for each of these scenes represent the current state-of-the-art (Suttles et al., 1988, 1989). Note the lack of accounting for cloud properties other than the fractional cloud cover. For each of these scenes the BRDF is defined in each viewing direction for each solar zenith angle. For each of the twelve scene categories, these models describe the anisotropy of the top-of-the-atmosphere radiation field as a function of solar zenith angle, viewing zenith angle, and relative azimuth angle. These models have been derived primarily from intensities measured by the Nimbus 7 scanner and GOES instruments, which operated between late 1978 and 1980. Missing and sparsely sampled observed quantities were estimated by a variety of techniques, including simple linear and bilinear interpolation, linear extrapolation, the reciprocity principle and radiative transfer model results.

The upcoming CERES mission will require a new generation of BRDFs. The BRDFs used for ERBE are not adequate for CERES for two reasons. First, the ERBE models describe all of the cloud anisotropic effects with only four coarse cloud cover classes. This choice was dictated in part by the scene identification process which was based only on the ERBE longwave and shortwave measurements (Wielicki and Green, 1989). The ERBE processing system was self-sufficient and used no ancillary data for flux retrieval. The second reason the ERBE models are not adequate for CERES is the inherent biases in the BRDFs. The purpose of the BRDFs is to account for the anisotropy of the earth's radiation field so that fluxes can be estimated independent of viewing geometry. However, post-flight analysis (Suttles et al., 1992) of ERBE data has shown that the estimated shortwave albedo systematically increases with viewing zenith angle and the estimated longwave flux decreases with viewing zenith. It is generally accepted that the ERBE BRDFs underestimate both longwave limb-darkening and shortwave limb-brightening.

An important goal of CERES is to reduce the flux retrieval error associated with the BRDFs by a factor of one-fourth. From this it was determined that a reasonable number of CERES scene types is about 200 (Green et al., 1994). Where ERBE modelled only cloud cover, in the shortwave CERES will model cloud cover plus visible optical depth, particle size, and cloud-top height. In the longwave, CERES will model cloud cover, cloud emissivity, cloud height, column water vapor, lapse rate, and surface emissivity. The 200 scene types in both the shortwave and longwave represent a discretization of these parameters.

The new CERES BDRFs will be developed from CERES-measured intensity data. This follows from the fact that the measured data must be classified and sorted according to the cloud types within its field-of-view so that scene-dependent BDRFs can be constructed. This full cloud characterization will only become available with CERES, where a full complement of ancillary data together with a library of remote-sensing algorithms will be used to identify the particular scene in the field-of-view. Once the field-of-view is identified the data will be sorted into scene types and accumulated over a period of time to determine the mean models in the presence of natural variation. The twelve ERBE models were built with 205 days of Nimbus-7 data and constructed over a four-year period. The 200 CERES models will require two to three years to collect.

The CERES scene types still remain to be refined to their final state. An initial set of parameters has been defined; however, the resulting number of scene types is still much more than 200. The parameters with the strongest effect on anisotropy must receive further discretization while those with weak or no effect can be grouped together. This can be done by studying the sensitivity of the BRDF to each of the scene parameters. It is desired to use a scene classification scheme which will allow for the highest accuracy in the retrieved fluxes. This means that scene parameters must be chosen carefully to account for variations in BRDF with scene parameters. Parameters to which scene BDRFs are highly sensitive have the potential of introducing errors into the flux retrieval process.

1.5 BRDF Sensitivity Analysis

The goal of the research reported in this dissertation is to study of the effect of varying marine cumulus and stratocumulus cloud properties on the anisotropy of the earth's reflected shortwave radiation field. In particular, the BRDF sensitivity to mean horizontal cloud size and cloud vertical optical thickness were studied. This was accomplished by first developing a modular three-dimensional Monte-Carlo ray-trace model of the earth's atmosphere with special allowances for realistically shaped clouds. This model has been used to predict the shortwave radiation field at the top of the earth's atmosphere given the physical and morphological properties of the cloud field. The sensitivity analysis is performed by calculating the BRDF from the model-predicted radiation for various cloud field configurations, where the parameter of interest is varied between test cases.

Chapter 2 Literature Review

2.1 Clouds and Climate

Clouds are known as the main modulator of the earth's reflected radiation field and consequently they have a very substantial impact on the climate. Thanks to satellite remote sensing techniques, the effect of clouds on the radiation budget at the top of the atmosphere may seem easiest to quantify. The cloud effect is two-fold. First, clouds are very efficient at reflecting incident solar radiation back to space. Secondly, in the longwave, clouds absorb thermal radiation emitted by the earth's surface and lower atmosphere and reradiate to space at a colder temperature, thereby producing a net heating effect. The balance between these two competing effects depends on a variety of conditions such as the regional distribution and seasonal variation of cloud properties.

The role of clouds in climate sensitivity calculations was analyzed in some detail by Schneider (1972), who considered the sensitivity of the radiation budget to fractional cloud cover. Since this time there have been many attempts to determine this sensitivity from satellite observations (Cess, 1976; Ohring and Clapp, 1980; Hartmann and Short, 1980). The results ranged from a net cancellation of shortwave and longwave effects to a strong shortwave albedo dominant effect. These results illustrate the potentially large radiative influence of clouds on climate. Such large discrepancies also shed some light on the difficulties in estimating the climate sensitivity. It is difficult, if not impossible, to isolate variations in reflected radiation due solely to a single parameter variation using purely observational techniques.

Charlock and Ramanathan (1985) more recently proposed that this problem should be examined with the concept of cloud radiative forcing. This is defined as the difference between the earth-reflected and earth-emitted flux from a scene with clouds present and the flux from a similar scene without clouds. Thus a positive value of cloud forcing implies that the presence of clouds has caused a net increase in the amount of energy absorbed by the earth. From the point of view of remote-sensing observations, it appears easier to estimate the cloud radiative

forcing from the difference between the overall (clear sky and cloudy) mean fluxes and the mean clear-sky fluxes, rather than from the estimation of cloud fraction and other parameters such as cloud albedo, cloud height, cloud top temperature, and emission (Hartmann et al., 1986; Ramanathan et al., 1989a, 1989b). The availability of regional estimates of clear-sky fluxes in the processed ERBE data allows for an empirical estimate of the cloud radiative forcing. From the ERBE data available for the month of August 1985, Ramanathan et al. (1989b) found a global shortwave cloud forcing of -44.5 W/m^2 and a longwave cloud forcing of 31.3 W/m^2 . The net effect is thus a cooling of -13.3 W/m^2 . For the month of July, 1985, Ramanathan (1989b) found a net cloud cooling effect of -16.6 W/m^2 .

Various climate models exhibit considerable disagreement regarding the magnitudes of shortwave and longwave cloud forcing terms. Even the sign of the net forcing is not certain, although most results are negative, ranging from 0 to -40 W/m^2 (Cess and Potter, 1988; Cess et al., 1989). The attempts at predicting the satellite-measured cloud radiative forcing reveals clearly the inadequacy of current cloud modelling efforts. It should be noted that accurate determination of cloud radiative forcing is only the first step in evaluating the climate-cloud-radiation feedback loop, since this feedback system also includes the reaction of cloud cover and cloud characteristics to climate forcing. It is then hardly surprising that there should be a fairly wide range in the predictions of climate sensitivity to changes such as a doubling of atmospheric CO_2 . Model comparisons (Cess et al., 1989) show that the major source of uncertainty is in the treatment of cloud radiative effects. Since the role played by cloud-to-cloud radiative interactions is so important in the various processes of the climate system, it is of utmost importance that they be adequately taken into account in three-dimensional atmospheric models.

Parol et al. (1994) have shown through an extensive field experiment that in the real world the influence of clouds on atmospheric radiation depends on many factors including water (or ice) content, cloud microphysical properties such as particle shape and size distribution, and on cloud morphology, spatial distribution and orientation. Their results indicate that neglect of cloud shape can lead to an overestimation of longwave emitted flux. In the shortwave they note that it can lead to an overestimation of reflected flux for low solar zenith angles but depends

strongly on cloud cell orientation for high solar zenith angles. Stephens and Greenwald (1991) have also recently shown that cloud morphology is likely to have a larger impact on the earth radiation budget than cloud microphysics. Thus it is very important to quantify and parameterize the influence of cloud inhomogeneities on the radiation field.

Given the delicate balance between clouds and climate, small systematic errors in characterizing the radiative behavior of clouds may be quite significant. Since cloudiness is known to exhibit heterogeneities at many spatial scales, the most obvious limitations in the current modelling efforts lie in using the plane-parallel hypothesis. This is an approach where the atmosphere is assumed to be one-dimensional and composed of many horizontally infinite plane-parallel layers. This method has become very popular in the recent past because of its simplicity; however, it is inherently unable to model many important features such as the radiative properties of broken cloud fields.

2.2 Cloud Modelling Efforts

Relaxing the plane-parallel cloud modelling idealization raises serious problems with regard to both realistic descriptions of broken cloud fields and the calculation of their radiative properties, particularly at visible wavelengths. Experimental investigation of the statistical morphology of real cloud fields shows a wide range of conditions (Plank, 1969). From detailed analysis of high-resolution imagery it is possible to determine the number density of cloud cells as a function of their mean dimension (Welch and Wielicki, 1986; Wielicki and Welch, 1986). However, a conceptual framework for fully describing statistically the variability of cloud shapes, sizes, and spatial organization is still lacking.

Solutions of the radiative transfer problem with geometry other than the usual plane-parallel one are difficult, and accurate and fast techniques do not exist yet. Exact methods (Preisendorff and Stephens, 1984) and analytical treatments based on the Eddington approximations (Davies, 1978; Gube et al., 1980) have been developed. These solutions may provide valuable benchmarks, and they are efficient at investigating the influence of some cloud

parameters. However, they have been developed only for isolated clouds with simple cuboid geometries, and their extension to other geometries and cloud fields is by no means immediate. Therefore most studies of radiative transfer in finite clouds have been based on numerical simulations using the Monte-Carlo ray-trace technique, which is particularly well suited to this problem because of its adaptability to modelling any geometry. While the Monte-Carlo method has proven useful for the study of isolated clouds, it is still perceived by the atmospheric science community as impractical for complex cloud fields. Previous to the current research, most Monte-Carlo simulations have been restricted to regular arrays of clouds so that symmetry considerations allow the ray to be traced from one cloud cell to the next. The current state-of-the-art in finite cloud modelling appears to consist of no more than regular arrays of uniform, simply shaped clouds (cubic, hemispheric, cylindrical, etc.) simply arranged in infinite checkerboard patterns.

For shortwave radiation, cloud brokenness essentially raises the problem of radiation scattering by heterogeneous media. Although scattering and absorption of solar radiation are linked, the comparative impact of absorption is significantly smaller than the scattering effect. The problem of studying the effect of cloud inhomogeneity on reflected flux was first addressed for isolated cubic clouds by McKee and Cox (1974) using the Monte-Carlo method. Davies (1978) later analyzed a similar geometry using the Eddington approximation. For this simple geometry these authors clearly showed the essential results associated with the influence of the exposed sides of finite isolated clouds. The problem of including the cloud-cloud interactions and the effects of mutual shadowing was then approached, with increasing accuracy and completeness, particularly by Aida (1976), Claussen (1982), Welch and Wielicki (1986), and Kite (1987). For a given cloud cover, the differences in predicted solar fluxes reflected by broken and plane-parallel clouds may amount to 40 to 60 W/m², as shown by Welch and Wielicki (1986). This difference is clearly significant when compared to the approximately 10 W/m² accuracy required by the ERBE program. Moreover, as shown by Harshvardhan (1982), the longwave and shortwave effects by no means compensate so that taking into account cloud brokenness in studies of the cloud radiative impact is clearly important. The main results of these studies may

be summed up in three characteristic types of behavior that broken cloudiness exhibits as a result of geometrical effects (Fouquart et al., 1990).

First, the amount of radiative flux reflected from a single isolated cloud will be less than that reflected from a plane-parallel cloud of equal optical thickness. This is because a certain amount of energy escapes the isolated cloud from its sides and therefore does not contribute to the component of reflected flux. Secondly, a broken cloud field will show a higher effective cloud cover, and therefore will have a higher effective albedo, for non-nadir solar zenith angles as more of the cloud sides are exposed to direct sunlight. This effect is not reproduced by plane-parallel models. Thirdly, as the solar zenith angle increases further, the above effect is reduced as neighboring clouds cast shadows upon each other.

2.3 Radiation Field Anisotropy

Prediction of earth-reflected fluxes requires the use of Bidirectional Reflectivity Distribution Functions (BRDFs) to account for the anisotropy of the measured radiation field. The exact definition and use of the BRDF is described in detail in Chapter 3. The Nimbus 3 experiment (Raschke et al., 1973) was the first attempt to correct for the anisotropic character of the radiation emitted and reflected from the earth-atmosphere system. The Nimbus 3 shortwave data were classified as viewing either ocean, land/cloud, or snow. These scene types were a result of limited data available to describe BRDFs and of limited ability to distinguish clear sky from cloudy scenes.

As a result of Nimbus 3 data, the Nimbus 7 earth radiation budget broadband scanner observed the earth in a biaxial scan pattern. This allowed for the collection of data for a more complete range of viewing zenith and azimuth angles. These data were then used to develop more comprehensive BRDFs over a wide range of scene types. Taylor and Stowe (1984) developed these new BRDFs from the Nimbus 7 data to construct bidirectional models for a range of uniform surface types: clear ocean, land, snow, ice and four altitude levels of cloud. The only allowance for cloud variation was either clear sky or overcast. The BRDFs used to

process cloudy scenes were derived from data which originated from overcast cloud conditions. Arking and Vemury (1984) have shown that Nimbus 7 data are biased with regard to viewing zenith angle and this is most likely due to the fact that cloud inhomogeneity was not taken into account.

The ERBE program (Barkstrom, 1982) made several improvements in its use of BRDFs to retrieve fluxes from radiance measurements. Most importantly, it used a set of BRDFs which attempted to account for a variation in fractional cloud cover, instead of simply clear sky and overcast conditions. Four basic scene categories were defined based on cloud cover: clear (0 - 5 percent), partly cloudy (5 - 50 percent), mostly cloudy (50 - 95 percent), and overcast (95 - 100 percent). The ERBE BRDFs represent an average of anisotropy for many cloud observations. The models were intended to give unbiased flux estimates only when applied to a large ensemble of measurements. However, post-flight analysis (Suttles et al., 1992) has shown that the estimated shortwave albedo systematically increases with viewing zenith angle. It is generally accepted that the ERBE BRDFs underestimate both longwave limb-darkening and shortwave limb-brightening (Green et al., 1994).

Chapter 3 Atmospheric Radiation Theory

The purpose of this chapter is to present a description of the basic fundamental theory necessary to describe the transfer of radiation in a participating medium. This theory is then presented in terms of application towards solving problems in atmospheric radiation. This discussion is based on a similar discussion by Seigel and Howell (1992) and is intended for the reader who is already somewhat familiar with radiation heat transfer.

3.1 Gaseous Radiative Heat Transfer

3.1.1 Attenuation of Radiation by Absorption and Scattering

Consider a beam of radiant energy incident to a volume element of thickness dL , shown in Figure 3.1. As the radiation passes through the volume, its intensity along the direction of travel may be reduced through absorption by the medium. This change in intensity is proportional to the local value of the intensity, and can be expressed as

$$di_{a\lambda} = -\sigma_{a\lambda}(x) i_{\lambda}(x) dx. \quad (3-1)$$

The absorption coefficient $\sigma_{a\lambda}$ varies strongly with wavelength and often substantially with temperature and pressure. The absorption coefficient is a physical property of the participating medium and has dimensions of reciprocal length. In fact, the absorption coefficient can be considered the inverse of the mean free path length that a given bundle of energy will travel before being absorbed by the medium. Thus a small value of $\sigma_{a\lambda}$ corresponds to a long mean free path length. The subscript λ signifies a spectral property. Considerable analytical and experimental effort has been expended to determine $\sigma_{a\lambda}$ for various gases, liquids, and solids. Analytical determination of the absorption coefficient requires detailed quantum-mechanical calculations and, except for the simplest gases such as atomic hydrogen, the calculations are very tedious and require many simplifying assumptions.

In addition to the process of absorption, the radiation in a beam can also be attenuated by scattering of energy out of the beam. This can be expressed in the same fashion as attenuation by absorption, but using a scattering coefficient $\sigma_{s\lambda}$ instead of the absorption coefficient,

$$di_{s\lambda} = -\sigma_{s\lambda}(x) i_{\lambda}(x) dx. \quad (3-2)$$

As in the interpretation of the absorption coefficient, the scattering coefficient can also be regarded as the reciprocal of the mean free path length that radiation will traverse before a scattering event. The scattering coefficient accounts only for the scattering of energy out of the beam. The concept of scattering into the beam is a separate issue and is considered shortly.

3.1.2 Emission of Radiation by a Gaseous Medium

The next process to consider is that of emission of energy within the medium. Consider a differential volume element dV , with absorption coefficient $\sigma_{a\lambda}$. To maintain thermodynamic equilibrium in the absence of heat conduction and heat sources, dV must spontaneously emit an amount of energy equal to that which it absorbs. Also, when the spontaneous emission is the same in all directions (isotropic), which is the condition for most cases, it is easily shown that the radiation intensity spontaneously emitted by a volume element into any direction is

$$di_{em\lambda} = \sigma_{a\lambda}(x) i_{b\lambda}(\lambda, T) dx. \quad (3-3)$$

The term $i_{b\lambda}$ represents the blackbody emission of radiation by the gaseous medium at temperature T and wavelength λ .

3.1.3 Augmentation of Radiation by Scattering

The scattering of intensity into a beam is described with the use of the phase function $\Phi(\theta, \phi)$, which can be physically interpreted as the intensity scattered into direction (θ, ϕ) normalized by the intensity that would be scattered in that direction if scattering was isotropic. For isotropic scattering, the phase function Φ is equal to unity for all incoming directions θ and ϕ . For any type of scattering, the augmentation of intensity in direction x by incoming scattering can be expressed as

$$di_{i,\lambda} = \frac{\sigma_{s\lambda}}{4\pi} \int_0^{2\pi} \int_0^{\pi/2} i_{\lambda}(\theta, \phi) \Phi(\theta, \phi) \sin\theta d\theta d\phi dx, \quad (3-4)$$

where the integration is over all incident angles. The intensity term in the kernel represents the intensity from directions outside the beam in direction θ, ϕ .

3.1.4 Equation of Radiative Heat Transfer

Equations 3-1 through 3-4 represent the four interactions radiation may undergo while traversing a volume of a gaseous medium, which may either increase or decrease the magnitude of the radiation. The net change in intensity in direction x can be found by summing these four terms together,

$$\begin{aligned} \frac{di_{\lambda}}{dx} = & -\sigma_{a\lambda}(x) i_{\lambda}(x) + \sigma_{a\lambda}(x) i_{b\lambda}(\lambda, T) - \sigma_{s\lambda}(x) i_{\lambda}(x) \\ & + \frac{\sigma_{s\lambda}}{4\pi} \int_0^{2\pi} \int_0^{\pi/2} i_{\lambda}(\theta, \phi) \Phi(\theta, \phi) \sin\theta d\theta d\phi. \end{aligned} \quad (3-5)$$

The terms of the above equation represent, in order, loss by absorption, gain by thermal emission, loss by scattering out of the beam, and gain by scattering into the beam. The two terms for decrease by absorption and scattering may be combined into a single term described as the *extinction* term. This is done by defining the extinction coefficient as

$$\sigma_{e,\lambda} = \sigma_{a,\lambda} + \sigma_{s,\lambda}. \quad (3-6)$$

The scattering and absorption coefficients individually are often referred to as the scattering and absorption extinction coefficients.

The albedo for single scattering Ω_λ is the ratio of the scattering coefficient to the extinction coefficient,

$$\Omega_\lambda = \frac{\sigma_{s,\lambda}}{\sigma_{a,\lambda} + \sigma_{s,\lambda}}. \quad (3-7)$$

For scattering alone, Ω_λ equals unity, while for absorption alone, Ω_λ equals zero. The scattering albedo represents the fraction that is scattered of all the energy that is both scattered and absorbed.

The optical thickness of the medium, u , when both scattering and absorption are involved is defined as

$$u_\lambda(L) = \int_0^L \sigma_{e,\lambda}(x) dx. \quad (3-8)$$

This expression is the integral of the product of extinction coefficient and length over the entire path length L . The optical thickness is indicative of the opacity, or "fogginess", of a medium

over a given path length. A medium with an optical thickness less than unity is considered optically thin, while a medium with an optical thickness much greater than unity is considered optically thick.

Equation 3-5 can now be expressed in terms of the scattering albedo and optical thickness,

$$\begin{aligned} \frac{di_{\lambda}}{du_{\lambda}} = & -i_{\lambda}(u_{\lambda}) + (1 - \Omega_{\lambda})i_{b\lambda}(\lambda, T) + \\ & \frac{\Omega_{\lambda}}{4\pi} \int_0^{2\pi} \int_0^{\pi/2} i_{\lambda}(\theta, \phi) \Phi(\theta, \phi) \sin\theta d\theta d\phi. \end{aligned} \quad (3-9)$$

A source term $I_{\lambda}(u_{\lambda})$, which combines the term for emission and absorption along with the scattering into the beam, is defined as

$$I_{\lambda}(u_{\lambda}) = (1 - \Omega_{\lambda})i_{b\lambda}(\lambda, T) + \frac{\Omega_{\lambda}}{4\pi} \int_0^{2\pi} \int_0^{\pi/2} i_{\lambda}(\theta, \phi) \Phi(\theta, \phi) \sin\theta d\theta d\phi. \quad (3-10)$$

The equation of transfer, Equation 3-9, then becomes

$$\frac{di_{\lambda}}{du_{\lambda}} + i_{\lambda}(u_{\lambda}) = I_{\lambda}(u_{\lambda}). \quad (3-11)$$

This is an integrodifferential equation since i_{λ} is also inside the integral of the source term.

An integrated form of the equation of transfer is obtained using an integrating factor $e^{u_{\lambda}}$. Multiplying through by this gives

$$e^{u_{\lambda}} \frac{di_{\lambda}}{du_{\lambda}} + i_{\lambda}(u_{\lambda}) e^{u_{\lambda}} = \frac{d}{du_{\lambda}} [i_{\lambda}(u_{\lambda}) e^{u_{\lambda}}] = I_{\lambda}(u_{\lambda}) e^{u_{\lambda}}. \quad (3-12)$$

Integrating over optical depth from $s = 0$ to $s = u_\lambda$ gives

$$i_\lambda(u_\lambda) = i_\lambda(0)e^{-u_\lambda} + \int_0^{u_\lambda} I_\lambda(s)e^{-(u_\lambda-s)}ds. \quad (3-13)$$

Equation 3-13 is physically interpreted as the intensity at optical depth u_λ being composed of two terms. The first is the portion of the initial intensity which has been attenuated by absorption and scattering in the intervening medium. The second is the component of the intensity at u_λ resulting from emission and incoming scattering by all points along the path, reduced by the exponential attenuation between the originating point s and the final point u_λ .

The difficulty in solving the problem defined by Equation 3-13 arises with the fact that in order to evaluate the source term integral, the temperature field must be known *a priori* to allow the calculation of the necessary absorption coefficients and phase functions. The temperature distribution depends on energy conservation within the medium, which in turn depends on the total amount of absorbed radiation in each volume element along the path. This total energy is obtained by using the spectral intensity passing through a location and integrating over all incident direction solid angles and all wavelengths. A variety of simplifying assumptions can be made to solve this problem by analytical means, but the results of such work are generally for very specific conditions.

3.2 Application to Shortwave Atmospheric Radiation Problems

This section describes the simplifying assumptions made in the development of an atmospheric shortwave ray-trace model. It reveals how the radiative equation of heat transfer has been applied, and how it is to be interpreted in the sense of a Monte-Carlo ray-trace. The boundary conditions in the model are also discussed.

3.2.1 Atmospheric Absorption

Thermal emission of energy by atmospheric gases is negligible in the shortwave portion of the spectrum due to the inherently low temperature. The absorption of energy by these gases is very much wavelength dependent, and for the most part is negligible in the shortwave portion of the spectrum (Parol et al., 1994). Along the same lines, it is also assumed that cloud particles do not absorb any significant fraction of shortwave energy. Certain scientists have expressed concern that a certain amount of shortwave absorption does occur either in the atmosphere or clouds. This term is often referred to as anomalous absorption (Cess et al., 1995) and to date it is still unclear as to the exact nature of this phenomenon (Levi, 1995).

3.2.2 Rayleigh Scattering

The scattering of radiation by atmospheric molecules is accurately modelled using Rayleigh scattering theory. Rayleigh scattering (McCartney, 1976) occurs when the scattering particle is much smaller than the wavelength of the incident radiation. The amount of scattering of this type varies directly as the second power of the particle volume and inversely as the fourth power of the radiation wavelength. The Rayleigh scattering phase function is such that equal amounts of energy are scattered into both the forward and rearward hemispheres. The phase function is given as

$$P(\theta) = \frac{3}{4}(1 + \cos^2 \theta), \quad (3-14)$$

where θ is the relative angle of scattering. This phase function is illustrated in Figure 3.2.

The principal Rayleigh scatterers in the atmosphere are the molecules of atmospheric gases. The wavelength dependence of Rayleigh scattering is the reason why the sky appears red at sunrise and sunset and why the sky appears blue during the day. Blue light (shorter wavelength) is scattered by atmospheric molecules much more than red light (longer wavelength). Thus sunsets and sunrises appear red because most of the blue light has been scattered out of the

direct path between the observer and the sun, thereby producing blue skies outside the beam. The scattering extinction coefficient calculated from electromagnetic wave theory is expressed as

$$\sigma_{s,R} = \frac{8 \pi^3 (n^2 - 1)^2}{3 N^2 \lambda^4}. \quad (3-15)$$

The term n is the index of refraction of the atmosphere, which varies directly with the density. The particle number density is given by N and the wavelength by λ . The application of this theory to the current problem is described in the next chapter.

3.2.3 Mie Scattering

Scattering and absorption of electromagnetic waves by spherical water droplets can be solved exactly by Mie theory (Mie, 1908), which is a complete, formal theory of the interaction of a plane wave with a dielectric sphere. The Mie theory (Liu, 1992) is applicable to a single homogeneous sphere; however, most cloud particles, with the exception of high-altitude cirrus clouds, which are made up of ice crystals, are composed of a distribution of water droplets with sizes ranging from one to ten micrometers. In order to apply Mie theory to typical water droplet clouds, the characteristics of the particle size distribution must be known. Because cloud particles are sufficiently far from each other and because the distance between them is much greater than the incident wavelengths in the solar and near infrared regions of the spectrum, the independent (or incoherent) scattering concept may be applied. This means that scattering by one particle in terms of the electric field may be treated independently of that by other particles. It is in this context that Mie theory has been applied to scattering by cloud water droplets.

A detailed discussion of the numerical techniques for the computation of the Mie solution has been written by Deirmendjian (1969). The Mie scattering phase function and extinction coefficients used in this research have been calculated using an algorithm developed by Schuster (1995) based on the work of Hansen (1971). In order to characterize the Mie scattering

properties of the particles in a water cloud, it is necessary to first define a size distribution of the cloud particles. An appropriate distribution is one based on the gamma distribution

$$n(r) = C r^{\left(\frac{1-3v_{eff}}{v_{eff}}\right)} e^{\left(\frac{-r}{r_{eff}v_{eff}}\right)}, \quad (3-16)$$

where r_{eff} is the mean effective particle radius and v_{eff} is the effective variance. The mean effective radius is defined as

$$r_{eff} = \frac{\int_0^{\infty} r \pi r^2 n(r) dr}{\int_0^{\infty} \pi r^2 n(r) dr}, \quad (3-17)$$

and has units of μm . This expression differs from the simple mean radius in that the particle area has been included as a weighting factor. The mean effective radius is a very significant characterization of a particle size distribution, and in many cases is completely adequate. However, the effective variance can also provide useful information. It is defined as

$$v_{eff} = \frac{\int_0^{\infty} (r-r_{eff})^2 \pi r^2 n(r) dr}{r_{eff}^2 \int_0^{\infty} \pi r^2 n(r) dr}. \quad (3-18)$$

The factor r_{eff}^2 is included in the denominator of Equation 3-18 to make v_{eff} dimensionless and a relative measure. Different cloud particle size distributions having the same values of r_{eff} and v_{eff} will have similar scattering properties. Table 2, adapted from Liu (1992), shows typical parameter values for a range of cloud types. Figure 3.3 shows the Mie scattering phase function

calculated for the fair weather cumulus cloud type. The scattering extinction coefficient for this cloud medium is calculated to be 0.0863 m^{-1} .

3.2.4 Aerosols

Scattering by aerosols (McCartney, 1976) has not been included in this model, even though in many cases it can be an important contributor to both atmospheric scattering and absorption. Aerosols are produced by natural processes (volcanic dust, sea spray, smoke, etc.) and by industrial processes (combustion products). This source of radiation scattering and absorption has not been included because of the very complex scattering properties of aerosols. These particles are often constructed of large numbers of molecules, and thus their shape is very much nonspherical. This geometric irregularity makes it very difficult, if not impossible (van de Hulst, 1981), to predict the scattering phase function and extinction coefficient of individual particles. In part because of this, the effect of aerosols has been ignored. Another difficulty with aerosols is that their distributions throughout the atmosphere vary strongly with time and location.

3.2.5 Scattering by Ice Crystals in High-Altitude Cirrus Clouds

Cirrus clouds (Liu, 1986; Flamant, 1989) have not been modeled as part of this research. These clouds regularly cover about 30 percent of the globe and have been identified as a major uncertainty in weather and climate research. Unlike water clouds, high altitude cirrus clouds are often optically thin and are composed of large, nonspherical ice crystals. These ice crystals may be in the shape of bullets, columns, and plates. They scatter incident solar energy in a fashion quite different from water droplets. Scattering events in cirrus clouds are caused by multiple reflections occurring inside ice crystals as well as by refraction as the radiation enters and leaves the crystal. The complexity of the ice crystal geometries and the large variations seen in their size distributions, make it very difficult to predict scattering phase functions representative of typical ice crystal populations. Also, the geometry of cirrus clouds is very different from that of low-altitude cumulus and stratus clouds. For these reasons cirrus ice clouds were not included as part of this research.

3.2.6 Surface Absorption and Reflection

While it has been possible to assume an atmosphere that is nonabsorbing in the shortwave spectrum, this is not possible for the surface of the earth. In fact, the type of underlying earth surface plays a very important role in determining the characteristics of the radiation reflected from or absorbed by the earth. For example, the Nimbus 7 ERB data (Taylor and Stowe, 1984; Smith et al., 1992) show that the ocean albedo varies with increasing solar angle from under 5 percent up to 30 percent. Snow surfaces on the other hand show a very nearly constant albedo of near 70 percent which begins to taper off to lower values only at extreme solar angles.

The focus of the current research is on fair weather cumulus and stratocumulus clouds over the ocean. We are trying to establish the utility of the current approach to cloud modelling and to that end it is not necessary to consider all possible scene types. A large fraction of the earth's surface is ocean, which is inherently a much simpler surface type than land, which can include mountains, forest, croplands, etc. For these reasons, only the reflecting characteristics of ocean surfaces are considered. A comprehensive set of data for ocean surface reflection of visible light has been collected by Cox and Munk (1954a, 1954b, 1955). This work involved making aerial photographic measurements of the reflected sunlight from the ocean surface. The premise behind this work was that, if the sea surface were absolutely calm, a single mirror-like reflection of the sun would be seen at the horizontal specular point. In the usual case there are thousands of dancing highlights. At each highlight there must be a water facet, possibly quite small, which is so oriented as to specularly reflect an incident ray from the sun towards the observer. The further the facet is from the horizontal specular point, the steeper the facet's slope must be in order to reflect the sun's rays to the observer. The distribution of surface facet orientations is directly related to the wind speed above the ocean surface.

Cox and Munk made many hundreds of measurements of the glitter patterns for various wind conditions and solar angles.. From this work it was possible to determine a semi-empirical expression for the surface slope distribution as a function of wind speed. This in turn allows for the calculation of both the ocean albedo and bidirectional reflecting characteristics as a function

of the angle of incidence and wind speed. Specific values for the albedo and BRDF are given in the next chapter.

3.2.7 Equation of Radiative Transfer Applied to Shortwave Atmospheric Radiation

A typical problem consists of a partly cloudy scene over an ocean surface. The clouds show a high degree of horizontal inhomogeneity and three-dimensionality. The information sought from the solution of this problem is the shortwave radiation field at the top of the atmosphere. This consists of the angular distribution of radiation intensity, or radiance, ($\text{W}/\text{m}^2/\text{sr}$) exiting the atmosphere as a function of position at the top of the atmosphere at a given wavelength in the interval $0.1 - 5.0 \mu\text{m}$.

A number of simplifications can be made to the radiative equation of transfer, Equation 3-13, when it is applied to atmospheric shortwave radiation problems. For example, emission and absorption by the atmosphere and clouds are considered to be negligible; thus the first term of the source term, Equation 3-10, reduces to zero since Ω_λ reduces to unity, and all that is left of the source term is

$$I_\lambda(u_\lambda) = \frac{1}{4\pi} \int_0^{2\pi} \int_0^{\pi/2} i_\lambda(\theta, \phi) \Phi(\theta, \phi) \sin\theta d\theta d\phi. \quad (3-19)$$

The source term now represents only the radiation that has been scattered into the beam from all other directions. For this problem, the scattering phase function $\Phi(\theta, \phi)$ will be defined by either Rayleigh or Mie scattering theory. The distinction between the two types of scattering at any instant is whether or not the radiation in question is traveling inside a cloud. If it is not inside a cloud, then the only source of scattering will be the atmosphere itself (Rayleigh scattering). Mie scattering will dominate if the beam is inside a cloud where such scattering is several orders of magnitude stronger than Rayleigh scattering.

The only significant boundary condition for this problem is the surface of the earth at the bottom of the atmosphere. This is completely defined by the ocean albedo and reflecting characteristics discussed in the previous section. When a beam of radiant energy strikes the ocean surface, a fraction of it is absorbed. This fraction is governed by the albedo, which is dependent on the angle of incidence. The fraction of energy which is not absorbed by the ocean is redirected upwards in a fashion defined by the ocean's bidirectional reflectivity properties.

The volume of the atmosphere defined in the problem is finite in all three dimensions. Cyclic boundary conditions have been implemented to describe the horizontal boundaries of the problem. When a beam of energy arrives at one of the side "walls" of the atmosphere, it is simply translated to the exact opposite side of the domain, where it re-enters the atmosphere and continues on through the atmosphere. The radiation passing upwards through the top of the atmosphere escapes the domain of the problem, and is no longer considered as part of the problem.

3.3 Review of Various Solution Methods

Equation 3-13 is an integrodifferential equation whose exact analytical solution for complex geometries can be difficult, if not impossible, to obtain. The Monte-Carlo ray-trace method has been used in this research to solve Equation 3-13, since it has proven to be the most flexible in allowing for very complex geometries (inhomogeneous and three-dimensional clouds). However, other numerical solution techniques are available which may be even more appropriate, given a different (simpler) problem. Siegel and Howell (1992) discuss a variety of these solution techniques.

3.3.1 The P-N (Differential) Method

The P-N approximation reduces the integral equation of radiative transfer in media to a differential equation by approximating the transfer relations with a finite set of moment equations. Unfortunately, the procedure provides one less equation than the number of unknowns

generated. To overcome this difficulty, the intensity is approximated by a series expansion in terms of spherical harmonics, denoted by P , and the series is truncated after a selected number of terms, N . When the series is truncated after one or three terms, the method is called P-1 or P-3; in general it is the P-N method. It is also referred to as the moment method and the differential approximation. The first three moment equations each have a physical significance, so this technique has some physical basis. For engineering problems, the P-3 approximation has been found to be adequate. Further information about this technique may be found in the works of Bayazitoglu (1979) and Modest (1990).

3.3.2 The Discrete Ordinate Method

The discrete ordinate method is an extension of the two-flux method used for the study of radiative transfer in stellar atmospheres. The two-flux method is based on a simple model with the intensities in the positive and negative coordinate directions each assumed isotropic over their respective hemispheres of solid angles. Anisotropic scattering may be considered but is used as an integrated average fraction for forward and backward scattering. The method works well in one-dimensional problems. When the solid angle about a location is subdivided into more than two hemispheres, each with uniform intensities as used in the two-flux method, the procedure is known as the multiframe, discrete ordinate, or S_n method. In this method, the general transfer relations are represented by a discrete set of equations for the average intensity over a finite number of ordinate directions. Integrals over solid angles are replaced by sums over the ordinate directions. Also the scattering phase functions are generally expanded into Legendre polynomials. Since intensities along each positive and negative ordinate direction around a node must be found, an even number of simultaneous equations must be solved at each node, where the solution is the intensity passing through the node in each of the finite directions.

3.3.3 The Finite Element Method

The finite element method (FEM) holds promise for solving radiative transfer problems because it can provide a match with the computational grid used when other energy transfer modes are present. It can also provide an exact solution, in the sense that the exact transfer equations can be solved. Results have been obtained with the FEM by solving the integral form of the equation of transfer for a grey medium, and some results were obtained for two-dimensional geometries. Finite-element calculations for pure radiation problems are time consuming because they require the solution of the integral equation of transfer to determine the value of the radiative intensity at each node in the domain. The finite element method essentially communicates information from one node to its neighbors. This poses a problem for optically thin problems where radiation must be able to travel relatively long distances before being extinguished. Numerical accuracy can in principle be improved by increasing the number of elements; however, this is at the expense of increased computer time. The FEM is very adaptable to problems which involve other modes of heat transfer (i.e. conduction or convection).

3.3.4 The Monte-Carlo Ray-Trace Method

The Monte-Carlo method is a technique of statistical simulation to determine the average behavior of a system. Halton (1970) provides a good historical account of the general Monte-Carlo method and a description of its fundamental theory. Its current popularity started with its use by researchers at Los Alamos National Laboratory in the late 1940's and early 1950's in the development of nuclear weapons technology. It is a technique which can be applied to a wide variety of applications such as the modelling of thermodynamic gas properties, radiation shielding, cell population studies, search and optimization procedures, signal detection, etc. The Monte-Carlo ray-trace technique is also very applicable to solving radiative heat transfer problems involving highly inhomogeneous problem domains. It is primarily for this reason that this technique has been chosen to analyze the three-dimensional cloud fields of the current research.

The principal idea of this method consists of following a finite number of energy bundles, or "rays", through their transport histories. The radiative behavior of the system is determined from the average behavior of the bundles. One of the benefits of this technique is that it is possible to account for a large variety of effects in problems involving participating media. This can be done without resorting to any of the simplifying assumptions which are often necessary for numerical solutions based on more traditional analytical formulations. Other numerical methods attempt to find a solution to Equation 3-13 through various numerical solution techniques. Equation 3-13 is itself a model of the true problem, and it may be necessary to simplify it in order to apply a particular numerical method. The Monte-Carlo ray-trace method is unique in that it does not attempt to directly solve Equation 3-13, but instead models the true physics affecting individual energy bundles as they traverse the domain of the problem. Thus in the end, if a sufficiently large number of rays have been traced, the true radiative solution is obtained. This solution method will reproduce reality to the extent that the fundamental physics have been properly accounted for in the ray-trace process.

In order to trace an individual ray through the domain of the problem, a geometrical description of the domain is required. This may be obtained by subdividing the problem into a number of elements, where an element can be either a solid surface or a volume of a gaseous medium. An example of a surface element is a planar surface defined by three or more points in space. A volume element is defined by the space enclosed by four or more surface elements. In general the surface properties (absorptivity, emissivity, and bidirectional reflectivity) are assumed to be uniform over the area of the surface elements. The same can also be said of the volume elements, in that the medium properties (absorption coefficients, scattering coefficient, and scattering phase function) are assumed to be uniform throughout the volume.

One particular implementation of the Monte-Carlo ray-trace method is the calculation of the *distribution factor* (Mahan and Eskin, 1984) from element i to element j , $D_{i,j}$. This represents the fraction of radiation power or flux emitted from element i that is ultimately absorbed by element j . In general, a large number of rays is emitted diffusely from element i and each ray is traced through the domain until it is finally absorbed by another element (surface or volume).

Each ray may undergo any number of scattering or reflection events at other elements before it is absorbed. The total number of rays, N_i , emitted from element i is proportional to all the radiant energy emitted from element i . The subset of the N_i rays absorbed at element j , N_{ij} , is similarly related to the fraction of energy absorbed at j . The distribution factor is estimated as

$$D_{ij} \cong \frac{N_{ij}}{N_i}. \quad (3-20)$$

When a sufficiently large number of rays is traced, D_{ij} represents the fraction of energy emitted by element i that is ultimately absorbed at element j . The distribution factor normally is applied to calculate Q_{ij} , which is the power emitted by surface i eventually absorbed by surface j . This is expressed as

$$Q_{ij} = \epsilon_i A_i \sigma T_i^4 D_{ij}, \quad (3-21)$$

where ϵ_i is the emissivity of surface i , A_i is the area of surface i , T_i is the temperature of surface i , and σ is the Stefan-Boltzmann constant. This technique has been applied in various modelling efforts within the Thermal Radiation Group (Eskin, 1981; Meekins, 1990; Tira, 1991; Chapman, 1992; Bongiovi, 1993; Nguyen, 1994; Villeneuve et al., 1994; Walkup, 1996)

The heart of the Monte-Carlo ray-trace method is the statistical nature in which scattering, reflection and absorption events are modelled. For example, if the absorptivity of surface i is represented by α_i , then a random number R uniformly distributed between zero and unity is drawn for each ray arriving at surface i to see whether or not it is absorbed. If R is less than α_i , then the ray is absorbed; otherwise the ray is reflected. A similar procedure is performed for absorption by a gaseous medium in a volume element. The modeling of reflection and scattering directions is slightly more complicated but is still determined in a similar statistical fashion. The complete implementation of the Monte-Carlo ray-trace technique is described in the next chapter.

Chapter 4 Model Description

The details of the Monte-Carlo ray-trace atmospheric radiation model developed as part of this research are described in this chapter. In general each section relates to a certain aspect of atmospheric radiation physics and how it is modelled in a Monte-Carlo sense.

Figure 4.1 is a schematic representation of the processes which a given ray may undergo as it travels from one atmospheric control volume to the next. While a ray is passing through the atmosphere, it may undergo Rayleigh scattering, or it may enter into a cloud bounding box (defined later) where it is scattered via Mie scattering any number of times by the cloud defined inside the box. A ray will either be absorbed or reflected at the earth's surface, where the surface albedo is defined as a function of the incident zenith angle. If a ray is reflected, the probability of the ray being reflected in any given direction is characterized by a BRDF for that particular surface as a function of the incident angle. When a ray exits the atmosphere through the top of the atmosphere (TOA), the information of its final position and direction are used to update the TOA radiation field.

4.1 Grid Systems

This section describes the various grid systems used to discretize the atmospheric domain both spatially and angularly. None of the grids used inside clouds or those used to characterize atmospheric scattering or surface reflection events are discussed in this section. They are each discussed in later sections.

4.1.1 Atmospheric Grid

The atmospheric grid, shown in Figure 4.2, is used to subdivide the atmosphere both horizontally and vertically into uniform-property control volumes. In general these subdivisions allow for spatial variations of atmospheric properties. However, only vertical variations of atmospheric properties have been studied to date. This discussion does not include clouds,

which, of course, *do* vary in all three dimensions. Horizontal grid divisions have been studied, but only as it applies to a particular acceleration technique to be discussed in the next chapter. It is assumed that the atmosphere itself, excluding clouds, is horizontally homogeneous. The atmospheric grid is defined by the set of nodes defining the corners of each control volume.

The atmosphere vertical divisions are chosen such that each of the horizontal layers contains an equal mass of atmospheric gases. Since atmospheric density decreases with increasing altitude, the result is that the higher-altitude control volumes are physically thicker than the lower control volumes, as illustrated schematically in Figure 4.2. The reason for gridding the atmosphere in this fashion is to allow for a higher grid resolution in the portion of the atmosphere where the atmosphere is most dense, and thus where the majority of scattering events occur.

The actual number of grid divisions required will depend on the amount and type of scattering taking place in the atmosphere. Currently, only Rayleigh scattering is considered in the atmosphere itself, as discussed in Section 3.2. It is important to realize that there is an optimum number of grid divisions. Too few divisions will fail to fully capture the scattering properties of the atmosphere, while too many divisions will slow down the model unnecessarily. Excluding the effect of clouds, the time it takes to trace a ray through the atmosphere is directly proportional to the number of vertical atmosphere control volumes.

4.1.2 Top-of-the-Atmosphere Spatial Grid

A secondary two-dimensional spatial grid is placed on top of the three-dimensional atmospheric grid to collect the rays as they exit the atmosphere. This grid is illustrated in Figure 4.3. This TOA grid defines the spatial resolution of the outgoing radiation field and is independent of the horizontal resolution of the atmospheric grid below. The constraints on the resolution of the atmospheric grid deal with optimizing the total number of clouds per atmospheric control volume. This is completely unrelated to the desired spatial resolution of the

radiation field calculated at the TOA, which is why a second grid system is necessary for the TOA.

4.1.3 Top-of-Atmosphere Angular Grid

The hemispherical angular space above each element of the TOA is discretized into an angular grid system, as shown in Figure 4.4. This grid system considers the TOA element as being viewed from the far field, where the element is seen as a point source from any perspective on the angular grid. This grid is defined by equal-angle zenith divisions and equal-angle azimuth divisions. When a ray exits the atmosphere through a given TOA element, it will pass through one of the angular bins defined above that element. Using a TOA spatial grid and an angular grid for each TOA surface element allows for the capture of the complete TOA radiation field by noting which rays pass through which angular bins of which TOA element. The dark rectangle at the origin in Figure 4.4 represents a TOA surface element such as the one shown darkened in Figure 4.3.

At this point it should be noted that the distribution factor used in this model is not that used in the traditional sense as discussed at the end of Chapter 3. The traditional distribution factor $D_{i,j}$ is defined as the fraction of energy emitted from element i that is ultimately absorbed at element j . The distribution factor used in this model is $D_{s,i,j}$, defined as the fraction of energy emitted by the sun (surface s) that eventually exits the atmosphere through TOA element i and through angular bin j of that element.

4.2 The Earth's Surface

The earth's surface is very important in determining the shortwave radiation reflected from the earth-atmosphere system. The type of surface can greatly affect the amount of radiation reflected and the nature of reflection (specular, diffuse, etc.). Absorption and reflection events in the model are each characterized as realistically as possible. However, to date only an ocean surface has been studied. The absorption and reflection properties described in this section

essentially define the boundary condition for the bottom of the atmosphere. The TOA grid discussed in the previous section defines the model's boundary at the top of the atmosphere. The sides of the atmosphere are handled in a different fashion, as described later in Section 4.3.

4.2.1 Surface Absorption

The physical quantity which characterizes surface absorption is the albedo, defined as the fraction of the radiation incident to a surface which is reflected. The albedo value ranges from zero to unity, where zero implies complete absorption and unity implies complete reflection. When a ray arrives at the earth surface in the model, a check is first made to see if it is absorbed or not. Using the Monte-Carlo method, a uniformly distributed random number between zero and unity is drawn using a random number generator and compared with the albedo. If the random number is less than the value of the albedo, the ray is reflected upwards. If the random number is larger than the albedo, the ray is absorbed by the surface.

In general, the manner in which a surface absorbs radiation depends on the angle of incidence of the incoming radiation. For a water surface, a very large fraction of energy will be reflected at shallower incident angles (for zenith angles approaching ninety degrees). We are all familiar with the glare reflected from an ocean or lake surface when the sun is rising or setting. Cox and Munk (1954a, 1954b, 1955) studied the reflection of sunlight from windy ocean surfaces through extensive aerial photography. As mentioned briefly in Subsection 3.2.5, Cox and Munk were able to predict the albedo and bidirectional reflectivity of the ocean surface as a function of incident angle and surface wind speed. The ocean surface albedo as a function of incident angle and surface wind speed is shown in Figure 4.5. Note that the glare at shallow angles (greater than 80 deg) is reduced with increasing wind speed. This is due to the effect of increased wave height casting shadows on the surface of the ocean.

4.2.2 Surface Reflection

Once a ray has been determined to have been reflected from the earth's surface, a BRDF is needed to characterize its reflection. The work of Cox and Munk is used again to determine the ocean BRDF as a function of solar zenith angle for various wind speeds. Figure 4.6 shows an example of the ocean BRDF with solar incident angles of 30 deg and 60 deg for a wind speed of 5 m/s. In this type of figure, the BRDF is plotted as a function of viewing zenith angle (radial coordinate) and viewing azimuth angle (angular coordinate). The small sun symbol indicates the direction of incidence for the incoming solar radiation. The large values in BRDF at both 30 deg and 60 deg zenith angles represent specular reflection peaks from the ocean surface.

The far-field hemispherical space above the ocean surface is discretized into a finite number of angular bins in the same manner as the TOA element angular space indicated in Figure 4.4. The BRDF is given as a function the viewing zenith and azimuth angles for a given incident zenith angle; thus the value of the BRDF is known for each discrete viewing angular bin. The surface BRDF must be put into a special form in order to be used to predict (in the Monte-Carlo sense) the reflected vector for a ray incident to a surface. The BRDF is normalized as $R'(\theta, \phi) = R(\theta, \phi)/S$, where S is the integral of the BRDF over the hemispherical space above the surface,

$$S = \int_0^{2\pi} \int_0^{\pi/2} R(\theta, \phi) \sin\theta \, d\theta \, d\phi. \quad (4-1)$$

The sine factor is provided to account for the fact that a ray represents a unit of power (W), while the BRDF is calculated from intensity (W/m²/sr). The projected area of the reflecting surface elemental varies with the sine of the viewing zenith angle, θ . Thus in order to use the BRDF to predict the reflected direction of a ray, it must be converted into the appropriate units. The result of the BRDF normalization results in the relation

$$\int_0^{2\pi} \int_0^{\pi/2} R'(\theta, \phi) \sin\theta \, d\theta \, d\phi = 1. \quad (4-2)$$

Since the BRDF is known only for the finite number of angular bins defined by the angular grid system, the above integral for S is rewritten as a summation,

$$S = \sum_{i=1}^{N_\phi} \sum_{j=1}^{N_\theta} R_{i,j} \sin\theta_i \Delta\theta_i \Delta\phi_j. \quad (4-3)$$

A new expression for the normalized BRDF is calculated as $R'_{ij} = R_{ij} \sin\theta_i / S$, where now the $\sin\theta_i$ is included in the definition as well. This results in

$$\sum_{i=1}^{N_\phi} \sum_{j=1}^{N_\theta} R'_{i,j} = 1. \quad (4-4)$$

The indices N_θ and N_ϕ are the respective total number of angular bins in the zenith and azimuth angular directions. The $\sin\theta_i$ term is included in the above definition for R' so that Equation 4-4 is simpler to evaluate in the ray-trace model.

A new ray direction is found using R'_{ij} as a weighting factor in determining a vector in the hemispherical space above the reflecting surface. A random number is selected and a loop is initiated over the zenith and azimuth indices of R'_{ij} and a running sum made of the bin values of R'_{ij} . The maximum possible value of this sum is unity because of the normalization defined above. When this sum reaches or exceeds the value of the previously selected random number, the bin where this occurs is the angular bin through which the ray passes. The direction of the reflected vector is then selected uniformly through this angular bin.

4.3 Cyclic Boundary Conditions

The side walls of the model do not correspond to any physical aspect of the atmosphere in the manner that the top and bottom boundaries do. One option would have been to treat the side walls as cold black surfaces, which would then absorb completely all incident rays without emitting any radiation. However this would have affected the TOA radiation field by providing an energy sink not naturally present in the atmosphere. In reality, the atmosphere essentially extends to infinity in all horizontal directions. For this reason the side walls were modelled with cyclic boundary conditions. As indicated in Figure 4.7, when a ray intercepts a side wall (point 1), it is simply copied to the opposite side of the atmosphere (point 2), where it continues with the same direction vector. This procedure is an attempt to model an infinite atmosphere by defining a cyclic atmosphere with infinite copies of the finite model atmosphere. This is analogous to the convention in fast Fourier transform (FFT) analysis of assuming a given time series to be periodic with an arbitrary but large period compared to the period of the harmonic content of the time series. A result of using this type of boundary condition is that the edges of the domain become "contaminated" by edge effects. A possible solution to this problem is to use only a subset of the results which omits the area near the edge of the problem domain.

4.4 Rayleigh Scattering

Scattering in the atmosphere is primarily through Rayleigh scattering, as discussed previously in Chapter 3. The wavelength-dependent Rayleigh scattering of solar energy is a very important factor in determining the angular distribution of shortwave energy leaving the TOA. For clear-sky conditions, it essentially contributes as much energy to the earth-atmosphere albedo as that reflected from the ocean.

4.4.1 Extinction Coefficient

Atmospheric temperature and pressure values from the US Standard Atmosphere (Anon., 1976) were used to calculate atmospheric density as a function of altitude. The Rayleigh

scattering properties are directly related to the index of refraction of the scattering particles, which in turn is directly proportional to the atmospheric density. Figure 4.8 shows the Rayleigh scattering extinction coefficient calculated as a function of altitude (dotted lines). Also shown in this figure are the corresponding values of the extinction coefficient calculated for the discretized atmospheric grid divisions. Five vertical equal-mass grid divisions were found to be sufficient to allow for a converged solution while avoiding an excessive number of grid divisions.

4.4.2 Phase Function

Recall that the phase function $P(\theta)$ is defined as the ratio of the radiation intensity scattered per unit solid angle in direction θ to the average intensity scattered per unit solid angle in all directions. This concept is very similar to that of the BRDF with the exception that the phase function allows for variations in zenith angle only (no variations with azimuth angle ϕ). The phase function assumes a uniform distribution with azimuth angle. Also, the phase function applies to the entire 4π -space surrounding the scattering center, while the BRDF applies to the 2π -space above a surface.

The zenith and azimuth angles are referenced to a local coordinate system based on the direction of the incident vector at the scattering center, and oriented such that the z-axis is along the original path, as illustrated in Figure 4.9.

As with the BRDF, the phase function must be properly discretized and normalized in order to be used with the Monte-Carlo ray-trace method. Mathematically, $P(\theta)$ is normalized as $P'(\theta) = P(\theta)/S$, where S is the integral of the phase function over the zenith angle of 4π -space,

$$S = \int_0^\pi P(\theta) \sin\theta \, d\theta. \quad (4-5)$$

The result of this normalization is

$$\int_0^{\pi} P'(\theta) \sin \theta d\theta = 1. \quad (4-6)$$

Since the phase function is known only as a uniform average value across each of the finite angular bins, the integral for S in Equation 4-5 is rewritten in summation form as

$$S = \sum_{i=1}^{N_{\theta}} P_i \sin \theta_i \Delta \theta_i. \quad (4-7)$$

The normalized phase function is then calculated as $P'_i = P_i \sin \theta_i / S$. The phase function is defined from a discussion of intensity; however a ray is a measure of power. As discussed in Subsection 4.2.2 with regard to the ocean BRDF, the particle phase function must be converted to a format compatible individual rays. Thus the $\sin \theta_i$ factor is included in Equation 4-7 and subsequent normalization. The sum of the normalized phase function over all zenith bins thus yields

$$\sum_{i=1}^{N_{\theta}} P'_i = 1, \quad (4-8)$$

where N_{θ} is the number of zenith angle bins.

In order to determine a new direction for a scattered ray, a random number uniformly distributed between zero and unity is drawn. A loop is initiated over the zenith indices of P'_i and a running sum computed of the phase function bin values at each index. When this value reaches or exceeds the value of the previously selected random number, the angular bin where this occurred is the bin through which the ray is redirected. The azimuth angle is chosen uniformly between 0 to 2π . An angle is chosen uniformly within this bin to define the vector of the scattered ray.

4.5 Clouds

Clouds have been found by many researchers to be the single most important factor influencing the earth's radiation budget. Therefore, special consideration has been given to the modelling of cloud size, shape and composition. The fact that clouds are often optically thick can pose a problem for modelers when performing a Monte-Carlo ray trace. A significant amount of computer resources is required to trace a ray through the history of the many scattering events taking place within a cloud. For this reason an acceleration technique has been developed to overcome this problem, thereby permitting improved performance in optically thick clouds. Essentially, a relatively large cubic volume of cloud medium is pre-processed with a preliminary ray trace to determine its multiple-scattering phase function. This phase function completely describes the scattering properties of the cloud building block. Clouds are constructed by stacking together multiple copies of this cloud building block, or cloud element, to approximate the shape of the desired cloud. A ray trace through this cloud then requires only a relatively small number of evaluations of this phase function for each element instead of tracing the ray through the much larger number of single-scattering events which would naturally occur.

Another benefit of using these pre-defined cloud elements is that they specify a cloud grid which is independent of the atmospheric grid and the TOA grid. The TOA grid resolution is often defined by the resolution of instruments used to measure the earth reflected solar energy.

Clouds in this model are characterized by three quantities. The *cloud bounding box* (CBB) is a rectangular box whose corner nodes are specified in the atmospheric coordinate system. The CBB locates the cloud within the atmosphere. During the ray-trace process, a ray can only enter a cloud by first intersecting one of the six sides of a CBB. Once a ray enters a CBB, a separate procedure is used to follow the ray through the cloud defined inside. The cloud inside the CBB is defined by the *cloud shape array* and the scattering properties of each element of this array is defined by the *cloud element scattering phase function*.

4.5.1 Cloud Shape Array

The cloud morphology is defined by the contents of the cloud shape array. This is a three-dimensional array representing the space inside the CBB. A given cell of the array will either be filled with cloud material, or not. Thus by turning on or off certain cells of the array, it is possible to define the complete three-dimensional shape of the cloud. An example is given in Figure 4.10, where only those cells filled by a cloud medium are shown. Not shown are the empty cells which are completely transparent and thus do not contribute to the Mie scattering inside the cloud. Normally, Rayleigh scattering should take place inside the "empty" cells of the shape array; however, the Mie scattering taking place in the "filled" portions of the cloud is many orders of magnitude more intense than Rayleigh scattering. This justifies not including Rayleigh scattering inside the CBB, which in turn improves the model performance.

No physical size is directly associated with the cloud shape array or any of its cells; the array simply describes the relative shape of the cloud. The size of the cloud is specified by the cloud element scattering phase function used to populate each of the filled elements. The phase function can only be calculated from a finite-sized cube of cloud medium. Thus the size scale associated with the phase function ultimately defines the size of the cloud composed of elements.

4.5.2 Cloud Element Scattering Phase Function

The cloud element scattering phase function defines the multiple-scattering properties of each of the cloud-medium-filled cubic cells of the shape array inside the CBB. The hemispherical space above each face of an element is subdivided into angular bins in the same manner as in Figure 4.4 for the TOA element hemispherical space. The phase function is defined to give the probability that a ray will exit a particular face through a particular angular bin, given the incoming angular bin on face 1. A two-dimensional representation of this definition is shown in Figure 4.11. In this example, the cloud element scattering phase function gives the probability that a ray incident on face 1 through angular bin i will exit the cube via face j through angular

bin k . A three-dimensional version is used in the model where there are six faces and the hemispherical space is divided in both the azimuth and zenith angular directions.

This phase function is calculated in advance through a pre-processing ray-trace of the control volume. The cubic control volume is specified by the length of one of its sides (typically hundreds of meters) and by the Mie scattering properties of the cloud material populating the cube. Rays are traced into the block through each of the incident angular bins of face 1 while their physical entrance points are chosen uniformly across face 1. The path of each ray is traced as it is scattered by the cloud medium until it finally exits the cube through any of the six faces. A note is then made of the angular bin by which the ray exited the control volume, and this information is then used to update the cloud element multiple-scattering phase function. The point on the outgoing face where the rays exit the cube is not needed since an assumption is made that the rays exit a cube face with a uniform spatial distribution. The need for making this assumption and its subsequent implications are discussed in a later paragraph.

The phase function is stored in a five-dimensional array, $P(i, j, s, l, m)$, and is interpreted as the fraction of the radiation intensity entering the control volume through incident angular bin (i, j) on face 1 which exits the control volume through face s via outgoing angular bin (l, m) . The pairs of indices (i, j) and (l, m) correspond to the zenith and azimuth angular bins defined for each face-local coordinate system. This definition is illustrated in two-dimensional form in Figure 4.11.

The cloud element multiple-scattering phase function is evaluated in a fashion very similar to that already discussed for the surface reflections in Equations 4-1 through 4-4. The difference now is that this procedure must be executed for each of the six outgoing faces. Also, instead of a single incident index (zenith angle) as in the case of the surface BRDF, there are now two indices corresponding to the zenith and azimuth incident angles. Given an incident direction bin (i, j) , the process of finding the outgoing vector is begun by choosing a random number uniformly distributed between zero and unity. A running sum of $P(j, s, l, m)$ is initiated over the outgoing faces and bins as

$$SUM = \sum_{s=1}^6 \sum_{l=1}^{N_\theta} \sum_{m=1}^{N_\phi} P(i, j, s, l, m). \quad (4-9)$$

After each increment the current value of the sum is compared to the random number. If the sum is equal to or greater than the random number, the surface and angular bin at which this occurs is the one through which the ray leaves the control volume.

The cloud element phase function contains a large amount of information and it is possible to represent this in a nonintuitive two-dimensional form, as shown in Figure 4.12. The phase function $P(i, j, s, l, m)$ is shown for two separate incident angles and corresponds to a cubic volume of cloud material 100 m on an edge. The Mie scattering properties are indicated in the box at the lower-right of Figure 4.12. The cartoon in Figure 4.12(c) shows the relative orientations of the two vectors a and b incident on face 1. The results shown in Figures 4.12(a) and 4.12(b) are the corresponding values of the phase function at each viewing zenith and azimuth angle for each cube face. As indicated in Figure 4.12(c), the data in Figure 4.12(a) are for energy normally incident, while Figure 4.12(b) is for energy incident at 45-deg zenith angle and 45-deg azimuth angle.

The viewing angles on each face are referenced to a face-local coordinate system similar to that indicated on the incident face 1. The horizontal dimension for each rectangular sub-region represents the azimuth angle index ranging from 0 at the left to 2π at the right. The vertical dimension is the zenith angle index ranging from 0 at the bottom to $\pi/2$ at the top. As an example, the bright area on face 1 of Figure 4.12(a) represents energy leaving the cube through the face it entered via backscattering. The bright areas on faces 3, 4, 5 and 6 in the same figure represent radiation leaving those faces at a shallow angle with respect to the plane of the face. The barely visible bright area on face 2 is energy that has passed entirely through the cube. Figure 4.12(b) shows a similar case with the exception that the incident energy is now arriving at a 45-deg zenith angle and a 45-deg azimuth angle. Notice that much of the energy leaving the element is now through faces 4 and 5, as expected.

The phase function characterizes the scattering properties of each filled element of the cloud shape array. Once a ray has entered the CBB, it is traced through a series of both empty and filled control volumes. When the ray passes through an empty control volume, it is simply traced along its path to the other side of the control volume. A ray can also pass through a filled control volume, in which case the multiple-scattering phase function is used to predict the face, and the angular bin from that face, through which the ray will leave the control volume. When the phase function is evaluated in this manner, the ray is no longer defined in the traditional sense (typically a starting point and a directional unit vector from that point). Instead, the information needed to evaluate the phase function are the incident zenith and azimuth angular bin indices i and j . The output from the evaluation of the phase function are a face number s and the outgoing zenith and azimuth angular bin indices l and m . The point at which a ray enters the filled control volume is unimportant. Since the phase function was defined for a uniform distribution of rays across the incident face, it is assumed that this is also the case inside the cloud. It is also assumed that the rays leave the control volume faces in a uniform spatial distribution. The implications of these assumptions are discussed later in Subsection 4.7.3.

Thus a translation of ray information from one form to the other must be made when the ray moves from an empty to a filled element, and vice versa. An example of this is shown in Figure 4.13, where a ray has entered the CBB at point P_1 with incident vector V_1 . The first element is empty and so the ray is propagated along its initial path to point P_2 . The next element is also empty so the ray continues along to point P_3 , still with direction vector V_1 . At this point the ray is about to enter a filled element and the ray does so through angular bin (i, j) , where i and j are the zenith and azimuth angle bin index numbers. Only the vector V_1 is used to determine these indices; no reference is made to point P_3 . The multiple scattering phase function is evaluated for the incident bin (i, j) , and an outgoing face s and bin (l, m) are found, as indicated at face A in Figure 4.13. The next element is also filled, and so the previous outgoing bin (l, m) is translated into an input bin (i, j) on the next control volume at face B. The phase function is again evaluated to find the output bin (l, m) and outgoing face. Point P_4 is then determined randomly on the outgoing face since the next control volume is empty. A vector V_2

is uniformly chosen in the outgoing bin (l, m) at P_4 . From this point the ray is continued to point P_5 , where it exits the CBB and continues on through the atmosphere.

4.5.3 Cloud Morphology from Landsat Data

Information from Landsat imagery data was used to create realistic clouds for inclusion in the ray-trace model. Figure 4.14 shows a sample Landsat image with four clouds (a, b, c and d) indicated for selection. The data shown in this figure have been converted into the form of optical thickness (Minnis et al., 1992) from the original Landsat radiances. Individual clouds were retrieved from images such as this and each pixel converted into a vertical optical height. It was assumed that the clouds had a flat bottom surface and that all cloud material was built upwards from this level. Clouds typically form with flat bottoms as a result of convective processes. Thus the optical thickness data from the two-dimensional images give all necessary information to create three-dimensional clouds. Figure 4.15 shows four examples of individual clouds extracted from the Landsat images in the previous figure. Figures 4.15(a) through 4.15(d) correspond to the clouds labelled a through d in Figure 4.14. Each square pixel making up these individual clouds represents a vertical column of cloud elements.

4.6 TOA Radiation Field from Ray-Trace Results

The result of analyzing a particular atmosphere and cloud field with the ray-trace model is the distribution factor $D_{i,j,k,l}$ which is defined as the fraction of the solar energy incident at the TOA which later passes upwards through TOA cell (i, j) via angular bin (k, l). The quantity which is needed for analysis is the intensity $i_{i,j,k,l}$ of the radiation passing through each angular bin of each TOA cell. The first step is to convert the distribution factor into the power passing through each angular bin of each TOA cell, $P_{i,j,k,l}$. This is calculated as

$$P_{i,j,k,l} = D_{i,j,k,l} q_o A_{TOA} \cos \theta_o, \quad (4-10)$$

where q_0 is the solar constant (1367.9 W/m²), A_{TOA} is the area of the entire top of the atmosphere, and θ_0 is the solar radiation zenith incidence angle. Equation 4-10 may be thought of as the defining relation for the distribution factor $D_{i,j,k,l}$. From this power the intensity $i_{i,j,k,l}$ passing through each TOA cell (i, j) and through each cell's angular bin (k, l) is calculated as

$$i_{i,j,k,l} = \frac{P_{i,j,k,l}}{\Delta \omega_{k,l} A_{i,j} \cos \theta_k}, \quad (4-11)$$

where the factor $\Delta \omega_{k,l}$ represents the solid of the angular bin (k, l), $A_{i,j}$ is the area of the single TOA cell (i, j), and θ_k is the mean zenith angle of the zenith angular bin k.

4.7 Model Validation

A variety of analyses have been performed to establish the validity and functionality of the atmospheric ray-trace model. First a series of test cases has been carried out to determine the number of rays required to give a converged solution. This number not only depends on the geometry of the model, but also on the application of the results. For example, much fewer rays are needed if only the TOA mean reflected flux is required instead of the scene-average BRDF. Another series of tests has been carried out to determine the optimal size of the cloud control volumes used in the clouds.

In order to run the ray-trace model we were given access to the Silicone Graphics Power Challenge super computer operated by the Atmospheric Sciences Division of NASA Langley Research Center. All of the test cases reported in the dissertation were executed on this computer. Further details about the capabilities of this computer are discussed in Section 4.8.

4.7.1 TOA Flux Convergence

The cloudy scene used to study TOA flux and BRDF convergence is shown in Figure 4.16. This scene is 14 by 14 km with a population of 50 rectangular clouds, where each cloud

measures 1 by 1 km horizontally and is 2 km tall, resulting in 25 percent cloud cover. The clouds are located and oriented randomly in the atmosphere. This cloud field is used to study all convergence related issues. The clouds are simple yet the cloud field as a whole is not a simple regular cloud array. The underlying earth's surface is ocean with a wind speed of 5 m/s. Rayleigh scattering by the atmosphere is included. The clouds here are built up from control volumes with a dimension 250 m on a side, which corresponds to an optical depth of 21.5 for a typical marine cumulus cloud type medium. The TOA grid used for the flux convergence study is not subdivided; rather, it is a single element. Thus the flux through this element is the mean flux reflected from the whole scene. The albedo is determined by normalizing the calculated reflected flux with the incident solar flux.

Figure 4.17 shows the model-predicted albedo as a function of the number of rays traced. Data are shown which correspond to ten different sets of values of the random number generator seeds. The solid line represents the mean albedo and the vertical bars represent one standard deviation of the ten data sets. For this scene, it is clear that about 700 thousand rays are adequate to achieve a converged solution to the reflected flux, or albedo. At this point one standard deviation corresponds to 0.2 percent of the final albedo value. Beyond this point the improvement in calculated albedo is small compared to the additional number of rays traced.

If the TOA grid were to be subdivided into a finer mesh, perhaps to study the spatial variation of reflected flux, then the number of rays traced would have to be increased proportionally. The 700 thousand rays required here represents the number of rays required *per TOA element* to achieve a converged solution. This number will vary with the scene content since various cloud fields and surface types can have very different scattering and reflecting characteristics.

4.7.2 BRDF Convergence

The BRDF may require a different number of rays for convergence than the TOA flux since it deals with a completely different grid system. The TOA flux is based on the spatial grid

at the top of the atmosphere, while the BRDF depends on the angular grid system defined above each of these TOA elements. In general the number of TOA elements is different from the number of BRDF angular bins. Thus different numbers of rays may have to be traced depending on the desired result. If it is desired to produce an "image" of the scene then the number of rays to be traced is the product of those required for both TOA and BRDF convergence since the image requires both angular and spatial convergence.

A measure of the convergence of the BRDF may be obtained by studying the BRDF's symmetry across the plane defined by the solar vector and the surface normal. Asymmetry will be introduced into the BRDF as a result of variance cause by non-convergence in the Monte-Carlo sense. Asymmetry in the BRDF will also occur as a result of asymmetries in the cloud field. Thus a converged solution should only exhibit asymmetry due to the scene content and not to the ray-trace procedure. The rate of convergence can be analyzed in the same sense as the TOA reflected flux by studying a representative value of the BRDF asymmetry as a function of the number of rays traced. This asymmetry parameter may be found by calculating the RMS difference between corresponding angular bins on each half of the BRDF plane of symmetry. This RMS difference field is then integrated over one-half of the hemispherical space above the atmosphere to yield a single scalar number. This is expressed as

$$RMS \text{ Difference} = \sqrt{\frac{1}{\pi} \int_0^{\pi} \int_0^{\pi/2} [R(\theta, \phi) - R(\theta, 2\pi - \phi)]^2 \sin \theta \, d\theta \, d\phi}. \quad (4-12)$$

Notice that the integral over the azimuth angle ϕ is only for half of the hemisphere from 0 to π (instead of 2π).

The integrated RMS difference would be zero if the BRDF were perfectly symmetric. Figure 4.18 shows the mean RMS difference and standard deviation among the ten data sets as a function of the number of rays traced. Data are shown for ten different initial sets of random number seeds. This example is for the same cloud field geometry as in the previous section for

the TOA flux convergence. The BRDF RMS symmetry difference converges at a similar rate as the albedo in the previous section. After approximately 500 thousand rays are traced the RMS difference has reached the point where tracing additional rays has little effect. Notice also that the RMS symmetry does not display the same type of variation in the standard deviation as the TOA albedo did. The RMS symmetry instead converges progressively to a final value. For this case the hemispherical space above the single TOA element is divided into a total of 432 angular bins (12 zenith divisions and 36 azimuth divisions). Thus if the number of 500 thousand rays for convergence is accepted, then slightly over 1000 rays should be traced per angular bin to achieve a converged scene BRDF.

4.7.3 Cloud Control Volume Optimum Size

A series of tests was carried out to determine the limits on the size of the elements used to make up the clouds. In reality, the energy leaving a given cloud element face will *not* be uniformly distributed across that face. However, this uniformity is an inherent assumption in the current model as discussed in Chapter 3. When a ray is traced through a cloud it will pass through a number of cloud elements before finally leaving the cloud. While passing from one element to the next, the only information about the ray that is transferred is direction, not position. This is necessary because of the assumed uniform energy distribution across the element incident face for the calculation of the element phase function. This procedure was used so that spatial resolution in the clouds could be controlled by the number and size of the elements themselves.

As a cloud element becomes larger and larger, it also becomes optically thicker. The implications of this fact are that the distribution of energy leaving a given element face will become less and less uniform as the optical depth increases. As this non-uniformity becomes more significant, the assumption of uniformity becomes less valid. For this reason, it is important to determine the effects of this assumption on the results derived from the ray-trace model. It is quite possible that a maximum cloud element optical depth exists beyond which the

results are invalidated by the violation of the assumption of uniform energy distribution on outgoing element faces.

There also exists a minimum cloud element optical depth below which it is meaningless to venture. A thin element would have few, if any, interior scattering events naturally taking place. However, the phase function for that element must still be evaluated in order to trace the ray through on to the next element. Thus work is done (phase function evaluation) to trace the ray, when in fact the ray should continue uninhibited without a scattering event taking place. In a true Monte-Carlo ray-trace, work is done only at those points where an extinction event (absorption or scattering) takes place. Thus a too-thin cloud element would place an unnecessary computational burden on the computer.

So now the problem is to find the optimum element optical thickness between the minimum and maximum size limits. It is desirable to have the largest element possible, since clouds made up of larger elements need fewer elements and thus require less computer time to trace a ray through. Therefore, the optimum element size *is* the maximum size limit beyond which results are adversely affected by the inherent assumption of uniform energy distribution on the outgoing element faces.

The effect of varying cloud resolution was studied with the same cloud field as in the previous two sections, as shown in Figure 4.16. Since the clouds in this field are 1 by 1 by 2 km, the largest cloud element used was 1 km³, which required only two elements to make up a cloud. The smallest cloud element was 50 m³, and required a total of 16000 elements to make up a single cloud. The reflected flux from this scene was calculated for each cloud element size. Figure 4.19 shows this scene-reflected flux as a function of the number of cloud elements per kilometer of cloud. Notice that as the number of elements increases, the albedo converges toward a final value. It is also important to note that the variation in albedo here across the entire range is only a very small fraction of the total final albedo, so that although the results do converge as a function of increasing cloud resolution, it appears that the model (at least for this cloud field) is fairly insensitive to cloud element size. In this case, the primary factor governing

the cloud element size is the size scale the modeler desires to incorporate into a given cloud field to achieve acceptable spatial resolution. Another important issue related to the cloud resolution is the computer time required to trace a given number of rays. Obviously, more computer time is required to obtain results as more elements are used to make up a given cloud.

The discussion thus far has concerned the results from clouds made of cubic elements. As a means of validation, the scene in Figure 4.16 has also been analyzed using a true ray trace through the clouds instead of using the cloud element scattering phase function to predict the progress of rays through the cloud. The true ray trace simply continues tracing the ray in the traditional sense into the cloud, using the same medium properties as used to calculate the cloud element scattering phase function. The albedo calculated using this technique was found to be 0.442, which is near the center of the range of values obtained using the cloud element phase function. When computer run times are compared between the true ray trace and the model using the elements, it is found that the cloud element technique runs approximately an order of magnitude faster while still giving essentially the same results. Of course, exact times will vary depending on the scene (number of clouds, cloud optical thickness, etc.).

4.8 Spectral Limitations

Currently the model is capable of analyzing a cloudy scene at a single wavelength. On the other hand, the BRDFs used in ERBE and those yet to be defined for CERES apply to the shortwave band ranging from approximately 0.1 to 5.0 μm . In order for model-predicted results to be indicative of this shortwave band, all model properties were evaluated at a wavelength of 0.55 μm since this corresponds to both the most intense solar radiation and the center of the visible spectrum. The Rayleigh scattering extinction coefficient was obtained from the index of refraction of water at a wavelength of 0.55 μm . The cloud element scattering properties were obtained from Mie theory at a wavelength of 0.55 μm . The only properties which were not calculated at this wavelength were the ocean albedo and BRDF data from Cox and Munk (1954a). These data were obtained from visible aerial reconnaissance photometric data.

4.9 Random Number Generator

The accuracy of a Monte-Carlo simulation relies on the quality of the random number generator used. According to James (1990) a random number generator must exhibit six qualities for Monte-Carlo applications. First, the generated numbers must have a uniform distribution and have low correlation between each other. Second, the random numbers must have a sufficiently long period. Every random number generator has a period, which is defined as the count of numbers after which the sequence of numbers begins to repeat itself. Third, the random number generator should produce repeatable sequences of numbers, given the same set of initial values, or seeds. Fourth, a random number generator should have long, disjointed subsequences. This means that using different seeds should result in completely different sequences of random numbers. Fifth, the random number generator should be portable by giving the same results on different computer platforms. Finally, the random number generator should be efficient without compromising any of the above five qualities.

The random number generator used in this research is the RANMAR algorithm recommended by James (1990). This generator is the first of a new generation of portable VLP (very long period) methods. It has a period of 2^{144} , or 2×10^{43} , and is completely portable across all machines having at least 32-bit floating point representation.

4.10 Computer Requirements

We were generously given access to the Silicone Graphics Power Challenge super computer at NASA Langley Research Center for the purpose of running the atmospheric ray-trace model. This computer is equipped with 2 gigabytes of RAM and eight CPUs, with four of them operating at a clock speed of 75 MHz and another four operating at 90 MHz. When the model was run on this computer it did so on a single processor. While no effort was made to construct this model to take advantage of high-level parallelism, it was possible to run multiple copies of the model at the same time on multiple CPUs. Some test cases were also run on the Thermal Radiation Group's Silicon Graphics Indigo², which has a single processor running at 150 MHz.

In terms of model performance, the Indigo² is essentially equivalent to a single of the Power Challenge's processors.

The atmospheric ray-trace model typically runs at a rate of 1 to 25 million rays per hour, depending on the specific cloud-field geometry and atmospheric grid. Obviously, more computer time is necessary for the cases involving clouds composed of large numbers of elements.

Various data files are required as input to define the atmospheric and cloud field geometry, as well as the scattering, reflecting and absorbing properties of the various components. These include data files for the atmosphere and TOA geometry, the Rayleigh scattering extinction coefficient and phase function, the surface albedo and BRDF, the cloud placement, the cloud shape arrays, and the cloud element scattering phase functions. Of these data files, only the cloud element scattering phase function requires a huge amount of storage space; typically 80 megabytes. The size of the radiation field data file produced by the model depends directly on the TOA grid size. For a 50-by-50 TOA grid, the resulting radiation field occupies approximately 10 megabytes of disk space.

Chapter 5 Acceleration Techniques

The purpose of this chapter is to describe some of the techniques that have been used to accelerate or simplify the ray-trace model used in this research. The baseline scene is the same as that used in the previous chapter, shown in Figure 4.16. Without any of the acceleration techniques implemented, this case requires that approximately 600 thousand rays be traced for convergence of the albedo. The clouds in this scene are composed of 250-m cloud elements (requiring a total of 128 elements per cloud). The baseline model traced rays through this scene at a rate of 0.11338 million rays per hour.

5.1 Line-Surface Intersections

This first section does not deal with an acceleration technique. Instead an attempt is made to describe a general method for determining whether or not a ray (line) intersects a finite-sized surface element placed and oriented arbitrarily in three-dimensional space. The specific type of surface is irrelevant; it could be a planar element, a portion of a cylinder or a cone, or any other type of surface. The only important issue is that the surface be defined in an orthogonal coordinate system (rectangular, spherical, etc.). For the purposes of this description, the finite surface will be considered as a triangular planar element in rectangular space.

5.1.1 Intersection Point of a Line with an Infinite Surface

In parametric form, the equations of a line in three-dimensional space are written as

$$\frac{x - A_x}{V_x} = \frac{y - A_y}{V_y} = \frac{z - A_z}{V_z} = T, \quad (5-1)$$

where T is the parameter describing the position (x, y, z) along the line. The line is defined by both a point A with coordinates (A_x, A_y, A_z) and a vector V with direction cosines V_x, V_y , and

V_z . A planar surface is defined by a point P through which the plane passes and a vector N normal to the surface. This is expressed as

$$N_x(x - P_x) + N_y(y - P_y) + N_z(z - P_z) = 0. \quad (5-2)$$

A spherical surface with a center at P and a radius R is defined by the equation

$$(x - P_x)^2 + (y - P_y)^2 + (z - P_z)^2 = R^2. \quad (5-3)$$

A conical surface with a vertex at point P and with cone angle θ is described by

$$(x - P_x)^2 + (y - P_y)^2 - \tan^2\theta(z - P_z)^2 = 0. \quad (5-4)$$

Given a vector defined by Equation 5-1 and any of the surfaces defined above, the intersection point between the two can easily be found. In general x, y, and z are written each from Equation 5-1 in terms of the parameter T and the starting point A of the ray. These expression for x, y, and z are then placed into the corresponding terms in the equation for the surface in question. The result is a second order polynomial as a function of T. If no real solution for T exists, then the ray and the surface do not intersect. If a real value for T can be found, then T is substituted back into Equation 5-1, and values for the intersection point Q (x, y, z) are found. If two real solutions for T are obtained from the solution of the expression for T, then two corresponding valid solutions exist for the point Q.

Thus far the surfaces have been treated as infinite in extent and therefore the intersection point Q may be anywhere on that infinite surface. It is now important to describe a finite surface as a portion of the infinite surface and then determine whether or not the point Q is inside or outside the range of the finite surface.

5.1.2 Does an Intersection Point Exist Within a Finite Surface?

An example of looking for an intersection point on an infinite surface inside a finite portion of that surface is most easily understood with a parallelepiped surface on an infinite plane. Figure 5.1 shows this case with the corners of the parallelepiped defined by points A, B, C, and D. The intersection point on the infinite surface is located at Q, which happens to be inside the finite surface ABCD in this example.

The first step is to define a local coordinate system for the finite surface in terms of two basis vectors. In Figure 5.1, these are indicated by the non-unit vectors $\vec{f} = \vec{AB}$ and $\vec{g} = \vec{AC}$. Since the finite surface in this case is a parallelepiped and not a rectangle, the basis vectors do not necessarily form an orthogonal coordinate system. This does not pose a problem as long as the parallelepiped is not too narrow, i.e., if the angle between the two basis vectors is not too small. In this case a corner, such as B, can always be found where the angle is sufficiently large. Point Q is defined in this system by the vector $\vec{q} = \vec{AQ}$. When \vec{q} is expressed in terms of the basis vectors, assuming the origin of the local and global coordinate systems are each at point A, the result is

$$\begin{aligned} q_x &= s f_x + t g_x \\ q_y &= s f_y + t g_y \\ q_z &= s f_z + t g_z. \end{aligned} \tag{5-5}$$

Three equations are given above since this problem is posed in three-dimensional space. The two unknowns in these equations are s and t. Since there are three equations it is possible to obtain three different solutions to s and t, which should all be equivalent. Once values of s and t are found, a simple comparison can be done to determine whether or not Q exists within the parallelepiped. If both values of s and t are between 0 and 1, then Q is inside the parallelepiped ABDC. If both s and t are greater than 0 and s + t is less than 1, then Q is inside the triangle

ABC. If $s + t$ is greater than 1 and s and t are each less than 1, then Q is inside the triangle DCB.

This technique has been used as the basis of the ray-trace model. While the initial programming effort for this technique was not simple, it allows for a very modular approach to creating an atmospheric grid system and complex clouds. Essentially every physical component of the model was created from finite surfaces such as these. The modular approach to creating this model made it possible to easily add features afterwards that had not even been considered initially.

5.2 Earth Surface Reflection Evaluation

Section 4.2 explained the general technique for determining the angular bin through which a ray passes when it is reflected from a surface characterized by a given BRDF. Recall that the BRDF discussed in this situation applies *only* to the surface of the earth, and not the entire earth-atmosphere system. A normalized form of the surface BRDF, R'_{ij} , is used such that the sum over all angular bins is equal to unity (Equation 4-4). This BRDF is used as a weighting factor on the direction of the reflected rays. As mentioned in Chapter 4, the process of finding the direction of the reflected ray is begun by drawing a uniformly distributed random number between 0 and 1. A running sum is then started over the bins of R'_{ij} until this sum reaches the same value of the random number. In mathematical form, the sum S is calculated as

$$S = \sum_{i=1}^{N_\theta} \sum_{j=1}^{N_\phi} R'(i,j). \quad (5-6)$$

The difficulty with this approach is that the sum must run over an entire ring of N_ϕ azimuth bins for each value of the zenith bin index i (refer to Figure 4.4 to see that a single angular bin is part of a horizontal ring of N_ϕ bins all at the same zenith angle). Thus if the final reflection bin is at a large value of the zenith angle, then almost the entire BRDF must be searched to reach this point. An acceleration technique has been developed to overcome this problem. As a

preprocessing step, a list is made of the sum of each BRDF zenith ring over all azimuth bins of that ring, i.e.

$$R_i^* = \sum_{j=1}^{N_\phi} R_{i,j}'. \quad (5-7)$$

Thus R_i^* represents the sum of $R_{i,j}'$ over a ring of azimuth angle bins for zenith index i . This preprocessing information can now be used to speed the search for the reflection direction bin index numbers. The random number is chosen as before between 0 and 1. The search is now started with R_i^* by summing over the zenith index i until the random number is surpassed. At this point it is known that the reflecting bin is in the current constant zenith ring at zenith index i . The running sum is decremented by one zenith index (by the value of the current ring) to place the sum at the beginning of zenith ring i . The running sum now continues in the azimuth direction from the beginning of the i^{th} zenith ring until the random number is reached again. At this point the zenith index and the azimuth index of the reflecting bin are known. The vector for the ray is then found by calculating a random direction through this bin. As shown in Table 3, a 3.49 percent increase in speed is realized compared to the unaccelerated model when this method is implemented with the model cloudy scene.

5.3 Fractional Absorption

Two traditional methods exist for handling the absorption of energy with the Monte-Carlo ray-trace method. The first is to treat a ray as a discrete amount of energy which is either completely absorbed or completely reflected at a given absorption opportunity. The physical quantity which determines whether or not absorption takes place is the absorptivity, which ranges from zero to unity and can be defined for both a physical surface and a finite gaseous volume. Based on the statistical nature of the Monte-Carlo method, a random number is chosen between zero and unity and then compared with the absorptivity for the current potential absorption event. If the random number is less than the value of the absorptivity, the ray is absorbed. The energy associated with this ray is transferred to the element which absorbed the ray. If the ray is not

absorbed, it is reflected (from a surface) or scattered (in a gaseous medium), and the ray is followed on to the next event in its history. This technique lends itself very well to the Monte-Carlo method in that the physics of the problem is revealed after a statistically significant number of rays has been traced. Several problems are associated with this method, however. These include cases where the absorptivities are extremely low (very reflective surfaces) and where certain surfaces in the geometry are very absorptive. In this latter case a statistically significant number of rays is prevented from reaching a surface where meaningful results are required. This second issue is the one considered here.

The ocean is a very absorptive surface as it typically absorbs upwards of 90 percent of the radiation striking its surface. Using the traditional method, most of the rays traced through the atmospheric model would be absorbed at the surface of the ocean. These absorbed rays only contribute information about the albedo of the earth-atmosphere-clouds system. They contribute nothing to the knowledge of the angular characteristics of the radiation leaving the atmosphere through the TOA. Therefore more rays must be traced in order to achieve a statistically meaningful number of rays which contribute to the radiation field. One way in which this problem can be addressed is to absorb only a portion of the ray at an absorption event, instead of the entire ray. This fraction is equal to the absorptivity of the element encountered. This fraction of energy is then subtracted from the current "value" of the ray at each absorption event (without needing a random number) and the ray continues to the next event. Thus a ray may lose 90 percent of its content when it strikes the ocean surface, but 10 percent may continue on to eventually contribute to the radiation field at the TOA. Thus for a desired level of convergence in the solution, fewer rays need be traced. A similar approach to this problem was performed by Turk (1994).

These two methods have been compared with each other using the baseline cloud field. As mentioned before, without any acceleration methods the test cloud field requires approximately 700 thousand rays for a converged albedo and approximately 500 thousand rays for a converged BRDF. Figure 5.2 shows the calculated albedo and standard deviation using both discrete and fractional absorption as a function of the number of rays traced. The vertical bars

in this figure represent one standard deviation among the ten data points at each value of the number of rays traced. The dashed lines show data for discrete absorption and the solid lines correspond to the use of fractional absorption. It is apparent here that the TOA flux converges after approximately 400 thousand rays for fractional absorption, which is a 43 percent improvement over the 700 thousand rays required for discrete absorption. The BRDF symmetry did not show an expected corresponding increase in rate of convergence. It is felt that this is because rays which reflect from the ocean surface contribute very little information to the BRDF outside of the vicinity of the specular reflection spike. The rays reflected from the clouds most often do not ever reach the ocean surface and so are not affected by this acceleration technique. However it is these cloud-reflected rays which define the BRDF angular properties away from the specular peak. The albedo did show an improvement in convergence since most of the rays reflected from the ocean will escape the atmosphere through the TOA and contribute to the energy reflected from the ocean-atmosphere system.

5.4 Cloud Element Phase Function Evaluation

The cloud element scattering phase function is defined in Section 4.5.2. Recall that $P(i, j, s, l, m)$ gives the fraction of energy entering the cloud element through incident angular bin (i, j) on face 1 which subsequently leaves the element through face s via outgoing angular bin (l, m) . As mentioned in Section 4.5.2, an outgoing vector is found by first selecting a random number uniformly distributed between zero and unity. A running sum is then initiated over the cloud element phase function for the incident bin (i, j) ,

$$S_{i,j} = \sum_{s=1}^6 \sum_{l=1}^{N_\theta} \sum_{m=1}^{N_\phi} P(i,j,s,l,m). \quad (5-8)$$

Recall that the sum of P over all values of s , l , and m for a given i and j yields 1. When the value of $S_{i,j}$ during the running sum reaches or surpasses the value of the random number drawn then the current values of s , l , and m represent the face and angular bin through which the ray leaves the cloud element. As with the surface BRDF evaluation in Section 5.2, the problem with

this approach is that the search must be made over a large number of angular bins before the final outgoing bin is found.

In the same fashion as with the BRDF evaluation, the search through the phase function can be accelerated by pre-processing the phase function to form sums of P over certain ranges of its parameters. The first is to find the sum of P over each of the six outgoing faces,

$$P''_{i,j,s} = \sum_{l=1}^{N_\theta} \sum_{m=1}^{N_\phi} P(i,j,s,l,m). \quad (5-9)$$

This allows the search to be very quickly narrowed down to the particular outgoing face instead of having to search through every bin of each face. Once the outgoing face is found, it is then necessary to find the particular outgoing directional bin on that face. This problem is identical to the BRDF evaluation situation of finding the reflection bin from the ocean surface. Thus in the same fashion a second pre-processing list can be created for the sums of P over each of the constant zenith angle rings for each of the faces,

$$P'_{i,j,s,l} = \sum_{m=1}^{N_\phi} P(i,j,s,l,m). \quad (5-10)$$

The original cloud element phase function P is used in conjunction with the pre-processed information in P' and P'' to find the outgoing angular bin from the cloud element.

The search is begun by selecting a random number between zero and unity and the starting running sum using P'' to find the outgoing face s,

$$S''_{i,j} = \sum_{s=1}^6 P''(i,j,s). \quad (5-11)$$

Once the value of S''_{ij} reaches or surpasses the value of the random number, then the outgoing face s has been found. The value of S''_{ij} is decremented by one face index so that it now represents the sum up to the beginning of the current face. The next step is to find the constant zenith angle ring through which the ray passes. This is done by continuing the running sum, but now using P' to give the outgoing zenith index l ,

$$S'_{ij} = S''_{ij} + \sum_{l=1}^{N_\theta} P'(i,j,s,l). \quad (5-12)$$

Once the value of S'_{ij} reaches or surpasses the value of the random number, then the outgoing zenith ring has been found. The value of S'_{ij} is decremented by one zenith index and the search then continues using the original phase function to find the outgoing azimuth index m ,

$$S_{ij} = S'_{ij} + \sum_{m=1}^{N_\phi} P(i,j,s,l,m). \quad (5-13)$$

When S_{ij} surpasses the value of the random number, the outgoing angular bin has been found and is defined by the outgoing indices (s, l, m) . When this method is implemented on the test cloud field, an increase in performance of nearly 500 percent is realized, as shown in Table 3.

5.5 Cloud Bounding Box Intersection

As mentioned previously, the outer boundaries of a cloud are defined by a cloud bounding box (CBB). The CBB is a three-dimensional rectangular box whose dimensions exactly match those of the cloud shape array defining the cloud. It is the physical location of the CBB in the atmosphere which defines the location of the corresponding cloud. During the ray-trace process, rays will intersect one of the six CBB surfaces. It is not known in advance whether or not a given ray will intersect a particular cloud. For each ray, a search must be carried out over all clouds to check for a possible intersection. If the ray intersects more than one cloud, only the nearest is chosen. The ray-trace model can become very sluggish in the presence of a large

number of clouds to search through. A CBB is made of six rectangular surfaces and so to check to see if a ray intersects the CBB, a check must be made with each of its six surfaces. Only if the ray strikes one of the six CBB surfaces does the ray intersect the cloud.

One method of acceleration has been to speed up this search process by placing a sphere around each cloud. Since a sphere is a single surface, it is much quicker to check for an intersection with this sphere than with the six surfaces of the CBB. The geometry is presented in Figure 5.3(a) where the diameter of the sphere is given by $D^2 = l_x^2 + l_y^2 + l_z^2$, where l_x , l_y , and l_z are the three dimensions of the CBB. It not even necessary to check for an intersection point with the sphere, since the only information needed is to know whether or not the vector V is pointing in the direction of the sphere. If V is not pointing towards the sphere, an intersection cannot occur. If V is pointing towards the sphere, then there most likely will be an intersection with the CBB. In this latter case checks are made to see if the ray intersects any of the six surfaces of the CBB. This final step is necessary, since when the ray enters the CBB, its exact entrance point must be known.

Figure 5.3(b) shows the relation of the unit ray vector V at point P with respect to the sphere with radius $R/2$ at point P_0 , where P_0 is at the center of the CBB. The vector V_0 is a non-unit vector extending from point P to P_0 . The angle θ represents the angle between V_0 and V . The angle θ_0 is the angle between vector V_0 and a line drawn from P tangent to the sphere. From the geometry in Figure 5-3(b), $\cos\theta_0$ is calculated as

$$\cos\theta_0 = \frac{\sqrt{|\vec{V}_0|^2 - \frac{D^2}{4}}}{|\vec{V}_0|}. \quad (5-14)$$

From the definition of the cosine, $\cos\theta$ is calculated as

$$\cos\theta = \frac{\vec{V} \cdot \vec{V}_0}{|\vec{V}| |\vec{V}_0|}. \quad (5-15)$$

The final and efficient method to see if an intersection exists between the ray and the sphere is to compare θ with θ_0 . If $\cos\theta > \cos\theta_0$ (or $\theta < \theta_0$) then the ray intersects the sphere, and further checks need to be made to determine which surface of the CBB (if any) the ray strikes. When this technique is applied to the test cloud field of Figure 4.16, an 18.64 percent improvement in performance is achieved, as indicated in Table 3.

5.6 Cloud Placement Pre-Processing

Another method for accelerating the ray-trace process deals with pre-processing the cloud positions to determine which clouds are located entirely or partially within a given atmospheric grid control volume. As discussed in the previous section, when a ray is traveling through a particular atmospheric grid cell, intersection checks must be made for each and every cloud. This is because the model does not know in advance which CBBs lie in the path of the ray. However, it is a waste of effort to check for intersections with those CBBs which are outside the current grid cell since the ray will intersect the cell wall before it ever reaches those CBBs. Thus it is efficient to make a list of which CBBs lie within each grid cell and to search for intersections only with those CBBs. This is referred to as cloud placement pre-processing. For each and every atmospheric grid cell, a search is made over all CBBs to see which ones have any portion of their volumes in that grid cell. Thus when tracing a ray, intersection checks need only be made with those CBBs in the current grid cell.

In order to show the effectiveness of this method, the atmosphere was divided into finer and finer grid systems. Figure 5.4 shows an example of the test cloud field of Figure 4.16 with a 3-by-3 grid system superimposed. Five studies were carried out with increasing grid resolution: 1-by-1, 2-by-2, 3-by-3, 4-by-4, and 5-by-5 grid cells. No vertical divisions were used in this particular study. For each case a ray trace was performed and the computer run times compared. An important parameter to keep in mind with this particular acceleration technique is the number of clouds per grid cell. This number determines how many times an intersection check must be made for a ray in a particular grid cell.

Figure 5.5(a) shows the mean number of clouds per grid cell as a function of the total number of grid cells into which the atmosphere has been divided. Recall that this scene is made up of 49 individual clouds. Notice that the number of clouds per control volume decreases in an exponential fashion with the number of control volumes. It should be expected that the model performance would be directly related to the number of clouds per control volume. As the number of clouds per cell grows smaller, there are fewer clouds to search for intersections. However a certain overhead is incurred associated with tracing a ray through a single atmospheric grid cell. Thus a break-even point may be anticipated beyond which the reduction in the number of clouds in a given cell does not compensate for the increased cost of ray-tracing through more grid cells.

Figure 5.5(b) shows the model performance in terms of millions of rays per hour as a function of the number of control volumes making up the atmosphere. The rate of tracing a ray through the model increases strongly up to the 3-by-3 grid system (nine control volumes) beyond which the model performance begins to degrade slightly. From Figure 5.5(a) it is apparent that beyond the 3-by-3 grid system the number of atmospheric control volumes begins to increase much faster than the associated rate of decrease of the number of clouds per control volume. Thus in Figure 5.5(b) the model performance ceases to increase past nine control volumes due to the added overhead of the much larger number of control volumes which do not contribute to a significant reduction in the number of clouds per control volume. From this result it is apparent that the model reaches peak performance at a grid size of 3-by-3 cells, which corresponds to an average of 5.44 clouds per grid cell. When the performance at this grid resolution is compared to the baseline model, the 3 by 3 atmospheric grid results in a 14.38 percent improvement in ray-tracing speed over the unaccelerated model. Thus in general an atmospheric grid size should be chosen which results in this number of clouds per cell.

When all of these acceleration techniques are implemented simultaneously, a ray-trace rate of 2.75 million rays per hour is achieved, giving a 2320 percent improvement over the unaccelerated model. This is a quite large improvement when compared to the improvements associated with each technique individually. However, it must be realized that each of the

techniques discussed applies to a completely different aspect of the radiation model. The model simulates a very nonlinear problem and thus these acceleration techniques should not be expected to work together in a linear fashion.

Chapter 6 Results

The purpose of this chapter is to present the results of applying the atmospheric radiation model developed in this research to various scientifically interesting problems. The objective of this research has been to study the effect on cloudy-scene BRDFs of varying cloud parameters. The first study of this sort has been to look at the effect of varying the mean horizontal cloud size in scenes made up of realistic cloud size distributions. The second study is of the effect of varying cloud optical thickness in similar cloudy scenes. Also associated with these studies is the calculation of the error in retrieved fluxes due to scene misidentification. Results have also been generated for direct comparison with experimental satellite data. Finally, the atmospheric radiation model has been integrated with a CERES end-to-end instrument model to simulate the instrument response to scanning a realistic earth scene.

6.1 Cloud Size Sensitivity Analysis

This section deals with a study of the sensitivity of BRDFs to mean cloud size. Eight partly cloudy scenes were created from a library of Landsat-based three-dimensional clouds. Each of these scenes has a 35 percent cloud cover over an ocean surface and a solar zenith angle of 45 deg. The wind speed above the ocean is 5 m/s. The clouds all have approximately the same vertical thickness and are composed of 100-m cloud elements. The cloud liquid water content (LWC) is 0.3 g/m^3 and the Mie scattering properties are for an effective particle radius of $5.56 \text{ }\mu\text{m}$ and a size variance of 0.111. The relative number of each individual cloud type is varied from scene to scene to change the mean scene cloud horizontal diameter.

6.1.1 Cloud Size Variation

Eight different scenes were analyzed, where the mean horizontal cloud size was varied from scene to scene. An equivalent cloud diameter is determined from the cloud horizontal area as $D = \sqrt{4A/\pi}$. Figure 6.1 shows the eight scenes where each is 30 by 30 km with the TOA at an altitude of 30 km. The individual clouds making up these scenes are cumulus clouds and

are based on Landsat imagery data, as discussed previously in Section 4.5.3. A total of twelve individual basis clouds were used to create these scenes by selecting different numbers of each cloud type to populate a given scene. The mean cloud diameter for a particular scene is thus an average over the various clouds making up the cloud field. The mean cloud sizes for this series range from 0.52 to 2.20 km. Once a given cloud size distribution was determined, the individual clouds of the distribution were placed randomly throughout the scene. The local x-axis of the cloud was oriented in a randomly chosen direction in the plane parallel to the earth's surface at that point. Once the cloud was located a check was made to see if the cloud extended beyond the boundaries of the domain or overlapped a previously placed cloud. If either of these conditions was true, another random position and orientation were chosen. This process was continued until an appropriate location was found for which no overlap occurred. The largest clouds were placed first and the smallest were placed last.

One of the stated goals of this research is to characterize the effect of variations in three-dimensional cloud parameters on the calculated earth-atmosphere BRDF. The scenes shown in Figure 6.1 were chosen to show the extremes in cloud three-dimensionality effects. The mean cloud size in the first scene was chosen to show maximum cloud-to-cloud interactions, as indicated in Figure 6.2(a). In this case a ray from the sun will have very little chance of directly reaching the underlying ocean surface and will instead be scattered by one or more clouds. The other extreme, shown in Figure 6.2(b), was chosen so that a large fraction of the solar energy strikes the ocean surface and perhaps never encounters a cloud. These two extremes are expected to show very different angular properties since the ocean surface and clouds reflect radiation very differently.

Figure 6.3 shows how individual clouds were created for this study. A particular cloud is selected from Landsat imagery data, shown in Figure 6.3(a), and extracted to form an isolated cloud. It is assumed that the clouds have a uniform density, a flat bottom surface, and are free of interior voids. Thus the optical thickness from the Landsat data is directly related to the height of the upper cloud surface. Figure 6.3(b) corresponds to the top view of a three-dimensional isolated cloud. The purpose of this particular study was to observe the effect on the

BRDF of varying the *horizontal* cloud size, which made it necessary to maintain all other parameters constant. Therefore, in addition to forcing the cloud cover to remain constant at 35 percent, the cloud vertical thickness was also forced to be constant at a value of 350 m, or an optical thickness of approximately 30. This was done by taking the isolated clouds from the Landsat data and processing them to eliminate as much as possible the horizontal variations in vertical thickness. The result is shown in Figure 6.3(c). While this process results in clouds which are not as realistic as the original clouds, it was a necessary step for the purposes of this aspect of the study. In nature, cumulus cloud vertical thickness is seen to increase with cloud width (Plank, 1969). However, if this cloud flattening had not been done, it would have been difficult to determine the exact cause of observed results since they would be biased with respect to cloud size. Realistic small clouds would be thinner and so reflect less radiation.

Figure 6.4 shows the cloud size distributions for scenes 1, 5 and 8 of Figure 6.1. Each symbol type in this figure corresponds to the clouds of a given scene. Each data point corresponds to the total number of clouds of that size used to populate that scene. For example, the square symbols represent the numbers of each cloud type used to populate scene 1 (which has an average cloud size of 0.52 km). The first square data point is for the smallest cloud with a diameter of 0.32 km and shows that approximately 600 clouds of this size were placed in scene 1. The last square symbol shows that only one cloud of size 2.25 km was placed in scene 1.

Notice that the vertical axis is logarithmic, and that the data points follow a straight line in this figure. The cloud distribution is forced to be logarithmic here based on the work of Plank (1969) who observed that the cloud number density will in general increase logarithmically as cloud size decreases. In other words, there will typically be many more small clouds in the sky than larger ones. The mean cloud size and percent cloud cover can only be specified once the individual basis clouds have been selected and the assumption of logarithmic size distribution has been made. The mean cloud size of a given distribution is adjusted by changing the slope of the logarithmic cloud size distribution and the cloud cover is adjusted by varying the area under the straight line defining the size distribution.

6.1.2 Albedo Sensitivity

Each of the eight scenes was analyzed using the atmospheric ray-trace model. The result from these analyses is the radiation field at the TOA, which may be interpreted in a number of ways. The first is to look at the albedo of the earth-atmosphere system, where the albedo is defined as the fraction of the incident solar flux which is reflected back into space. The albedo was calculated from the radiation field for each of the eight scenes and is presented in Figure 6.5 as a function of the mean cloud size along with a linear regression through the data points. The results indicate that the albedo decreases steadily from approximately 0.55 down to 0.44 as the mean cloud size ranges from 0.52 km to 2.20 km. The slope from the linear regression may be interpreted as the sensitivity of the scene albedo to the mean cloud size and was found to be -0.0648 km^{-1} . The correlation coefficient from this regression is $R^2 = 0.8734$.

This trend in the albedo is most easily understood while referring back to Figure 6.2, which shows how the change in mean cloud size can affect the manner in which radiation is reflected from a cloud field. A smaller cloud size means that the incident solar radiation is more likely to strike a cloud top or cloud side than the ocean surface. At the larger cloud sizes, the gaps between the clouds are relatively larger, thus allowing more radiation to arrive at the surface of the ocean and be absorbed. Clouds are in general much more reflective than the ocean surface, and thus the effect of having a scene populated with a larger number of small clouds is to increase the *effective* cloud cover for that scene. This in turn results in a higher fraction of energy reflected from the cloud scene.

Notice in Figure 6.5 that the albedo data points do not follow a continuously decreasing pattern. In fact, a significant amount variability in the albedo results is apparent. This is due to the varying degree of homogeneity in each of the eight scenes. The smaller-cloud-size scenes result in a much more uniform distribution of clouds across the scene. The larger-cloud-size scenes in turn have a higher degree of statistical variance simply because of the smaller cloud population. It is expected that results for the larger-mean-cloud-size cases will have a higher degree of uncertainty in their results.

6.1.3 BRDF Sensitivity

The BRDF is another way of interpreting the predicted radiation field. The BRDFs for each of the eight cloudy scenes are shown in Figure 6.6. Recall from Subsection 1.4.1 that the BRDF is a tool to account for the anisotropy of the observed radiation field in the flux retrieval process. The BRDF is essentially the intensity from the radiation field normalized by the intensity from an equivalent diffuse scene with the same albedo. If the value of the BRDF at a particular observing direction is 1.5, that particular scene is then reflecting 1.5 times as much energy in that direction as a diffuse scene having the same albedo would reflect in that same direction.

Several trends may be noticed in the BRDFs presented in Figure 6.6. Note that in each case the solar radiation is incident at a zenith angle of 45 deg and an azimuth angle of 0 deg, as indicated on each of the BRDFs by the small sun symbol. Given this solar angle, a specular reflection from the ocean surface would result in a reflection peak at a zenith angle of 45 deg and an azimuth angle of 180 deg. The specular peak is virtually nonexistent for a mean cloud size of 0.52 km, while it is very strong for a mean cloud size of 2.20 km. This trend is a result of the same factors that affected the albedo as discussed in the previous section. The scenes with the smaller clouds present a higher effective scene albedo and thus reflect most of the incident energy from clouds rather than from the ocean surface. Clouds do not reflect energy specularly, but instead reflect energy via multiple Mie scattering events inside the cloud. The scenes with larger clouds tend to have extensive gaps between the clouds and thus allow a much larger fraction of energy to reach the ocean surface. While the ocean absorbs close to 90 percent of the incident energy, the fraction that is not absorbed is reflected in a specular fashion (but is diffused slightly from the specular spike because of the wavy ocean surface). This explains the large specular peaks for the larger mean cloud sizes.

Another interesting trend to observe in Figure 6.6 is the increase in rearward limb brightening with increasing mean cloud size. Limb brightening occurs when a scene appears brighter when viewed from a shallower angle, as illustrated in Figure 6.7. This is indicated by

the increase in intense red color at the bottom of the individual BRDF figures for the larger cloud sizes. The limb region of the BRDF represents the horizon and in this case indicates energy reflected from the scene at very shallow zenith angles (for any azimuth angle). Limb brightening occurs naturally in clear sky scenes as a result of Rayleigh scattering. In this case the feature is intensified by the brightly lit cloud sides which can reflect solar energy in the rearward direction. This reflected radiation does not contribute to the rearward limb brightening for small mean cloud sizes because it is most likely to strike another cloud before it can escape the atmosphere. In the case of large clouds, the wide gaps in the cloud field allow for more energy in this direction to contribute to limb brightening.

The BRDF sensitivity may be approximated by performing a linear regression only slightly more complicated than that for the scene albedo. Consider that for each possible viewing direction in the zenith angle/azimuth angle spherical coordinate system, a single data point (BRDF value) exists corresponding to each of the eight scenes. A linear regression was performed on the eight data points corresponding to each scene in this coordinate system, and the resulting slope interpreted as an approximation to the BRDF sensitivity to mean cloud size. This regression implies an assumption that the BRDF of these cloudy scenes follows a linear trend similar to the albedo shown in Figure 6.5. Figures 6.8(a) and 6.8(b) show the BRDF sensitivity to cloud size and correlation coefficient, R^2 , each as a function of viewing direction.

The results indicate that the BRDF is most sensitive to mean cloud size in the forward reflecting specular peak region. This is expected since this is the region where the BRDF changed the most across the range of mean cloud sizes. Between zenith angles of 60 deg and approximately 80 deg the BRDF also shows a strong negative sensitivity to mean cloud size. The nadir and extreme limb regions show moderate positive BRDF sensitivity to cloud size. The region with zero sensitivity occurs near a zenith angle of 60 deg for almost the entire range of azimuth angles. This observation corresponds to the model predictions of Davies (1984) who noticed the least amount of BRDF variation at this angle for observations of cumulus and stratus clouds.

The correlation coefficient indicates that only certain viewing directions followed a linear variation with respect to mean cloud diameter. These regions are the nadir and specular reflection area, and the ring slightly elevated above the limb. This ring corresponds to the similar ring of negative sensitivity in Figure 6.8(a). Between the two areas of good correlation is a thinner ring with values of R^2 approaching zero. It is noted that the region of low correlation to a linear regression corresponds to the region of zero sensitivity. It is currently unknown if this has some physical significance or if it is merely a coincidence.

6.2 Optical Thickness Sensitivity Analysis

A second sensitivity study was done to observe the effect of changes in mean cloud optical thickness on both the scene albedo and scene BRDF. Cloud field number 4, with a mean cloud size of 1.05 km, from Figure 6.1 was chosen as the baseline cloud field. This scene was selected because it was centrally located in the range of mean cloud sizes. Recall from Section 6.1 that the clouds in the cloud size sensitivity analysis were composed of 100-m elements. For the optical thickness study of the current section, this cloud element size was maintained; however, the cloud liquid water content (LWC) was varied from 0.013 to 0.6 g/m³ to produce a mean cloud optical thickness variation from 1.12 to 51.0. The mean cloud optical thickness is calculated by integrating the vertical optical thickness across the area of the cloud. The values of LWC and optical thickness are given in Table 4. The cloud LWC used in the cloud size sensitivity analysis was 0.3 g/m³, which is typical for cumulus clouds. Variations in the scene albedo and BRDF are expected as the variations in the optical thickness allow for more or less radiation to pass through the clouds and reach the ocean surface below.

6.2.1 Albedo Sensitivity

Figure 6.9 shows the scene albedo as a function of mean cloud optical thickness for the cloud field 4 shown in Figure 6.1. Each of the six data points corresponds to the model-predicted results for different mean cloud optical thickness. The LWC of the cloud elements used to construct the clouds in each of these scenes was varied to produce the variation in mean

cloud optical thickness. The important feature to note in Figure 6.9 is that the albedo varies in a logarithmic fashion with the cloud optical thickness. The higher optical thicknesses reflect more radiation from the scene simply because of the increased number of scattering events inside the clouds. The thinner clouds allow more radiation to pass completely through to be absorbed by the ocean.

In Subsection 6.1.2 the albedo sensitivity to mean cloud size was found through a linear regression of the data because there appeared to be a near linear relation between the albedo and the cloud size. Thus the sensitivity in that case was approximated with the slope from the linear regression. In the current case the albedo varies logarithmically with mean optical thickness; thus a regression was performed based on the relation

$$\omega = A + B \log u, \quad (6-1)$$

where A and B may be interpreted as the intercept and slope, respectively, when the data are displayed on a log-linear plot, as in Figure 6.9(a). The sensitivity of the albedo to optical thickness may be obtained by differentiating Equation 6-1 with respect to the optical thickness, u. This gives

$$\frac{d\omega}{du} = \frac{B}{u \ln(10)}, \quad (6-2)$$

where the only parameter from the regression to appear in the sensitivity is B, which was found to be 0.139. This expression tells us that the albedo sensitivity to cloud optical thickness varies inversely with optical thickness and linearly with the parameter B. Figure 6.9(b), which shows Equation 6-2 applied to the data of Figure 6.9(a), indicates that as a cloud becomes optically thicker, the albedo sensitivity to cloud optical thickness decreases.

6.2.2 BRDF Sensitivity

Figure 6.10 shows the BRDFs calculated for each of the data points in Figure 6.9. The range of variation in the BRDF for this study is much larger than for the cloud size sensitivity analysis of Section 6.1. Notice here that the forward reflecting peak becomes much weaker with increasing cloud optical thickness. This is a result of the clouds allowing more radiation to pass directly through and reflect from the ocean surface. As the clouds become thicker they reflect more radiation in all directions, thereby creating a more diffuse BRDF. Another very important trend is to note that the limb brightening shifts its peak from the forward direction to the rearward direction with increasing optical thickness.

As mentioned earlier, a large part of the limb brightening effect is due to the Rayleigh scattering present in the atmosphere. In this case however, clouds are also playing an important role as well. The thinner clouds allow more radiation to pass directly through the clouds instead of reflecting back in the rearward direction. For example, the case for optical thickness of 51.0 in Figure 6.10 results in a large fraction of the energy striking the incident face of the clouds and then reflecting rearward towards the horizon. For the case of optical thickness 1.12, most of the energy striking the clouds passes through and causes in part the very intense forward limb brightening. The color scale in this case is misleading since the range of 0.50 to 2.25 was chosen to give good coverage over the entire range of the six cases. For optical thickness equal to 1.12, the actual peak value of the BRDF was slightly over 3.6 in the forward limb brightening region, which was significantly higher than either the specular reflection peak or the rearward limb brightening.

The logarithmic regression of Equation 6-1 was also applied to each viewing direction bin of the BRDFs from Figure 6.10, in the same manner as the sensitivity calculation of Section 6.1. The slope of this regression is shown in Figure 6.11(a) as a function of viewing direction. This factor is not the sensitivity of the BRDF to cloud optical thickness, but it is related to it with an expression similar to Equation 6-2. The BRDF sensitivity parameter is a set of two-dimensional data; thus the BRDF sensitivity to cloud optical thickness is a three-dimensional volume of

information because of its variation with optical thickness, which is impractical to illustrate on paper.

Figure 6.11(b) shows the correlation coefficient, R^2 , of the regression used to obtain the data in Figure 6.11(a). Almost the entire region of this figure shows a high-degree of correlation except for a small ring-like region at zenith angles near 75 deg. The nadir portion shows a high degree of correlation since there is essentially no change in the BRDF as a function of cloud optical thickness. This can be seen by referring back to Figure 6.10, where the nadir region exhibits an almost constant value slightly higher than 0.5. The other region of high correlation is the forward limb region and, to some degree, the forward specular reflection peak from the ocean surface. This area represents radiation which has passed through the cloud field and then been scattered towards the forward limb or the ocean surface. This radiation was scattered according to the equation of transfer, Equation 3-13. Since this equation has an exponential factor with optical thickness applied to the incident intensity, the amount of radiation passing through a cloud *should* vary in an exponential (logarithmic) fashion. This explains the strong correlation of the regression for both the albedo and the forward limb area of the BRDF.

6.3 Scene Misidentification Error

The sensitivity analyses discussed in the previous section are the primary results of this research. However, it is also important to understand the implications of the values of the BRDF sensitivities. For example, what does the sensitivity information tell us about our ability to retrieve fluxes from a given scene? In order to answer this question a study was done where the BRDF calculated from the radiation field of one scene was used to retrieve fluxes from a second different scene of a slightly different composition but having the same percentage cloud cover. Fluxes were retrieved using Equation 1-5 in all observing directions of the hemispherical space. The retrieved fluxes were then compared to the true flux for that scene and a percent error was calculated as a function of observation direction. This type of analysis was done with the data sets considered above in the two sensitivity analyses. This made it possible to quantify the effect of misidentifying the mean cloud size or mean cloud optical thickness in a given scene.

6.3.1 Misidentified Cloud Size

For the first part of this study the cloudy scenes from the cloud size sensitivity analysis have been used to predict the error due to cloud size misidentification. Specifically, the BRDF corresponding to the 0.52 km mean cloud size was used to retrieve fluxes from each of the eight scenes in all viewing directions. Each of these scenes has the same cloud cover and same cloud microphysical properties. The only variation among these scenes is the mean cloud diameter. Figure 6.12 shows (as a function of viewing direction) the percent error between the retrieved flux and the actual flux as calculated from the ray-trace model results. Referring back to Figure 6.6, notice the significant changes in the BRDF as the mean cloud size increases from 0.52 km up to 2.20 km. As discussed earlier, the most striking feature to observe here is the forward specular peak and the rearward limb brightening, both of which vary strongly as a function of cloud size. Thus errors are to be expected when using a BRDF from a particular scene with a certain angular distribution of reflected radiation to predict the reflected flux from another scene with quite different angular radiative properties. The large positive error in Figure 6.12 for a mean cloud size of 2.2 km occurs because the BRDF used to predict the reflected fluxes from this scene was not able to account for the strong specular peak. The error for the first scene is zero at all observing angles since the BRDF used to retrieve fluxes from this scene was derived from the radiation field of that same scene. The error also increases in the negative direction with increasing cloud size for zenith angles near 75 deg at all azimuth angles. This can be accounted for by the decreasing amount of cloud-scattered radiation which is instead reflected from the ocean surface in the specular peak region.

6.3.2 Misidentified Cloud Optical Thickness

The second scene misidentification study was carried out using cloud scenes with varying optical thicknesses. The radiation field from the cloud field with a mean optical thickness of 51.0 was used as the source of the BRDF used to retrieve fluxes from each of the six scenes. The results are shown in Figure 6.13, where the percent error ranges from -20 to 80. In the previous section the peak error was associated with the specular reflection peak. The results for

cloud optical thickness show a slightly different result. Here, while the specular region does have a strong associated error, the maximum error is in the forward limb brightening region, which corresponds to the maximum BRDF peak in Figure 6.10 of the cloud optical thickness study. Another trend is that the nadir region shows a significant negative error for lower optical thicknesses. The error for the scene with a cloud optical thickness of 51.0 shows zero percent error since this scene was the basis for the BRDF used to retrieve fluxes from each of the scenes.

6.4 Model Comparison with the Along Track Scanning Radiometer

The Along Track Scanning Radiometer (ATSR) is an instrument operated by the Rutherford Appleton Laboratory in the United Kingdom. It produces images of the earth at a 1-km spatial resolution. The data from these images have a wide variety of applications, of which the primary is to detect changes in global sea surface temperature. The sea is a huge thermal energy reservoir and plays a key role in determining the climate of the planet. Long-term reliable measurement of the ocean temperature is necessary to establish whether or not global warming is really taking place. It is also very useful for predicting and correlating the El Niño events.

A unique aspect of the ATSR instrument is that the instrument makes two independent measurements of the same earth scene from two different viewing directions. As the satellite progresses in its orbit it is able to image a given scene from multiple directions over a time interval that is essentially negligible compared to the times scales over which atmospheric changes occur. Figure 6.14 shows how the ATSR instrument is able to produce the forward view of a scene as it approaches and then the nadir view as it passes directly above the scene. The purpose of the dual-view design of ATSR is that it is possible to estimate the ocean surface temperature by giving more information about the effects that the intervening atmosphere may have on the radiation leaving the ocean surface. The ATSR instrument scans at four wavelengths: 0.55, 0.85, 1.6 and 11 μm . The resulting data from the ATSR mission contains a large amount of cloud data, and a number of researchers, for example Watts (1995), are trying to use these data to extract useful information aside from their primary ocean surface temperature measurement objective.

6.4.1 ATSR Data Sets

Figure 6.15 shows examples of two of the ATSR data sets used in this comparison analysis. These two images were taken over the Atlantic ocean and the local time of day was such that the solar zenith angle was 68.2 deg. Figure 6.15(a) shows the cloud height obtained from the nadir view using the 11- μ m thermal channel. This was done (Watts, 1995) by converting the thermal intensity into a temperature assuming the clouds emit as black bodies. The temperature in the troposphere decreases with altitude at a steady rate of about 10 K/km. This is known as the environmental lapse rate. The ocean surface temperature was obtained from the clear sky portions of the thermal image. Starting with this temperature and using the lapse rate, it is possible to associate a temperature with every altitude. This allows the measured cloud temperatures to be converted into the cloud top altitude above sea level. The resolution of the ATSR instrument gives a pixel size of 1 by 1 km in the nadir view. The image in Figure 6.15(b) is the intensity measured in the forward view of the same cloud scene at a wavelength of 0.55 μ m. The zenith angle to the satellite was 54.5 deg and the satellite was essentially in the plane defined by the ocean surface normal and a vector from the scene to the sun. In other words, the sun was illuminating this scene from almost directly behind the satellite. The basis of this comparison is that a model cloud scene is created based on the cloud morphology information from Figure 6.15(a) and the ray-trace model is used to predict the forward view in Figure 6.15(b).

6.4.2 Reproduction of Cloud Fields from the ATSR Nadir View

The cloud geometry for inclusion in the atmospheric radiation model was obtained from the thermal data in Figure 6.15(a). The clouds in these images were assumed to be maritime cumulus clouds and the typical cloud optical properties associated with these types of clouds were used to calculate the cloud element scattering phase function. Initially it was thought that the cloud element size would be determined by the 1 km resolution of the nadir cloud height image. However, the cloud height ranged from 0 to 3.85 km, and thus a cloud element size of 1 km gave a very poor vertical resolution. Therefore it was decided to use a 250 m cloud element size for the sole purpose of improving the vertical resolution. The cloud field in Figure

6.15(a) was subdivided into four individual clouds and their cloud height information exported to separate data files. The vertical columns corresponding to each 1-km pixel were further subdivided into 16 subpixels to allow for the 250-m cloud elements. Cloud elements were then stacked in each column until the cloud-top height was reached. Figure 6.16 shows a two-dimensional hypothetical example of how this was done. Aside from the pixel subdivision, this process is similar to that used for processing the Landsat image data in previous sections. The only other difference is that the Landsat data were in terms of vertical cloud optical thickness, while the ATSR data are in kilometers to cloud-top height.

The actual and model cloud fields corresponding to the four clouds are shown in Figures 6.17(a) and (b), respectively. The cloud bounding boxes (CBB) are also shown. The solar energy is incident to this scene from the bottom portion of the image at a zenith angle of 68 deg. Several cloud features from the ATSR data were not included for the sake of simplicity. These include the small clouds at the lower left corner, the small clouds along the right edge, and the portion of a cloud at the upper right cut off by the top edge of the field of view. Also the tail at the lower-right of cloud 3 was not included since it was much thinner than the rest of the cloud field.

6.4.3 Model Results and Comparison with ATSR Forward View

The cloud field discussed above was placed inside an atmosphere with dimensions 110 km by 100 km horizontally and 30 km vertically. These horizontal dimensions are exactly twice the ATSR nadir field-of-view dimension. This size was chosen instead of the original field-of-view size itself because of the cyclic boundary conditions implemented by the model. Recall from Section 4.3 that these boundary conditions essentially result in edges of the atmosphere being windows into exact duplicates of the model scene. Thus a larger atmosphere was chosen to create a scene which completely isolated the cloud field from copies of itself. This ensures that the radiation field predicted above the cloud field results solely from the clouds in the scene and are minimally affected by the lateral boundary conditions. A surface wind speed of 5 m/s was assumed.

A total of 50 million rays were required to achieve convergence in both the reflected flux and the intensity anisotropy on a per-TOA-element basis. The TOA reflected flux calculated from the model-predicted radiation field is shown in Figure 6.18. The flux values range from 50 to 350 W/m². The minimum value occurs in the dark blue shadow region at the top portion of the figure. Recall that the radiation field is calculated at the TOA itself, and thus this dark blue region is due to the shadow cast by the clouds onto the ocean surface and which is then reflected up to the TOA. The maximum in reflected flux is due to the energy reflected from clouds 1 and 2 (refer to Figure 6.17(b)). These two clouds together form a horizontally extensive region of cloud which then intercepts and reflects a large amount of solar radiation. It is evident from this result that the four-cloud system is well-isolated from the cyclic boundary conditions. If the atmosphere had been any smaller then the shadow region near the top of the figure would have been passed through to the lower portion of the figure.

In order to compare the model results with the ATSR forward view, the predicted TOA radiation field must be processed in such a way as to produce an image of the scene from the satellite point of view. The ATSR forward view image shows the intensity arriving at each pixel of the instrument sensor from the earth scene. The results from the ray-trace model are in the form of the intensity leaving the atmosphere at each TOA element and through each angular bin above that TOA element.

A technique has been developed to predict the image of an earth scene which an observer located at a given point in space would see if they were looking through a virtual screen at the earth. Figure 6.19(a) shows an example of how this virtual screen is defined in front of the observer location; note that the virtual screen is subdivided into a large number of pixels. The result of this technique is the intensity passing through each pixel from a solid angle originating at the observer point and subtended by the area of the pixel. In order to determine this, a reverse Monte-Carlo ray trace is performed (Turk, 1994) on a pixel-by-pixel basis where rays are traced from the observer point in a direction randomly determined within the solid angle subtended by that pixel. Each ray is traced down to the earth scene where it intercepts an element of the TOA grid as shown in Figure 6.19(b). The angular bin above the TOA element through which the ray

arrives can be determined from the geometry of the TOA, the virtual observer location, and the vector of the ray, as shown in Figure 6.19(c). The radiation field (which has already been calculated) is then evaluated to determine the intensity which is leaving the TOA in the direction of the ray traced from the virtual screen. This intensity is then used to update the value of the intensity for the current pixel of the virtual screen. This process is repeated for a sufficient number of rays for each pixel until a virtual image is produced of a portion of the earth scene.

This tool has primarily been used for diagnostic purposes to view the atmospheric model results during the development phase. Typical radiation fields can take upwards of 50 megabytes of disk space, which represents a staggering amount of information. This virtual screen is a means of exposing very detailed information about the scene content not available from the BRDF or the TOA flux. Each of these latter two products is a result of integration of the radiation field over either a spatial variable or angular variable. The virtual screen does not do any of this; instead it is literally a window into the heart of the results produced by the atmospheric ray-trace model.

Figure 6.20(a) shows the ATSR forward view, and the model-predicted forward view is shown in Figure 6.20(b). The first thing to note here is that the two images are remarkably similar in terms of the spatial distribution of reflected energy. They both show high levels of intensity at similar locations in the cloud field. These correspond to both thick and brightly lit portions of the cloud field. Note, however, that the color scales of these two images do not range over the same values of intensities. The ATSR image intensity ranges from 50 to 250 W/m²/sr, while the model predicted image ranges from 50 to 450 W/m²/sr.

The difference in scales between these two images does not invalidate the ray-trace model. A large number of assumptions were made in the process of re-creating the ATSR cloud field and then analyzing it to produce the predicted TOA radiation field. The most important is probably the assumption of typical cloud optical properties. This was done since the ATSR instrument, and the later data processing, are not able to retrieve these types of information. Instead, as mentioned earlier typical cloud properties were obtained from the literature. Clouds

can vary quite significantly in terms of their physical properties even inside a single cloud, let alone across an entire cloud field.

Another potential source for the differences in these two images is the procedure used to re-create the cloud morphology. The procedure used in extracting clouds from the Landsat images would most likely have resulted in more accurate clouds. Recall that the Landsat data were in terms of vertical cloud optical thickness. Thus it was possible to stack cloud elements (for which the optical depth is known) in vertical columns for each Landsat pixel until the Landsat optical depth was reached. The process for the ATSR data on the other hand was essentially to stack up the cloud scattering elements at each ATSR nadir-view pixel until they reached the cloud-top height. The problem with the ATSR technique is that the cloud optical properties were one step further removed from the end result of the cloud morphology. The Landsat optical thickness is a direct measure of the cloud amount at each image pixel. The ATSR cloud height does not reliably give this information; instead, an assumption had to be made about the cloud properties before the cloud amount could be determined.

One possible solution to this problem would be to iterate with a predicted nadir view at a given wavelength. The mean cloud optical properties would be varied until the predicted nadir view matched the ATSR nadir view. The forward view could then be predicted at a different wavelength and compared with the corresponding ATSR view.

6.5 Integration of the Atmospheric Radiation Model with the CERES End-to-End Dynamic Electrothermal Instrument Model

The ERBE and CERES satellite-borne radiometric instruments are key components of NASA's Earth Observing System (EOS), whose initiative is to advance scientific understanding of the earth by providing global observations of the atmospheric and oceanic environments. High-level dynamic electrothermal models of these instruments have been created by the Thermal Radiation Group through long-term NASA funding.

The instrument model consists of several different components. A Monte-Carlo ray-trace model (Meekins, 1990; and Bongiovi, 1993) is used to characterize the radiative transfer of energy through the optical system of the instrument. A finite difference model was developed by Haeffelin (1993) to calculate the thermal and electric fields inside the instrument sensor, a thermistor bolometer. A numerical model of the ERBE electronic bridge circuit was also developed to calculate the voltage output from the ERBE instrument given the power distribution on the surface of the sensor. The radiative, thermal, electrical, and electronic models were integrated (Haeffelin, 1993) to produce an end-to-end model of the complete instrument. The circuit model was later updated (Priestley et al., 1995) to the newer CERES detector bridge circuit, which along with an updated radiative model (Bongiovi, 1993), resulted in an end-to-end CERES instrument model.

An effort is currently underway (Haeffelin, 1996) to characterize the ERBE and CERES instrument sensitivity to various parameters such as scene equivalence, multi-channel co-alignment, and various components of the electrothermal model. As part of this effort it is desired to understand the instrument response as it scans across a realistic earth scene. In order to achieve this goal, the atmospheric radiation model developed during the current research was integrated with the instrument end-to-end model by post-processing the model-predicted TOA radiation field to determine the power input to the instrument aperture. In addition to showing some initial scientific results of the model integration effort, a secondary goal is to demonstrate the capabilities of this integrated model. The results shown here include a study of the bidirectional effects on the instrument response as it scans a given scene from several different observation points.

6.5.1 Mosaic Scene Construction

Realistic scenes for this study were created by patching together a sequence of smaller scenes to create an extensive mosaic scene. This mosaic process was necessary because of the high TOA spatial and angular resolution required. A region scanned by the instrument can extend to over one thousand kilometers, but is at most 50 kilometers in width. It would have

been prohibitively time consuming to create an atmospheric model of this size at the required resolution. Thus a limited number of 50-by-50-km cloudy earth scenes were generated and then fitted together in various sequences to create long sections of earth atmosphere which could then be scanned by the instrument model. Another benefit of this technique is that this small number of individual scenes, or "frames", can be put together in many different sequences to create a large number of mosaic scenes. Figure 6.21 shows the five scenes used for this study. Cloud types are both stratocumulus and cumulus. The cloud cover ranges from 10 percent to 30 percent. One of the scenes is simply clear sky over ocean. Each of these scenes was introduced into the atmospheric ray-trace model for a solar zenith angle of 45 deg and an underlying ocean surface with a wind speed of 5 m/s.

Figure 6.22 shows the complete mosaic scene made from multiple copies of the individual scenes of Figure 6.21. In the figure the scene is broken into two sections so that it will fit one page; it is scanned by the instrument as a single continuous scene. In all cases to be discussed in the following sections, the scans start at the bottom of the first mosaic section (0 km) and end at the top of the second section (500 km). Typical CERES scans are from the west to the east across the track of a polar (north-south) orbit. Thus the bottom of the mosaic scene corresponds to a westward direction and the top to an eastward direction. The angle of incidence of the solar radiation in each of the five basic scenes corresponds to a local time of 8:00 am. The sun is located at a 45-deg zenith in the due east direction (top of the page).

One of the purposes of this section is to illustrate the bidirectional effects of the anisotropic radiation field reflected from a broken cloud field mosaic scene. This scene was scanned from three different positions corresponding to a satellite scanning the same portion of the earth (at the same local time) from consecutive 800-km altitude polar orbits. This is indicated schematically in Figure 6.23 which shows the three satellite positions and the corresponding scan geometry relative to the scene.

6.5.2 Scene Analysis for Input into Instrument Model

The input information required by the instrument radiative transfer model is the collimated power incident to the instrument aperture from many different directions. This can be interpreted as the image of the earth the instrument sees from the aperture. Thus it was a simple process to use a technique similar to the virtual screen process described in Subsection 6.4.3 to calculate the radiation power field incident at the aperture. The virtual screen technique was described with reference to Figure 6.19. The only difference for calculating the aperture radiation field was to redefine the concept of the virtual screen, which was specified by a spatial discretization in a rectangular plane in front of the observer. The aperture radiation field was calculated by discretizing the angular field of view (1.8 deg in the scan direction and 2.8 deg in the cross-scan direction) into a finite number of angular bins. Thus the main difference between the two methods is that one uses a spatial discretization and the other uses an angular discretization. The end results are similar.

An additional step with the aperture study was that a large TOA grid was defined to fit over the top of the entire mosaic scene (500 by 50 km in this case). This was necessary for tracing rays from the aperture to the mosaic scene. These rays first intersected this larger TOA grid, and from this information it was possible to determine which underlying basic scene the ray had hit. Only then could the proper aperture radiation field angular bin be updated by the power from the TOA radiation field.

As indicated in Figure 6.23, the scans start at one end of the mosaic scene and go completely to the other end. The instrument scan process was simulated by calculating the aperture radiation field at every millisecond along the scan. The CERES instruments scan at a rate of 63.5 deg/s, which results in over 500 1-ms updates of the aperture radiation field in this simulation. Figure 6.24 shows two examples of the aperture input data, which can be interpreted as images of the earth scene from the instrument point of view. These two images correspond to the instrument looking at the same TOA point from satellite positions 1 and 3. This point is indicated in Figure 6.23 as point A, which corresponds to a TOA coordinate of 425 km. Notice

that the units of the data in these images are microwatts. Although the instrument is focused on the same point from each point of view, the actual scene contents are slightly different because of the different satellite viewing zenith angles. Figure 6.24(a) shows the image of the earth scene at point A from satellite position 1, which is almost a nadir view. The bright areas in this figure are the brightly lit cloud tops and the dark regions are the ocean surface. Figure 6.24(b) shows this same scene but from the point of view of satellite position 3. The same cloud field can be seen, but now much more energy is reflected from the ocean surface to the observer. Notice also the dark shadows underneath the clouds. The clouds in these two scenes correspond to the cloud field of Figure 6.21(d).

The angular distribution of the power incident at the aperture can be averaged over the field of view to give an equivalent incident power. This average is weighted by the solid angle of each angular bin. This mean power is converted to an intensity by multiplying the solid angle field of view from the aperture and the area of the aperture opening. This represents the intensity reflected towards the instrument from the scene in the field of view. It is this intensity which the instrument is attempting to measure. Figure 6.25(a) shows this equivalent input intensity for each of the satellite orbit locations as a function of the observed position on the TOA. Each value of the equivalent intensity in this figure is directly a function of the content of the observed scene. Since the scenes in this analysis contain clouds over the ocean, the higher intensity values are due to larger amounts of sunlight reflected from the cloud tops and sides and from sun glint from the ocean surface. Note that the information in this figure is not the data actually introduced into the instrument model. The input into the model is the original aperture power radiation fields for each scan position similar to those shown in Figure 6.24. Figure 6.25(a) is simply shown to give an idea of the *mean* input into the model. Also, it is possible to compare the calibrated model output with these data.

6.5.3 Instrument Response

The time-series data of the aperture-incident power has been processed by the instrument optical model to determine the spatial distribution of power (as a function of time) on the instrument thermal radiation detector, which is a thermistor bolometer. These data were then introduced into the detector dynamic electrothermal model. The output from this model is a time-varying voltage signal which is a measure of the intensity arriving at the instrument aperture from the scan of the observed scene. This voltage signal was converted back into intensity via the model-predicted instrument calibration information. This intensity, or radiance, is shown in Figure 6.25(b) as a function of the observed position on the TOA. The data in this figure are the response of the complete instrument end-to-end model to scanning a realistic broken cloud field from orbit.

Figures 6.25(a) and 6.25(b) are shown on the same page to facilitate comparison between the two. The first feature to note is that much of the high-frequency information has been filtered out of the signal; the curves in Figure 6.25(b) are noticeably smoother than those in 6.25(a). Also, in Figure 6.25(b) the major peaks are slightly lower and the valleys slightly shallower than their counterparts in Figure 6.25(a). This is due to the fact that the instrument has thermal and electronic time delays and is thus inherently an integrator. The output has been corrected to account for the time delay by shifting the signal according to the point-spread function (Haeffelin, 1996).

The 500-km scene was scanned from each of the orbit positions shown in Figure 6.23, where the solar radiation is incident at a 45-deg zenith angle from the east. The differences between the three successive scans are due solely to the change in instrument location and scene-viewing angle. An example of these differences can be seen at a TOA position of 125 km. The satellite in orbit 3 is almost directly above this point and sees the brightly illuminated cloud top and a portion of the dark westward side. The satellite in orbit 2 no longer sees the dark side of the clouds and instead sees the bright eastern side. This results in the moderate jump in measured intensity at a position of 125 km from orbit 3 to orbit 2 in Figures 6.25(a) and (b).

The most obvious difference occurs near a TOA coordinate of 450 km at the end of the scanned scene. Here the intensity measured from orbit 3 is significantly stronger than from either orbit 1 or 2 due to the intense sun glint from the ocean surface reflecting up to the instrument.

Chapter 7 Conclusions and Recommendations

7.1 Conclusions

The stated objective of this work is to characterize the sensitivity of cloudy-scene bidirectional reflectivity distribution functions (BRDF) to several cloud parameters. This type of work is necessary for the creation of new BRDFs for use in remote-sensing applications. In particular this work has focused on NASA's earth radiation budget studies including both the Earth Radiation Budget Experiment (ERBE) and the Clouds and the Earth's Radiant Energy System (CERES). The BRDF is a tool in these programs necessary for the retrieval of earth-reflected shortwave fluxes from satellite intensity measurements. Major developments and conclusions from the study are:

1. The BRDF is used to account for the anisotropic nature of the shortwave radiation field. This anisotropy is a result of the very complicated processes to which the incident solar radiation is subjected before it is reflected back into space. Most importantly, this includes the effects of broken three-dimensional cloud fields. Clouds have traditionally been very difficult to model since they change very dramatically over several time and length scales. Many efforts have been made to model realistic cloud fields, but it is not until recently, with the advent of relatively low-cost super computers, that the type of work reported here has been possible. An approach which is ideally suited to cloud modelling is the Monte-Carlo ray-trace method.
2. Using the Monte-Carlo method a modular atmospheric radiation model has been created which permits the simulation of realistic three-dimensional broken cloud fields. This model has been used to predict the BRDF sensitivity to mean cloud size while maintaining constant all other parameters such as percent cloud cover and physical cloud properties. Results indicate that the BRDF sensitivity varies quite significantly with viewing angle, especially in the region of the forward reflecting peak from the ocean surface.. The sensitivity of the BRDF to cloud vertical optical thickness was

also studied in a similar fashion. The results here are very different from those in of the cloud size sensitivity study in that there is a higher sensitivity in the region of the forward limb brightening. In a related study, it was also possible to predict the effect of scene misidentification by using the BRDF from a given scene to retrieve fluxes from similar scenes. Errors as high as 60 percent may be realized for certain view angles in cases where the mean cloud size is severely misidentified.

3. A comparison with satellite experimental data was done using data from the Rutherford Appleton Laboratory's Along Track Scanning Radiometer (ATSR). Cloud-top height data from a nadir view of a scene were used to create a cloud field for input into the atmospheric radiation model. The top-of-the-atmosphere (TOA) radiation field was calculated and then used to predict a second view of this same scene. This predicted view was compared with the corresponding ATSR image. While the magnitudes of the predicted radiances were over-predicted by almost a factor of two, probably because of our ignorance of the clouds' water content, the relative distribution of reflected radiation matched very well.
4. Finally the model-predicted radiation field was integrated with a CERES radiometric end-to-end model to simulate the instrument voltage response to scanning a realistic partly-cloudy scene. This integrated model was used to illustrate the bidirectional effects of scanning a given earth scene from adjacent polar orbits. The results show significant differences between the different orbits, especially when the sun glint reflected from the ocean is visible from one orbit and not from the others. This study demonstrates the need to account for the anisotropy of the reflected radiation field, since the measured radiance can vary quite substantially with viewing direction for a given scene.

7.2 Recommendations for Future Work

7.2.1 Model Improvements

The Monte-Carlo ray-trace atmospheric radiation model as it currently stands is a very complex system. However, a number of areas still remain in which the model can be adapted, improved, and extended to give more accurate representation of the earth's surface, the atmosphere, and, of course, clouds.

1. The work reported here has focused only on the results for clouds above an ocean surface. This is because data for other surface types (land, snow, etc.) are presently unavailable in a format appropriate to describe the albedo and bidirectional properties of these surfaces. This is an area which needs further work since, while most of the earth's surface is ocean, the continents also play a major role in determining the earth's radiative energy budget.
2. Another area which has been neglected is the absorption of shortwave radiation by atmospheric gases and cloud water droplets. The spectral properties of the atmosphere, clouds, and the earth's surface are extremely rich in terms of the amount of variation for relatively small changes in wavelength. The future of remote sensing will lead to sensors capable of simultaneously imaging a scene in thousands of small wavelength bands. Thus it would be appropriate to include an atmospheric gaseous absorption model to account for wavelength-dependent absorption in the atmosphere. Mie scattering theory can be further applied to obtain the water droplet wavelength dependent absorption properties inside clouds in addition to cloud scattering properties.
3. Another area to be further developed in the model is the variation of cloud properties within the cloud. The model was created in a modular fashion to allow for such variations, but this feature has never been exercised. In part this is because of the large amount of storage required for a single cloud element scattering phase function,

thus making it difficult to load more than a single such phase function into memory at one time. However, this should be possible given access to sufficient computer resources and further refinements in modelling the cloud element scattering properties.

4. Scattering of shortwave radiation by aerosol particles has not been included in the current model. The transport of radiation through the atmosphere is significantly affected by aerosol scattering over many important wavelength intervals. This type of scattering is difficult to characterize because of the wide variations in particle geometry and chemical composition. However, this is an active research area, and it should be possible to include some type of aerosol scattering into this model in a manner similar to the treatment of Rayleigh scattering.
5. This model has been developed primarily to model three-dimensional cumulus and stratus clouds. Very little has been done to study high-altitude cirrus ice clouds. While these clouds are often very thin optically, they can have a significant effect on the earth radiation budget. Therefore some effort should be made to include cirrus clouds in the atmospheric radiation model. Since cirrus clouds are often thin and horizontally extensive, the cubic cloud element technique already developed might not be an appropriate tool. However, it should still be possible to include these types of clouds in the model to give the model complete description of the radiative properties of the earth's atmosphere.

7.2.2 Further Studies

The atmospheric model developed during this research has been applied only to a small fraction of the problems it is capable of analyzing. The model has primarily been used to study the BRDF sensitivity to cloud parameters. There exist many other problems which can be studied which are currently at the frontier of science.

1. The problem of anomalous cloud absorption has many implications for climate research and is a particular challenge for the radiative transfer community. This problem deals with the fact that space-based and ground-based measurements of earth radiation budget components are in consistent disagreement with traditional theoretical methods. It is felt that clouds are absorbing more radiation than theory is able to account for. If the model additions and modifications discussed in the previous section were to be implemented, the model would then be the ideal tool to investigate this problem.
2. Shortwave radiative fluxes that reach the earth's surface are key factors that influence atmospheric and oceanic circulations as well as surface climate. Yet, information on these fluxes is meager since surface data are available only from a limited number of observing stations over land and even fewer over the ocean. This problem is very closely linked to three-dimensional cloud fields since radiative cloud-to-cloud interactions can produce unusual bright and dark spots on the earth's surface. The model developed during this research could be a key tool in studying the shortwave flux at the earth's surface.
3. The comparison study with the Along Track Scanning Radiometer (ATSR) should be repeated with a different approach to determining the cloud morphology from the nadir view. In the current research the morphology was obtained from thermal-channel derived cloud-top height. Cloud properties were assumed and used to fill the shape defined by the cloud-top height. A better approach would be to use the 0.87 μm channel nadir view as the source for cloud morphology. This could not be done with direct conversion to cloud-top height, but instead an iterative approach could be used. A set of cloud parameters could be assumed and then analyzed by the model and the results then compared with the 0.87 μm data. Based on the differences, the cloud parameters could be changed and the cloud field analyzed again. This process could be repeated until the model-predicted 0.87 μm nadir view corresponded with the similar ATSR view. At this point the model could be used to predict the ATSR *forward* view

in the $0.55\ \mu\text{m}$ channel. The difference between the two images in this comparison would be a measure of the capabilities of the model.

4. Finally, further work could be done with the CERES instrument end-to-end model as it applies to BRDFs. Currently the end-to-end model has been used in this research to give the instrument response to a given scene. This response was calibrated into units of radiance. Since the viewing geometry is easily known as a function of scan angle, and the radiation fields have already been calculated for each of the scenes, it is entirely possible to apply the appropriate BRDF to the simulated instrument-measured radiance and retrieve a reflected flux from the observed scene. This flux could then be compared to the true flux for that scene and the difference studied as a function of instrument scan angle.

Tables

Table 1 The ERBE 12–scene classification scheme.

Scene	Surface Type	Percent Cloud Cover
1 2 3 4 5	Ocean Land Snow Desert Land–Ocean Mix	0 – 5
6 7 8	Ocean Land/Desert Land–Ocean Mix	5 – 50
9 10 11	Ocean Land/Desert Land–Ocean Mix	50 – 95
12	Overcast	95 – 100

Table 2 Typical cloud water droplet size characteristics (Liou, 1992)

Cloud Type	$r_{\text{eff}} (\mu\text{m})$	r_{eff}
Fair Weather Cumulus	5.56	0.111
Altostratus	7.01	0.113
Stratus	11.19	0.193
Cumulus Congestus	10.48	0.147
Stratocumulus	5.33	0.118
Nimbostratus	10.81	0.143

Table 3 Ray–trace model acceleration technique results.

Technique	Millions of Rays per Hour	Percent Improvement
Baseline	0.113378	
Surface Reflection	0.117337	3.49
Fractional Absorption		42.0
Cloud Phase Function	0.674937	495.3
Cloud Spheres	0.134512	18.64
Cloud Placement	0.129684	14.38
All	2.748931	2320.0

Table 4 Cloud liquid water content and corresponding optical thickness from sensitivity study.

Test Case	LWC (g/m ³)	Cloud Optical Thickness
1	0.013	1.12
2	0.0325	2.79
3	0.075	6.48
4	0.150	12.9
5	0.300	25.5
6	0.600	51.0

Figures

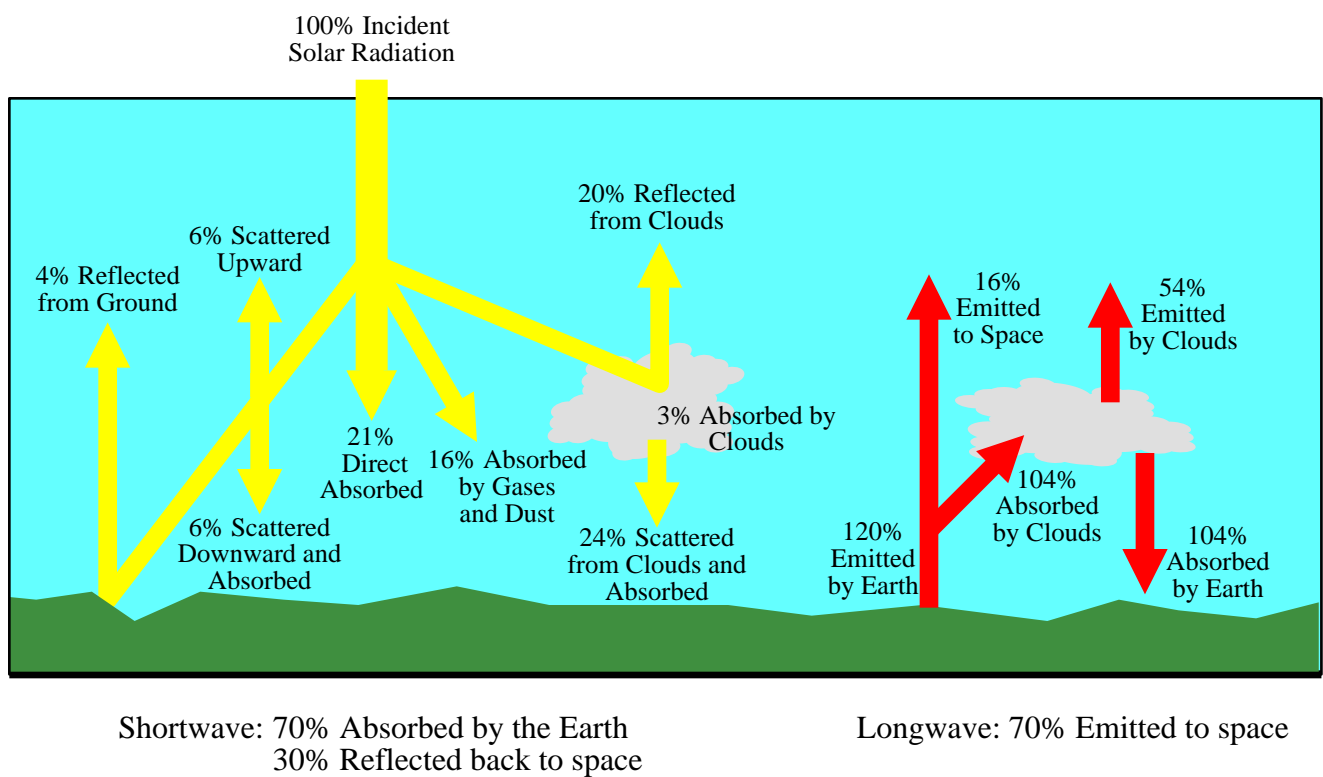


Figure 1.1 Schematic of the earth–atmosphere system showing the major components of the earth radiation budget.

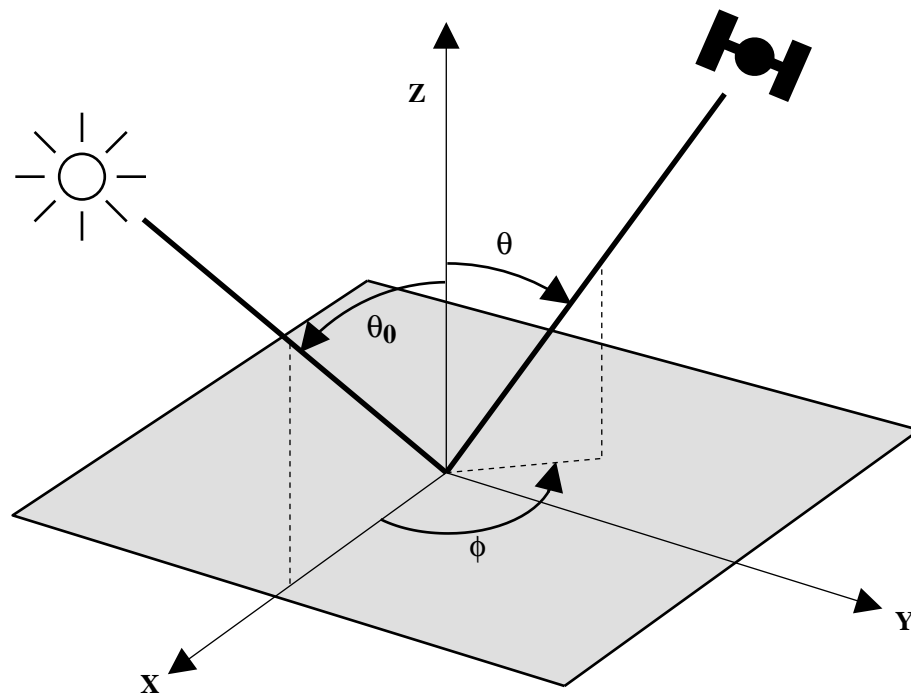


Figure 1.2 Spherical coordinate system defining position of observer relative to solar plane.

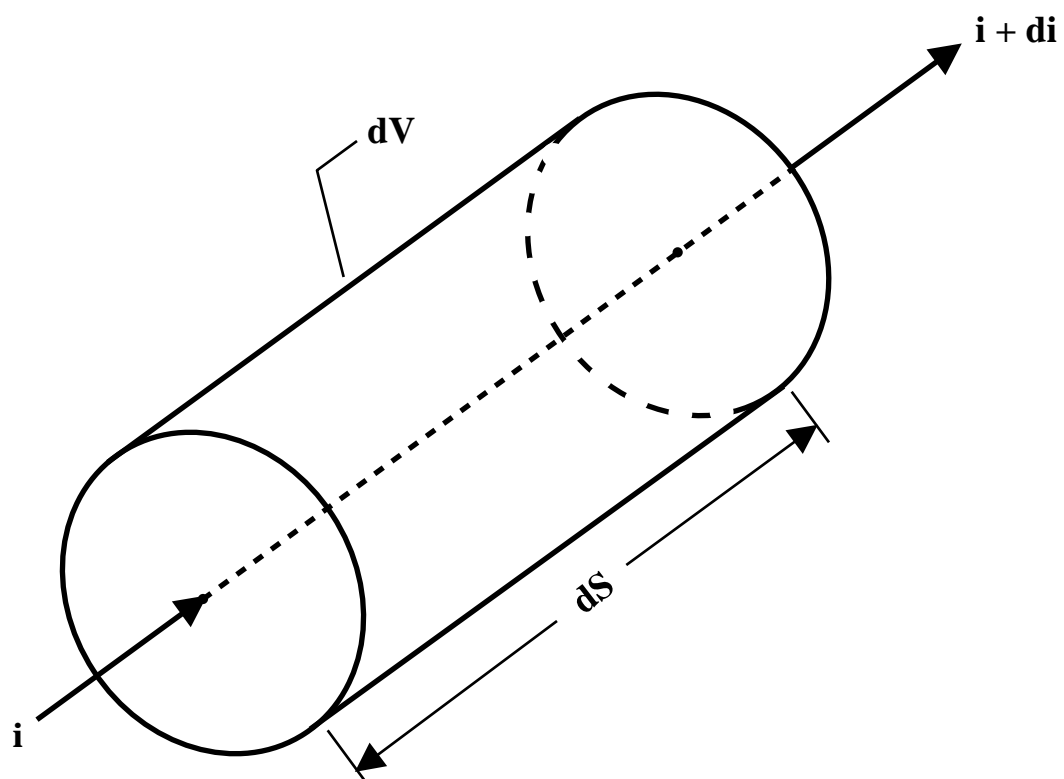


Figure 3.1 Intensity normally incident on an absorbing and scattering volume element of thickness dS .

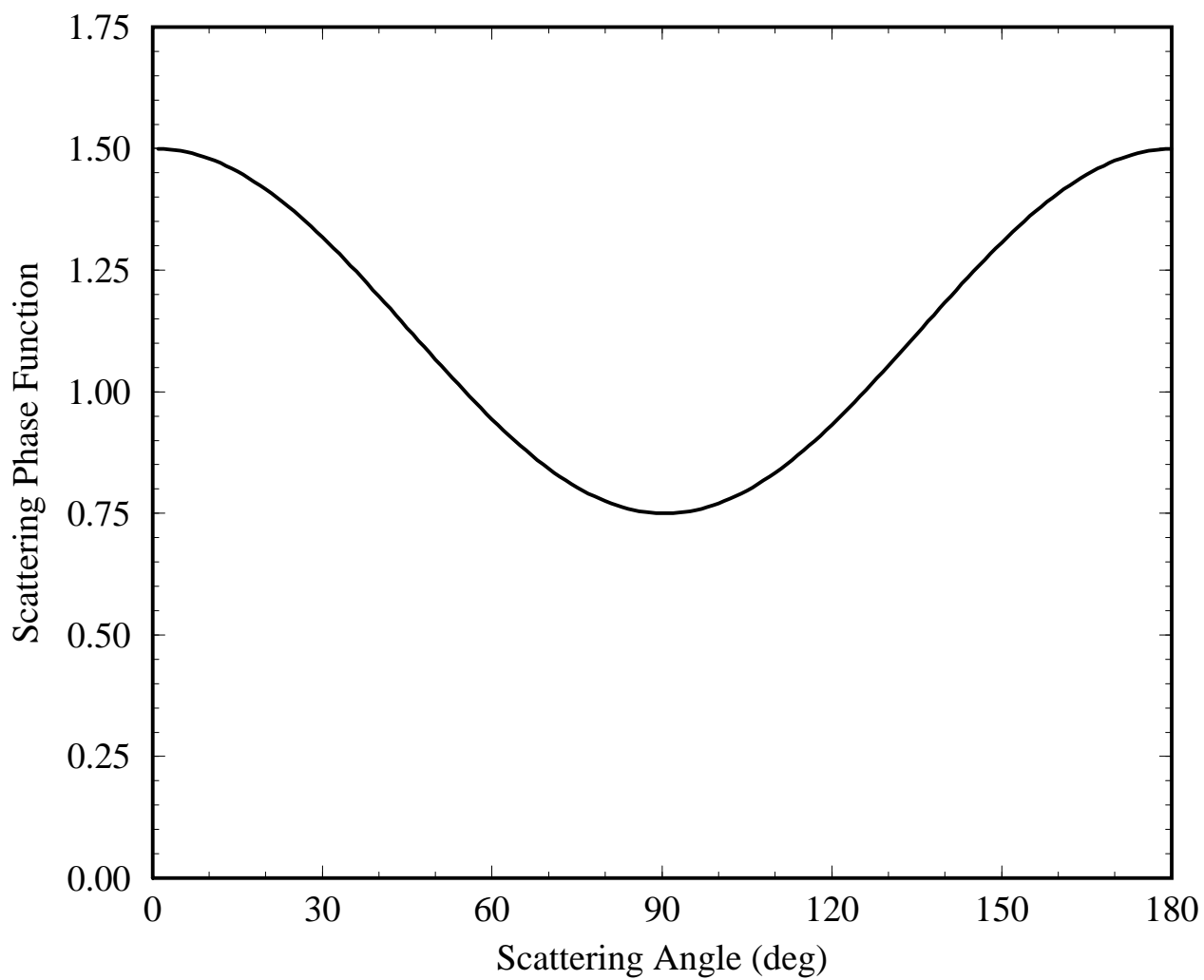


Figure 3.2 Rayleigh scattering phase function versus scattering angle.

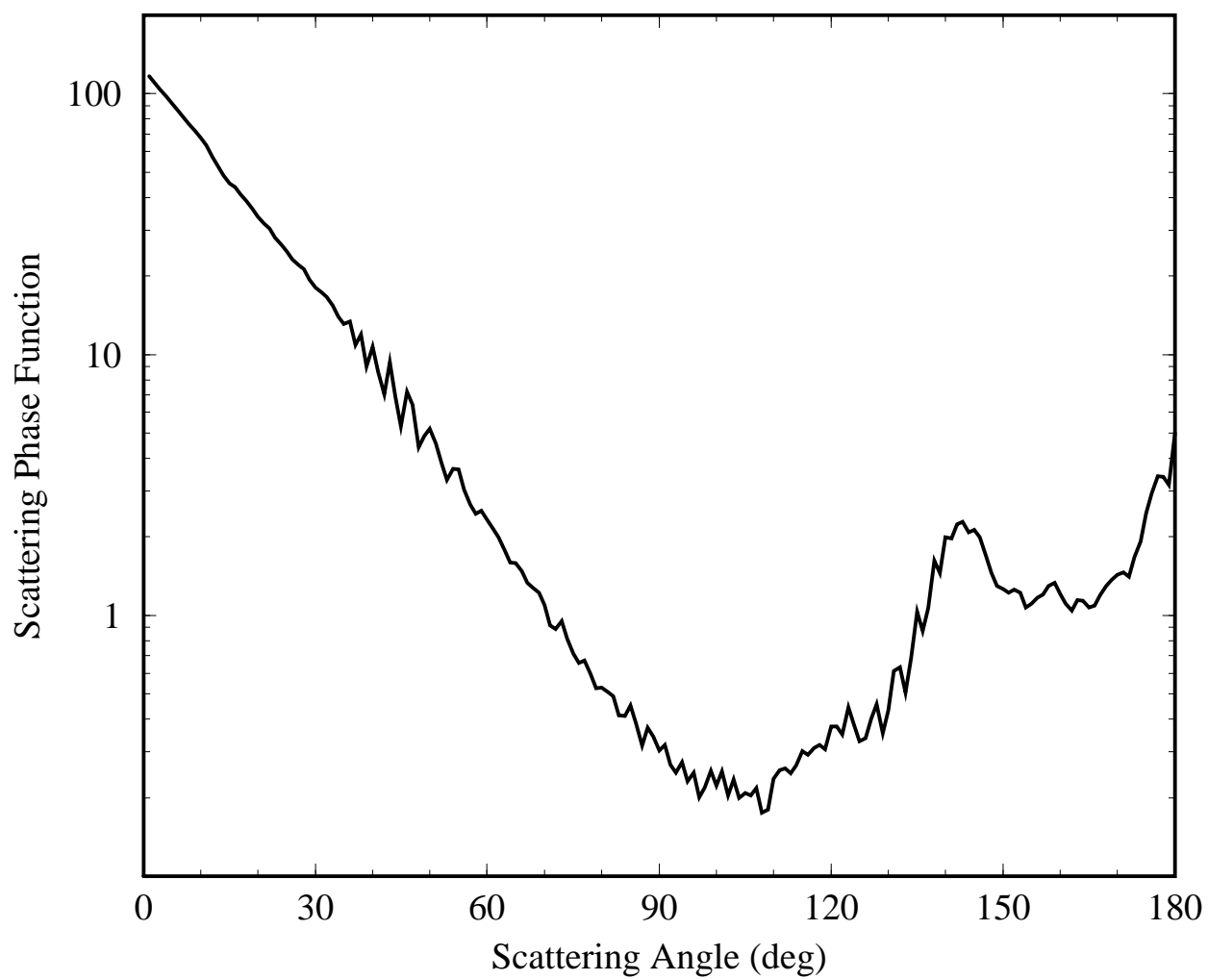


Figure 3.3 Mie scattering phase function versus scattering angle for typical marine cumulus cloud with water droplet size distribution parameters $r_{\text{eff}} = 5.56 \mu\text{m}$ and $v_{\text{eff}} = 0.111$ at $\lambda = 0.55 \mu\text{m}$.

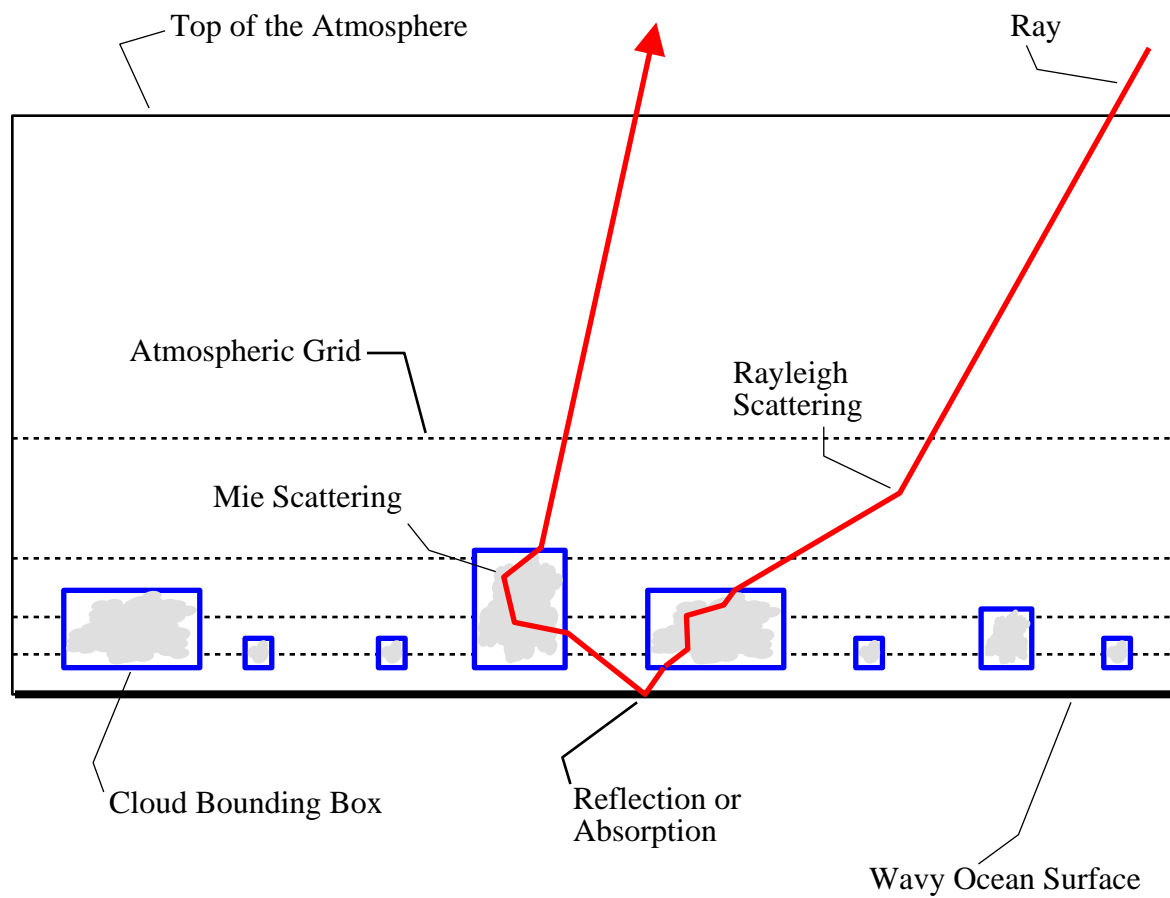


Figure 4.1. Monte-Carlo ray-trace model of the atmosphere including three-dimensional clouds, ocean surface, and atmospheric scattering.

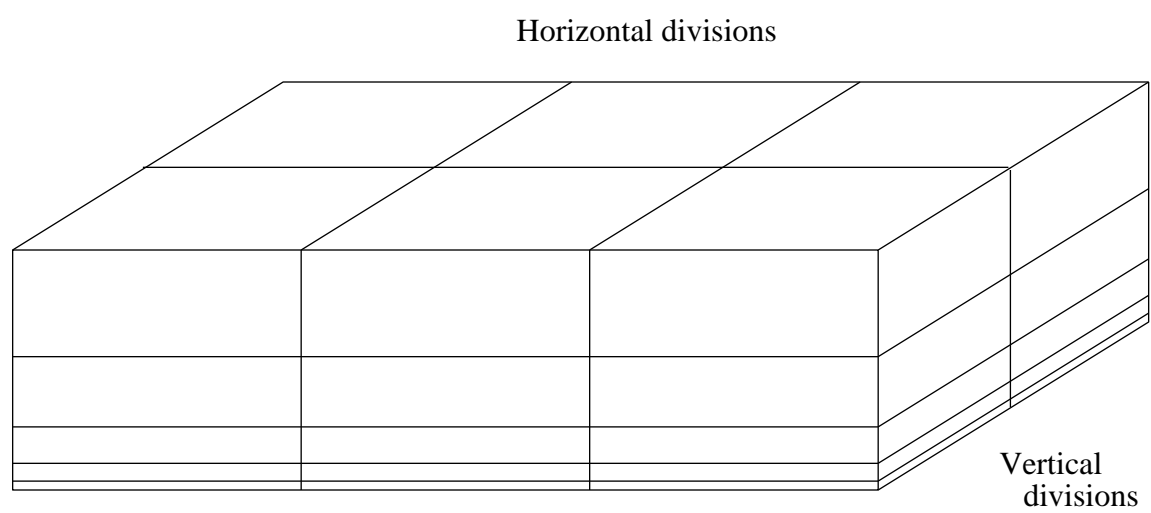


Figure 4.2. Three-dimensional atmospheric grid system.

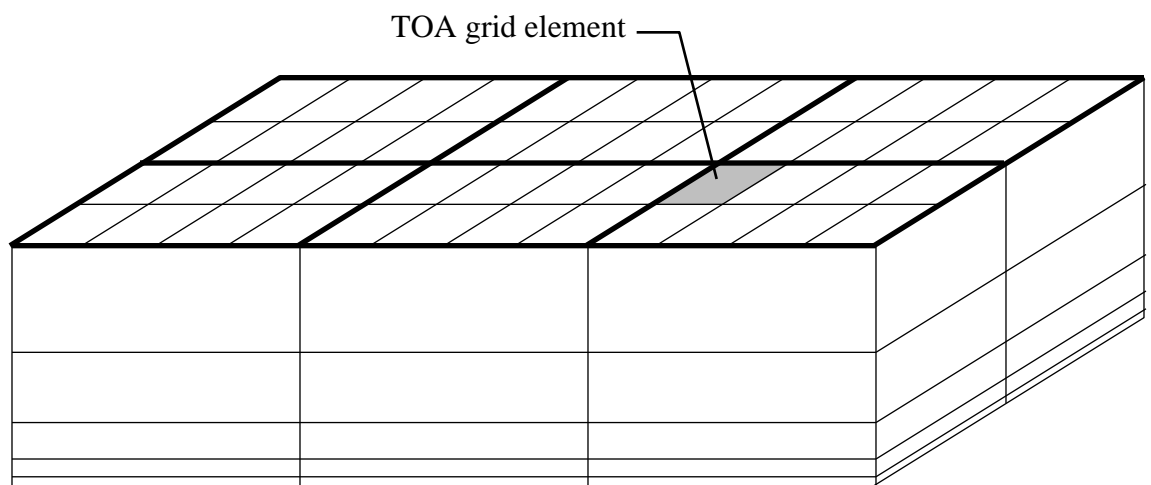


Figure 4.3. Top-of-the-atmosphere (TOA) two-dimensional spatial grid system.

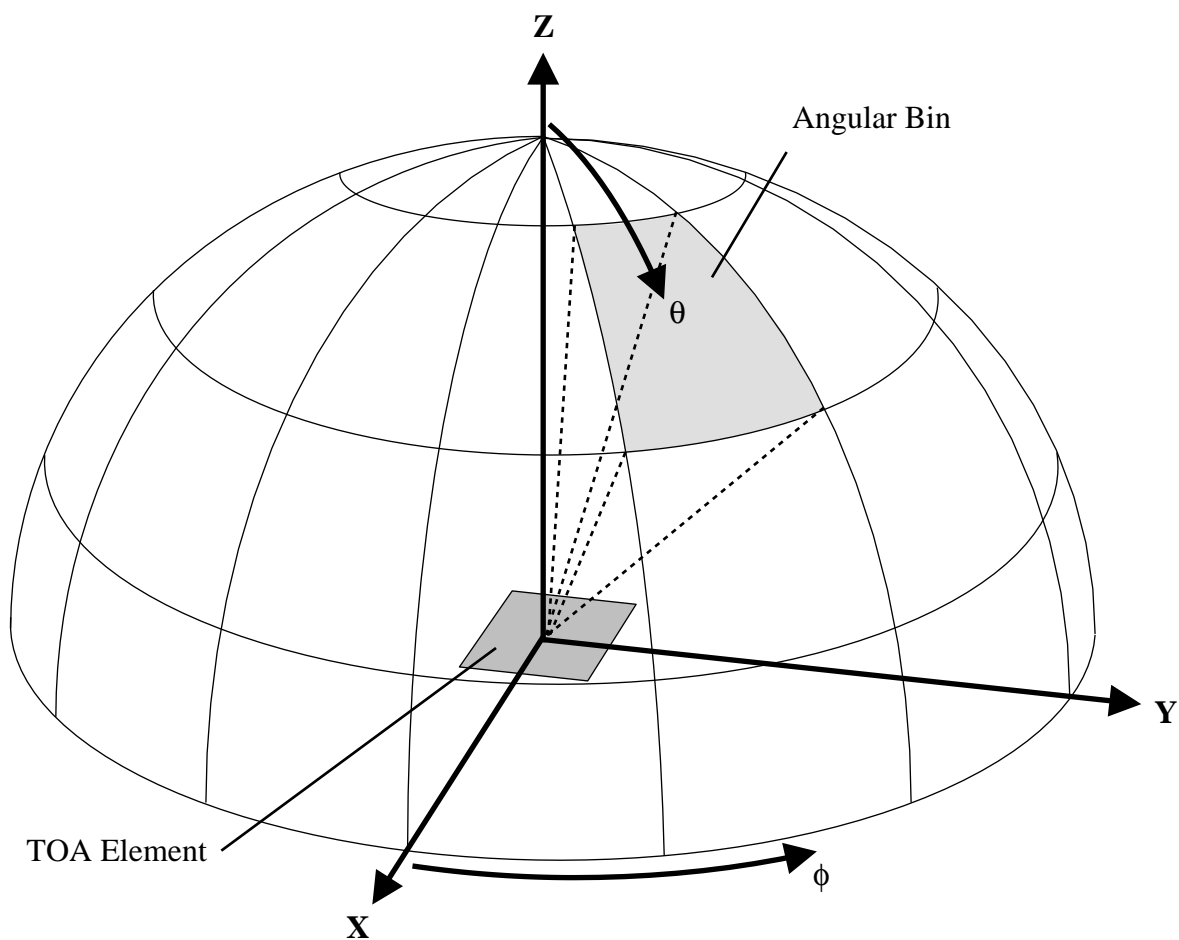


Figure 4.4 TOA angular grid system with divisions in zenith (θ) and azimuth (ϕ) angular directions.

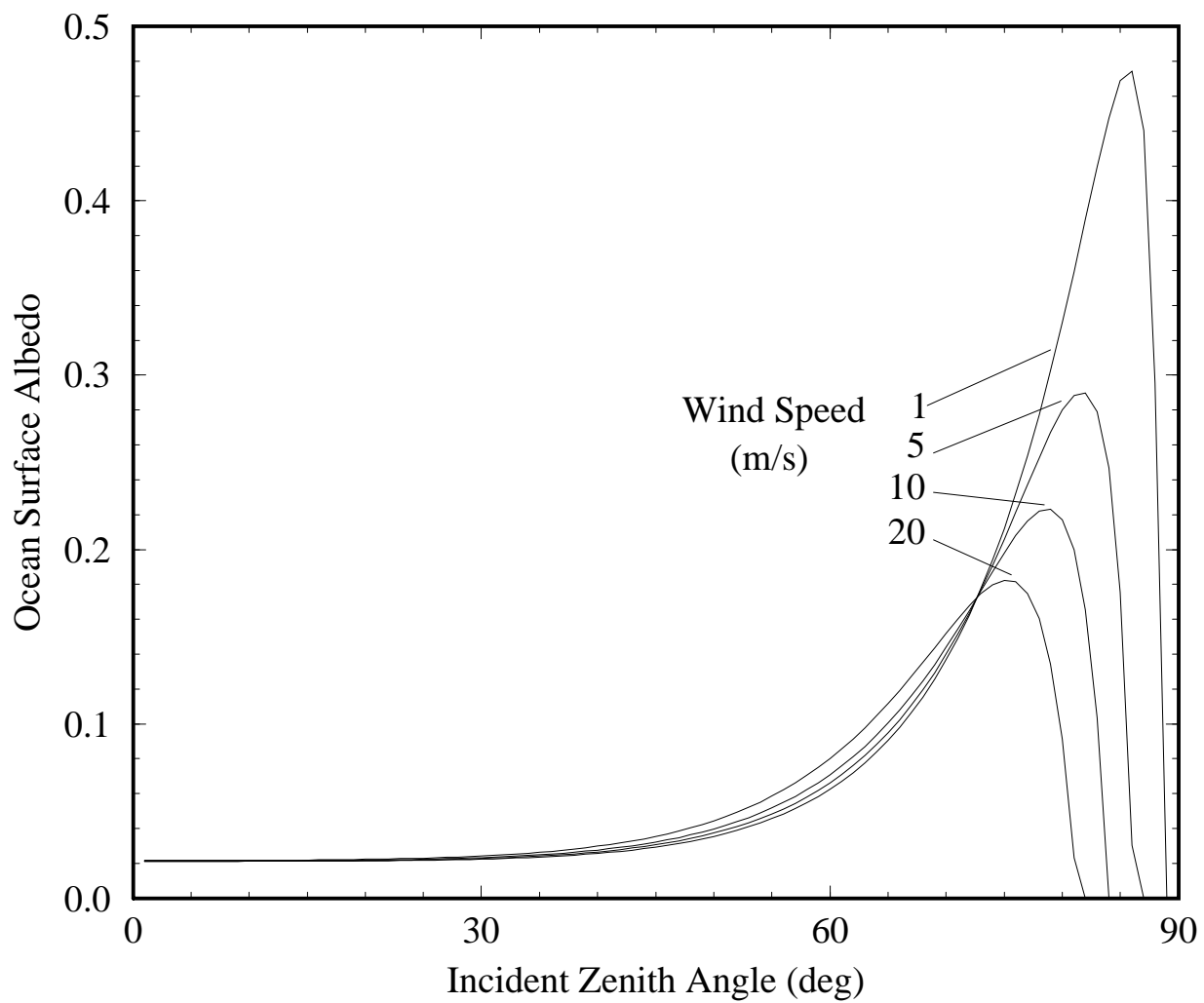


Figure 4.5 Ocean surface albedo as a function of incident zenith angle and wind speed according to Cox and Munk (1954a).

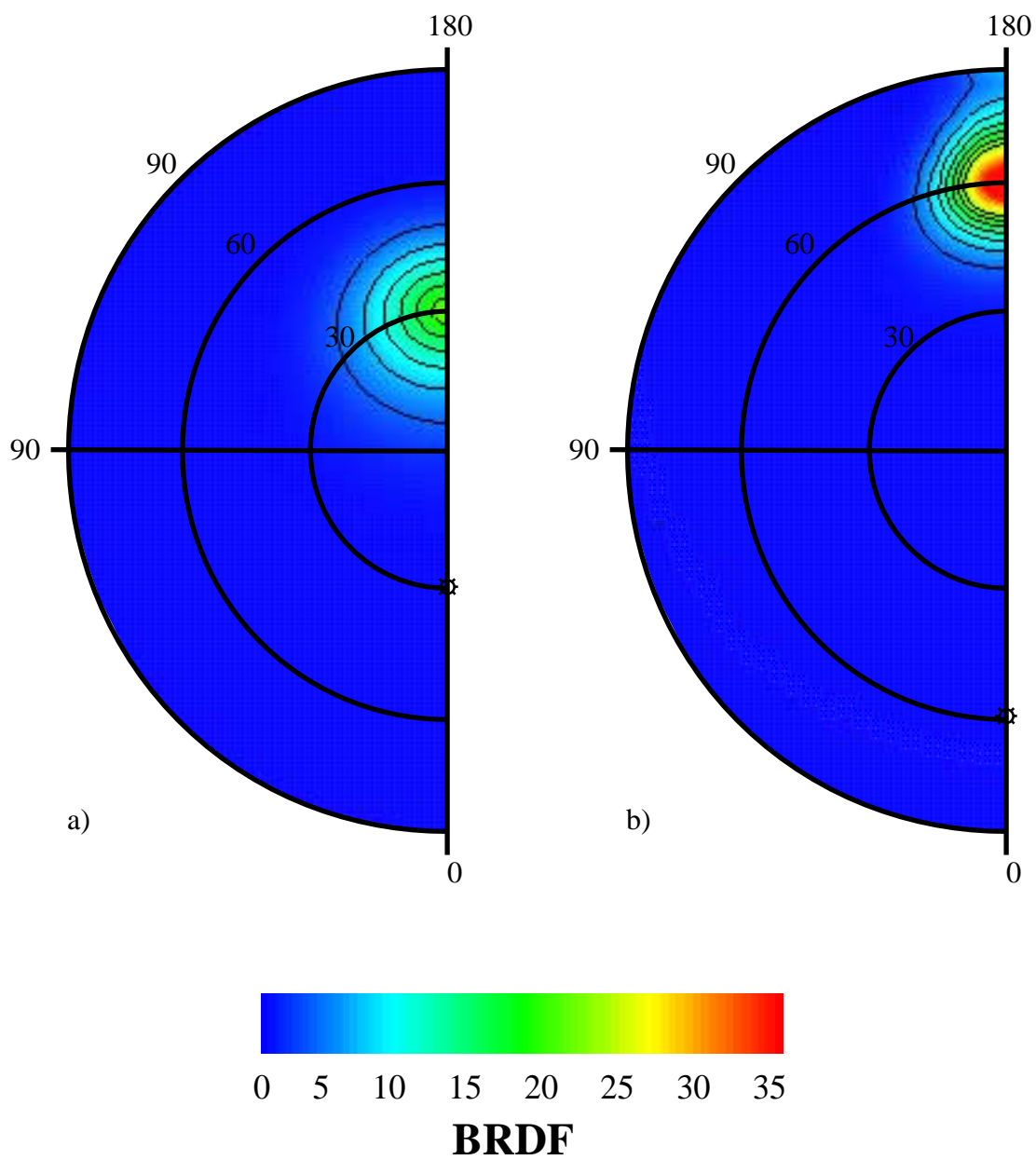


Figure 4.6 Ocean surface BRDF for wind speed of 5 m/s with solar zenith angles (a) 30 deg and (b) 60 deg.

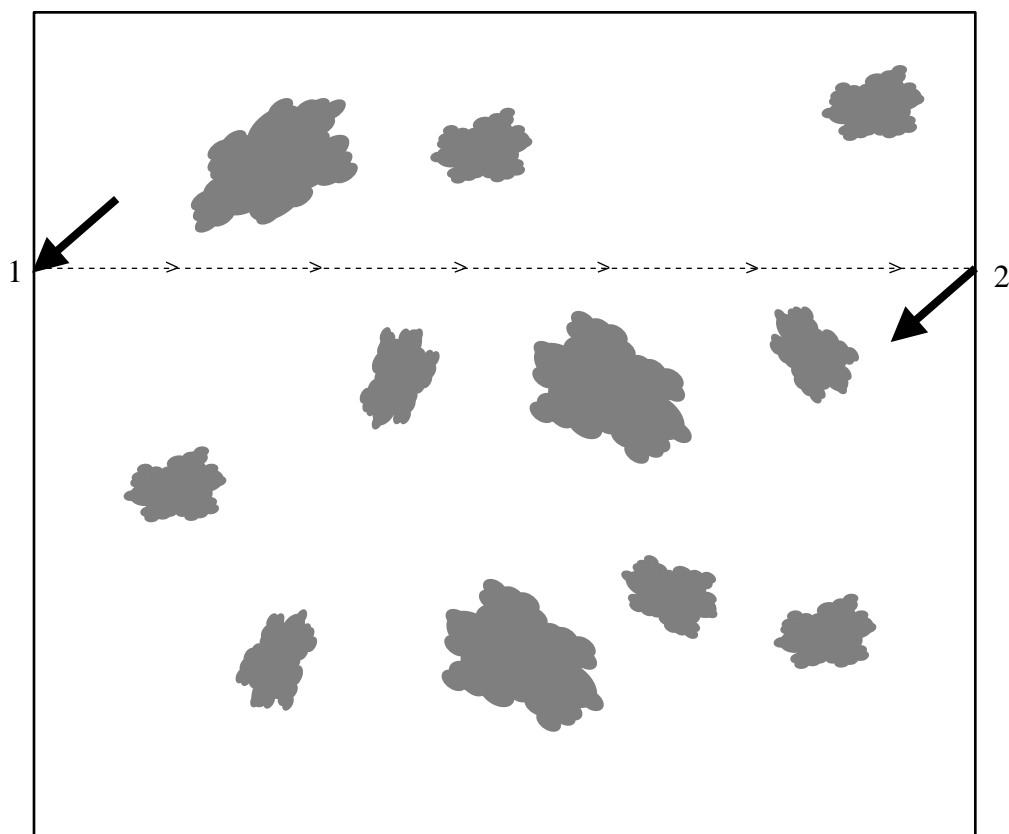


Figure 4.7 Example of cyclic boundary condition at side walls of atmosphere showing ray copied from point 1 to point 2 without change in direction.

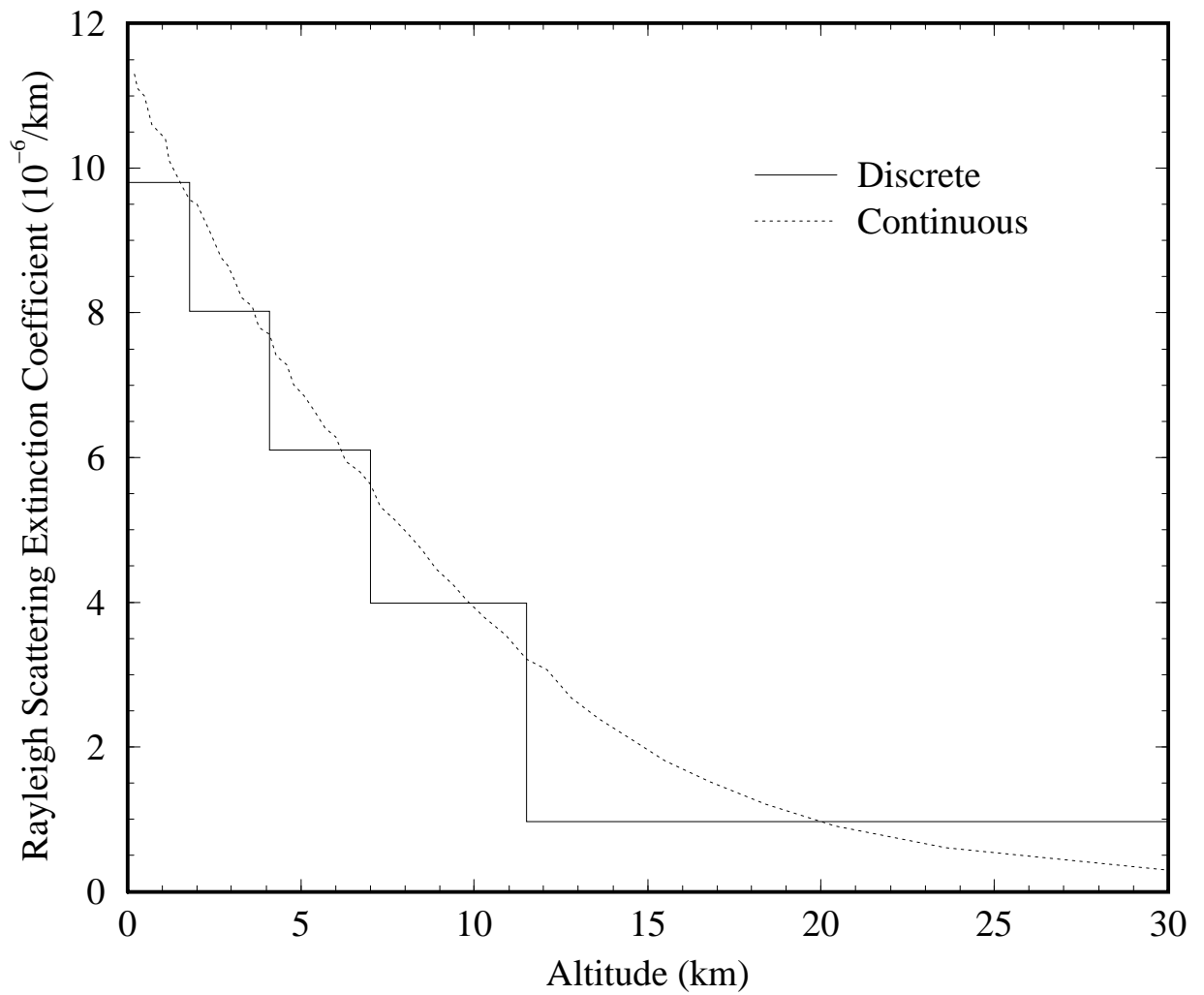


Figure 4.8 Rayleigh scattering coefficient versus altitude in the atmosphere.

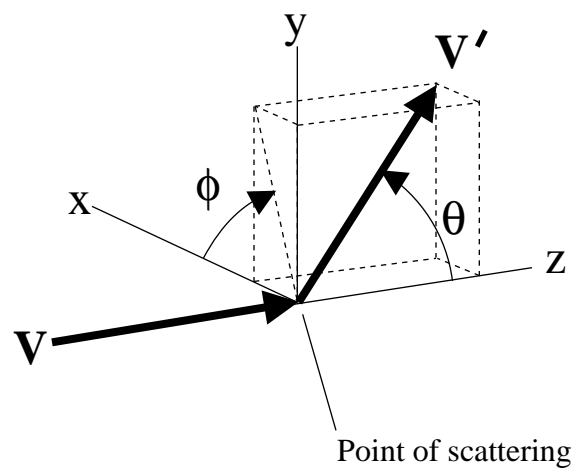


Figure 4.9. Single-scattering event local coordinate system defined by orientation of incoming vector.

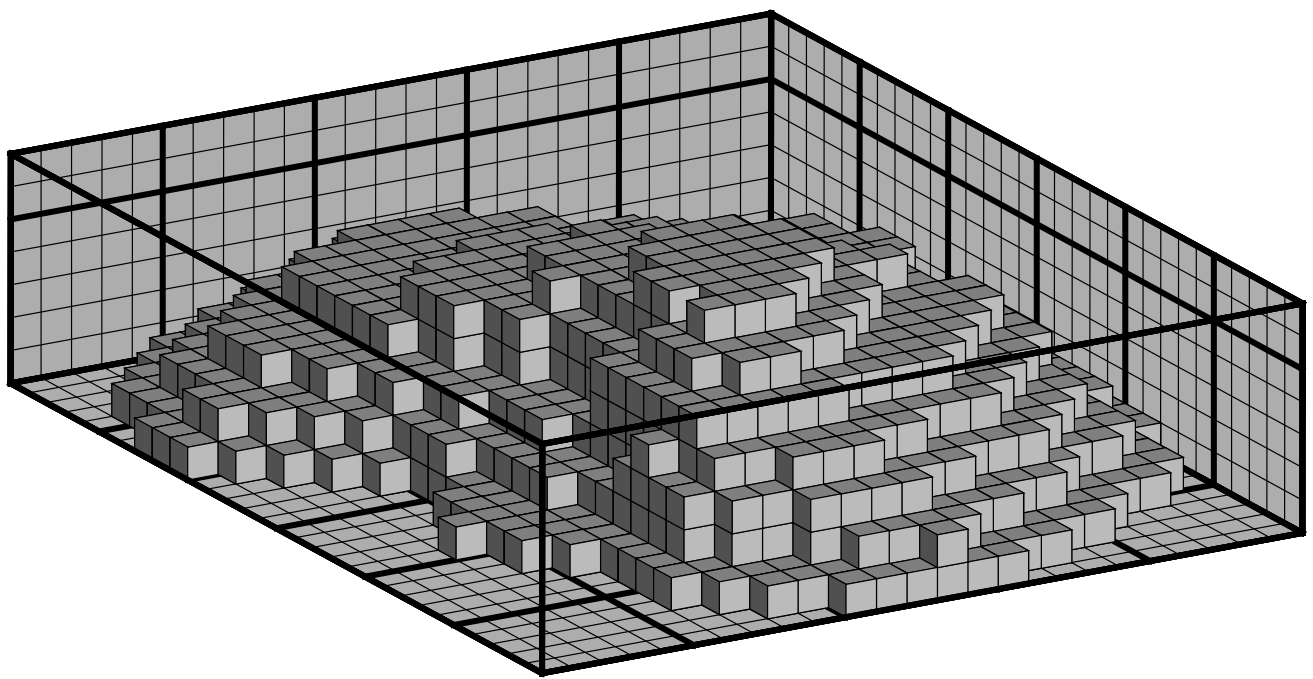


Figure 4.10 Typical three-dimensional cloud composed of a large number of identical cubic elements, or cloud building blocks.

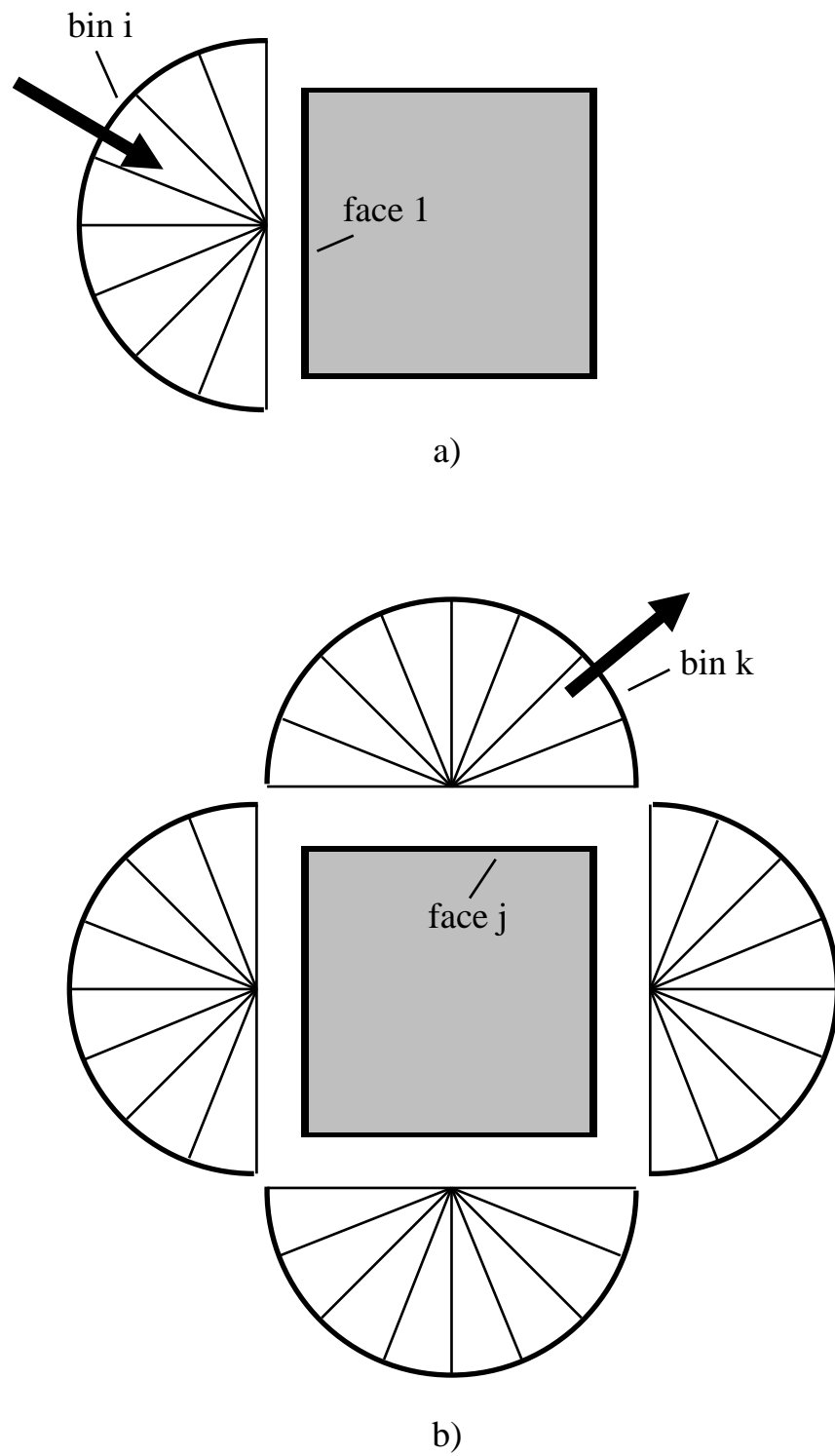
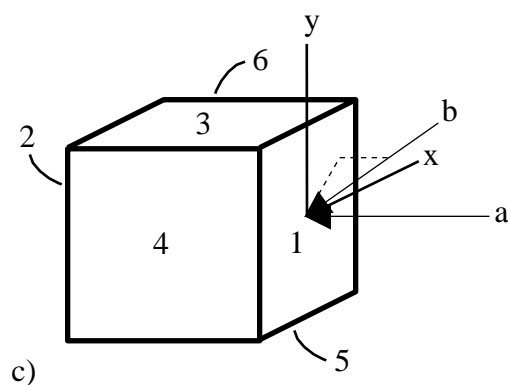
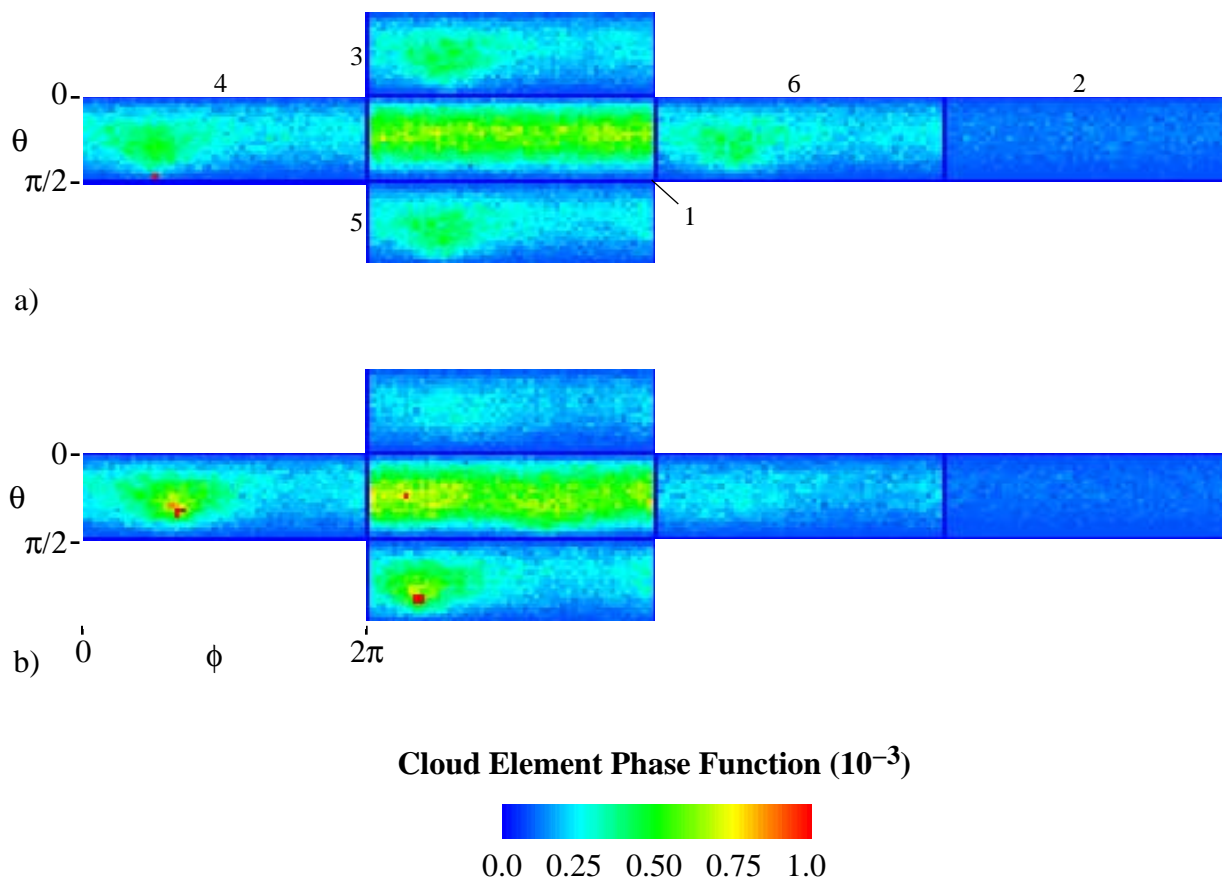


Figure 4.11. Two-dimensional representation of cloud element angular discretization showing (a) the incoming bins and the (b) outgoing bins.



Medium Optical Properties:
 Scattering: Mie
 Mean partical size: 5.56 μm
 Size variance: 0.111
 Wavelength: 0.55 μm
 Index of refraction: 1.333
 Element size: 100 m edges
 Element optical depth: 8.6

Figure 4.12. Cloud element multiple-scattering phase function showing the proportion of energy leaving the six faces for two different incident angles (a) and (b) corresponding to the similarly labelled vectors in (c).

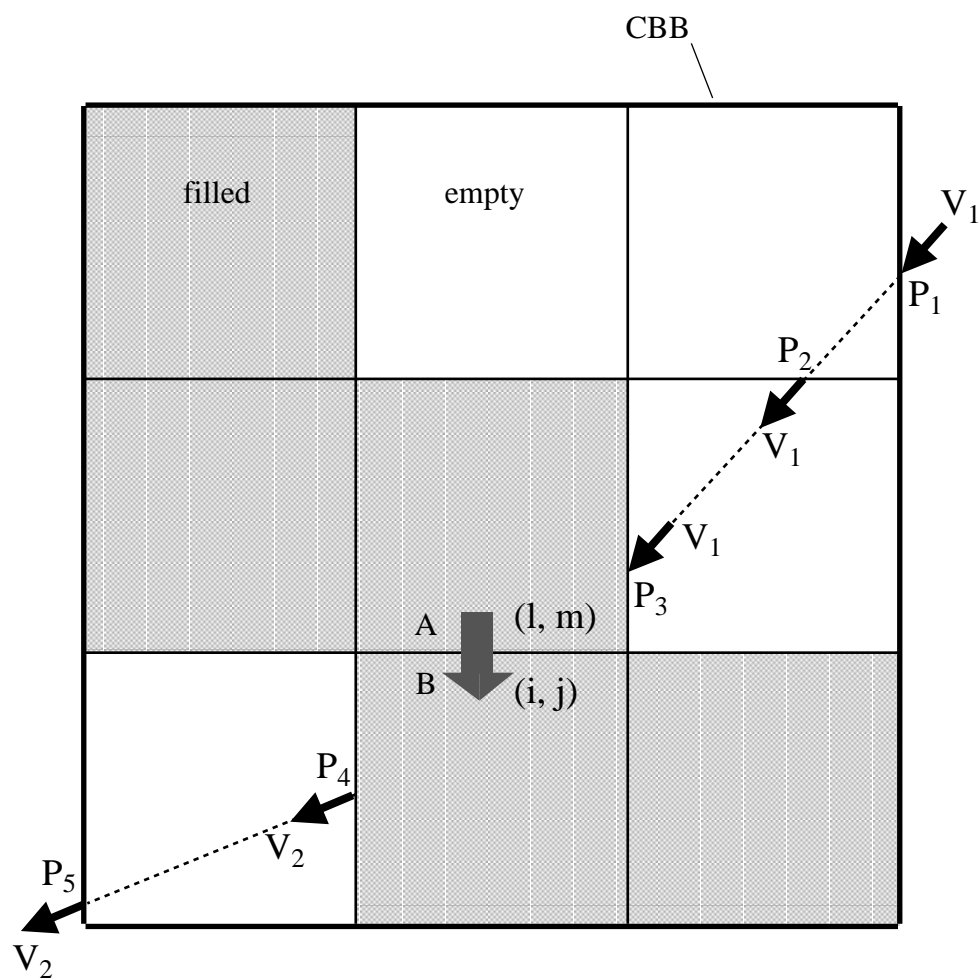


Figure 4.13. A typical ray trace through filled and empty cloud elements.

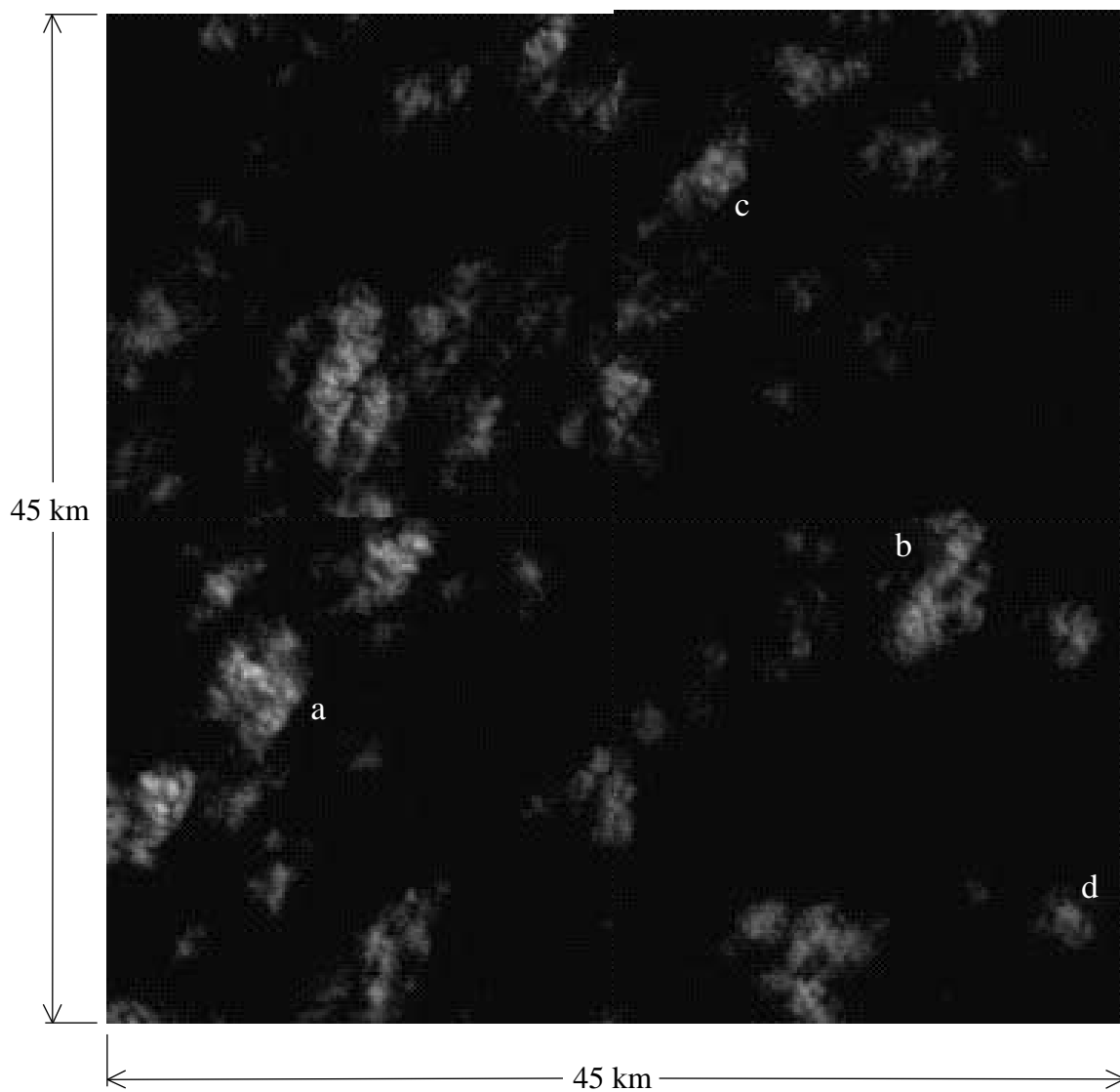
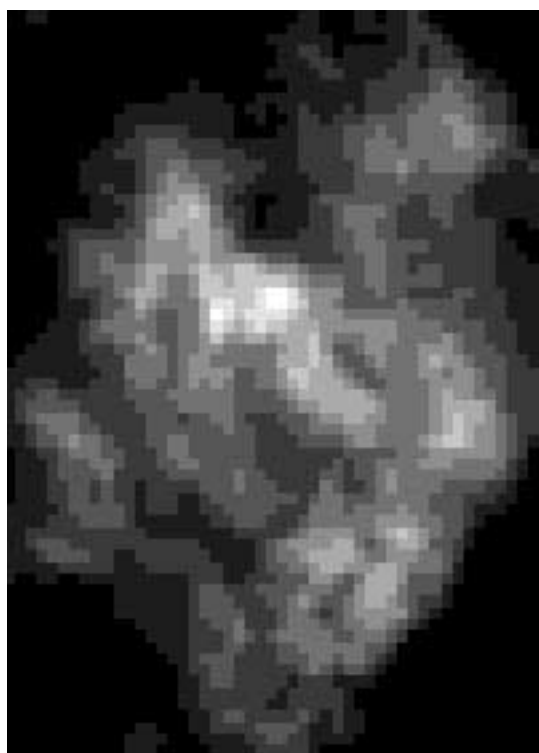
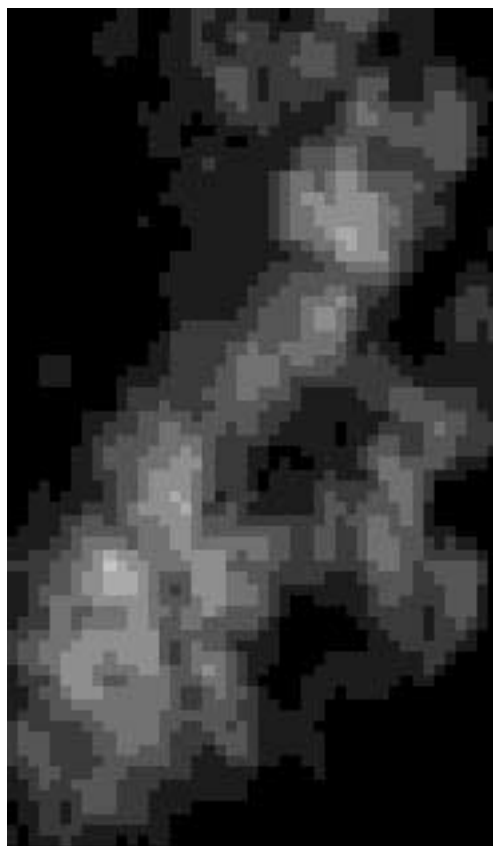


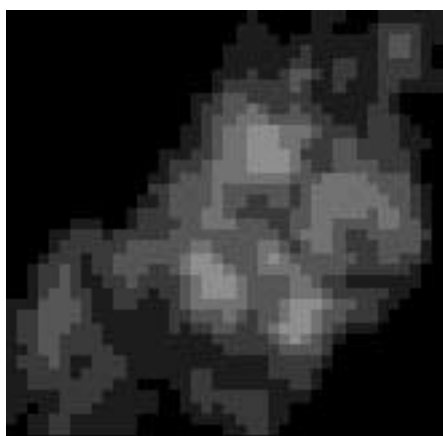
Figure 4.14. Typical Landsat data showing cloud optical thickness..



a)



b)



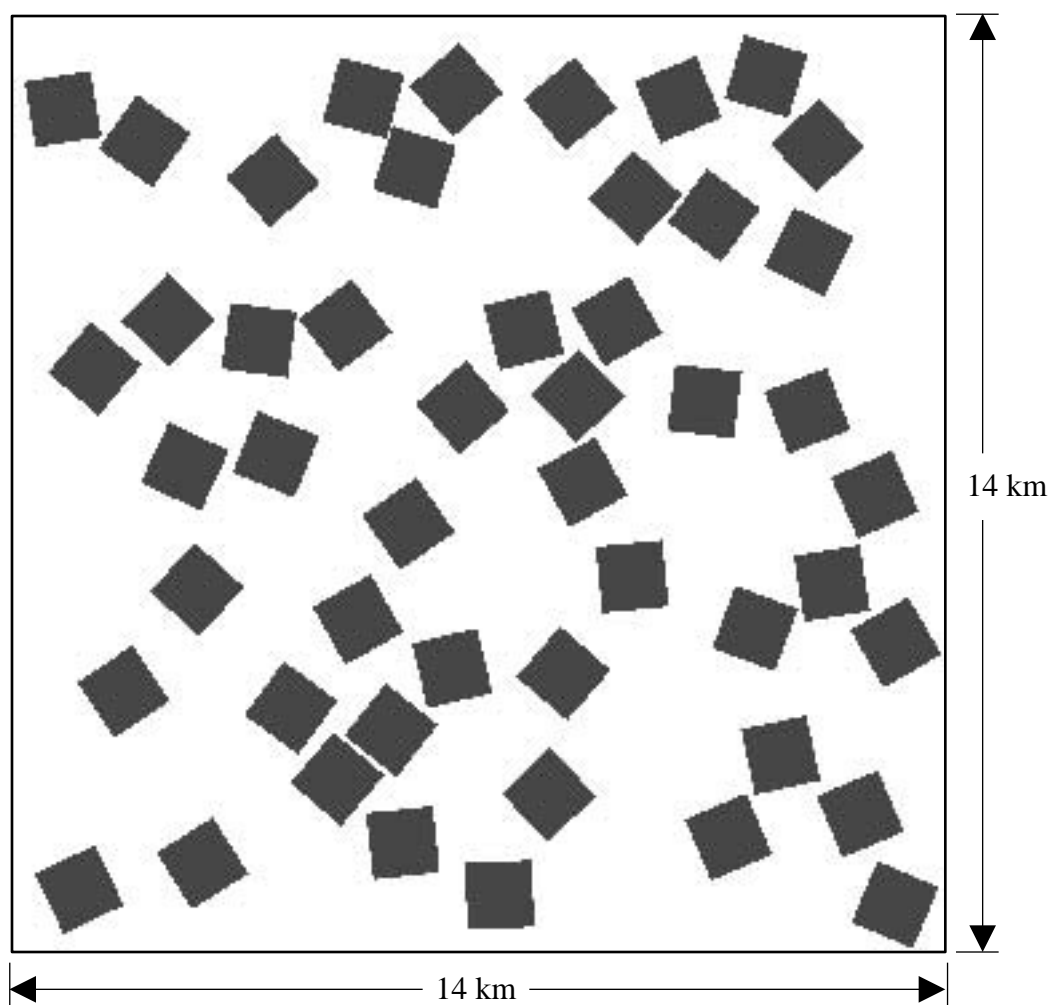
c)



d)

5 km

Figure 4.15. Example of four clouds extracted from the Landsat image data of Figure 4.14.



Individual three-dimensional cloud
(1 x 1 x 2 km)

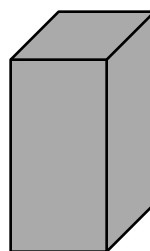


Figure 4.16 Cloud field used for TOA flux, BRDF symmetry, and cloud element size convergence studies.

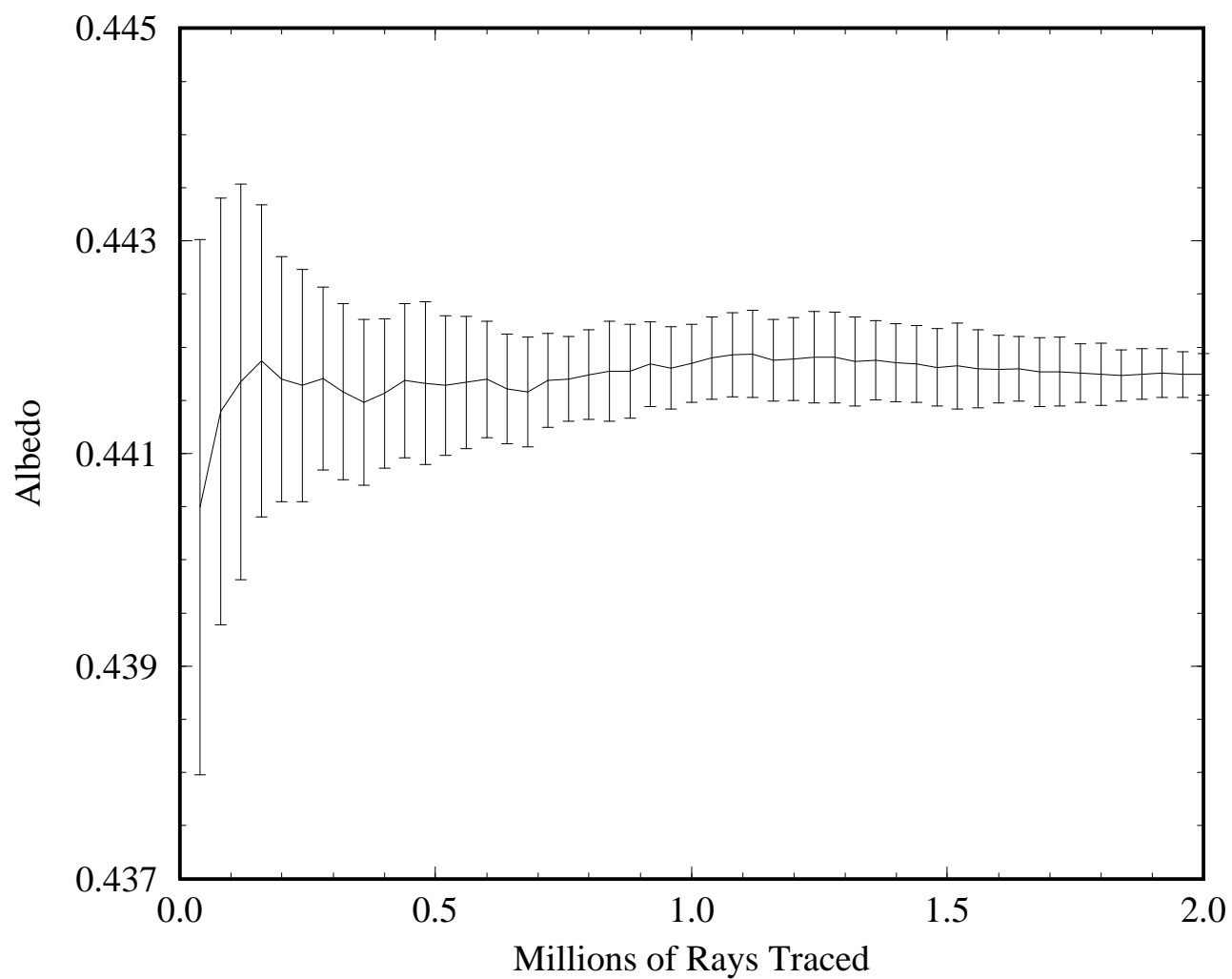


Figure 4.17 Albedo convergence as a function of the number of rays traced for ten separate sets of random number generator seeds. The vertical bars represent one standard deviation among each set of ten data points. Note the truncated vertical scale.

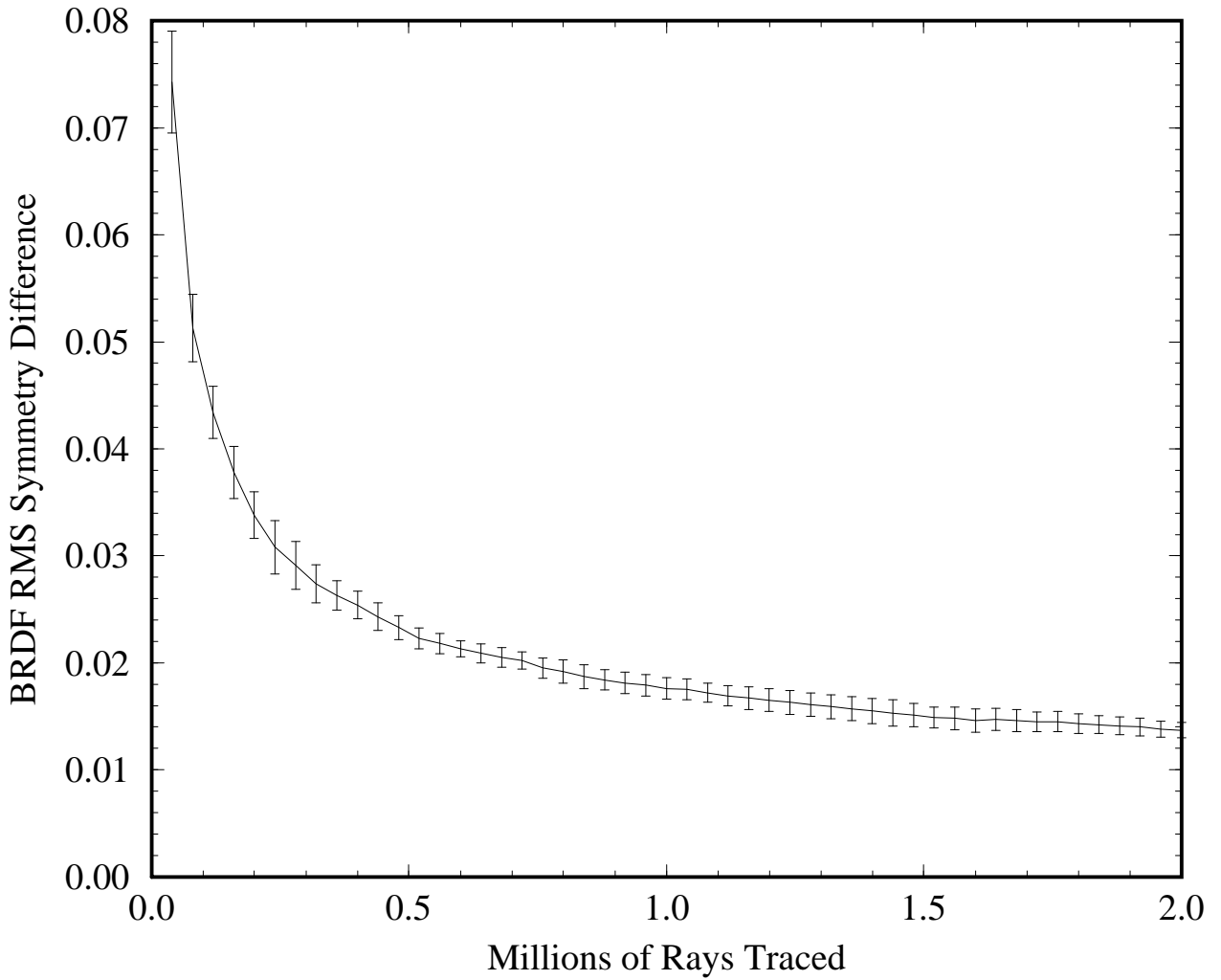


Figure 4.18 BRDF convergence as a function of the number of rays traced for ten separate sets of random number generator seeds. The vertical bars represent one standard deviation among each set of ten data points.

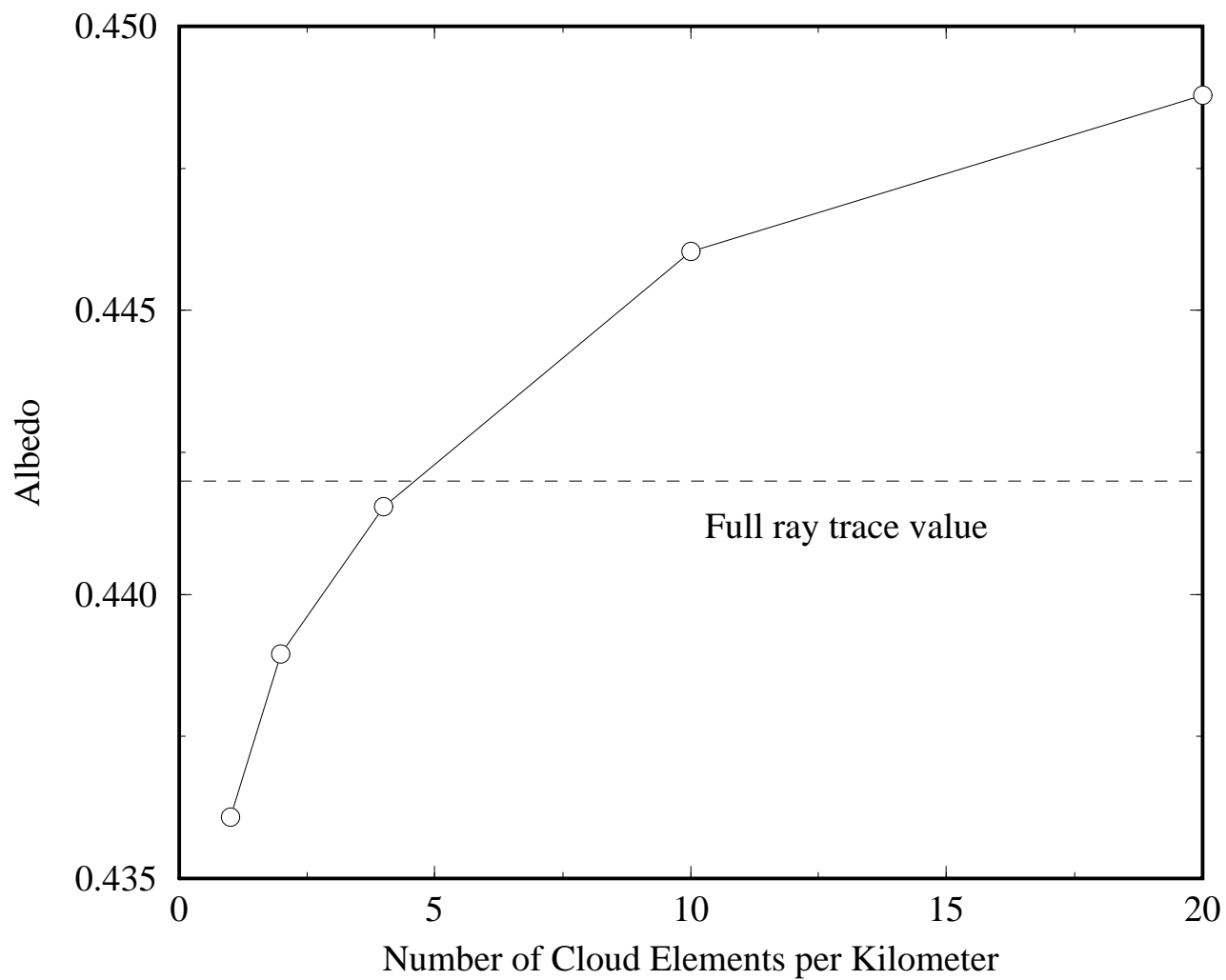


Figure 4.19 Convergence of the scene albedo as the cloud element size is refined. Note the truncated vertical scale.

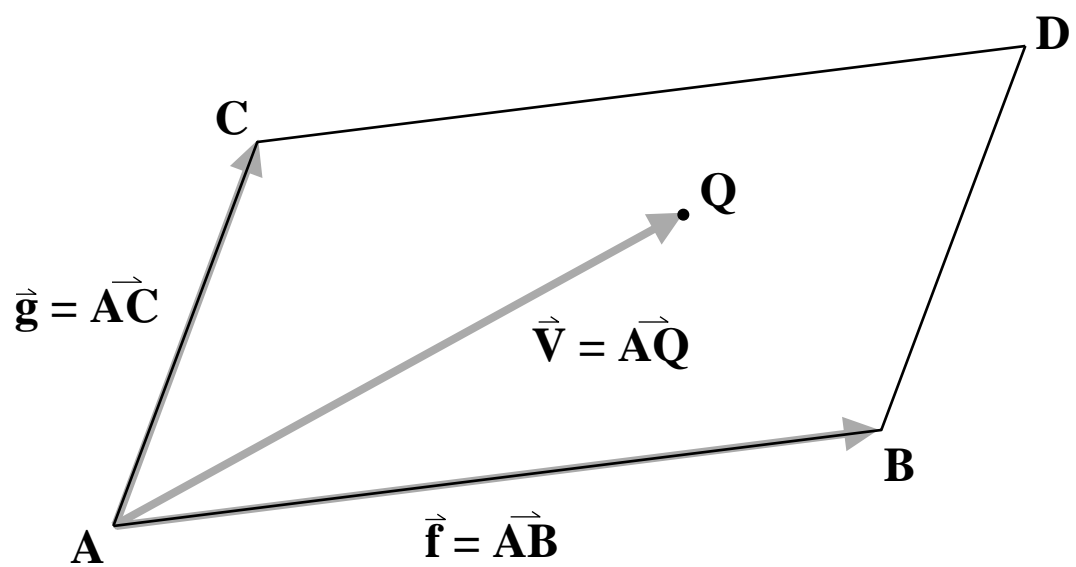


Figure 5.1 Basis–vector definition for determining whether or not a point exists within the boundaries of a finite surface.

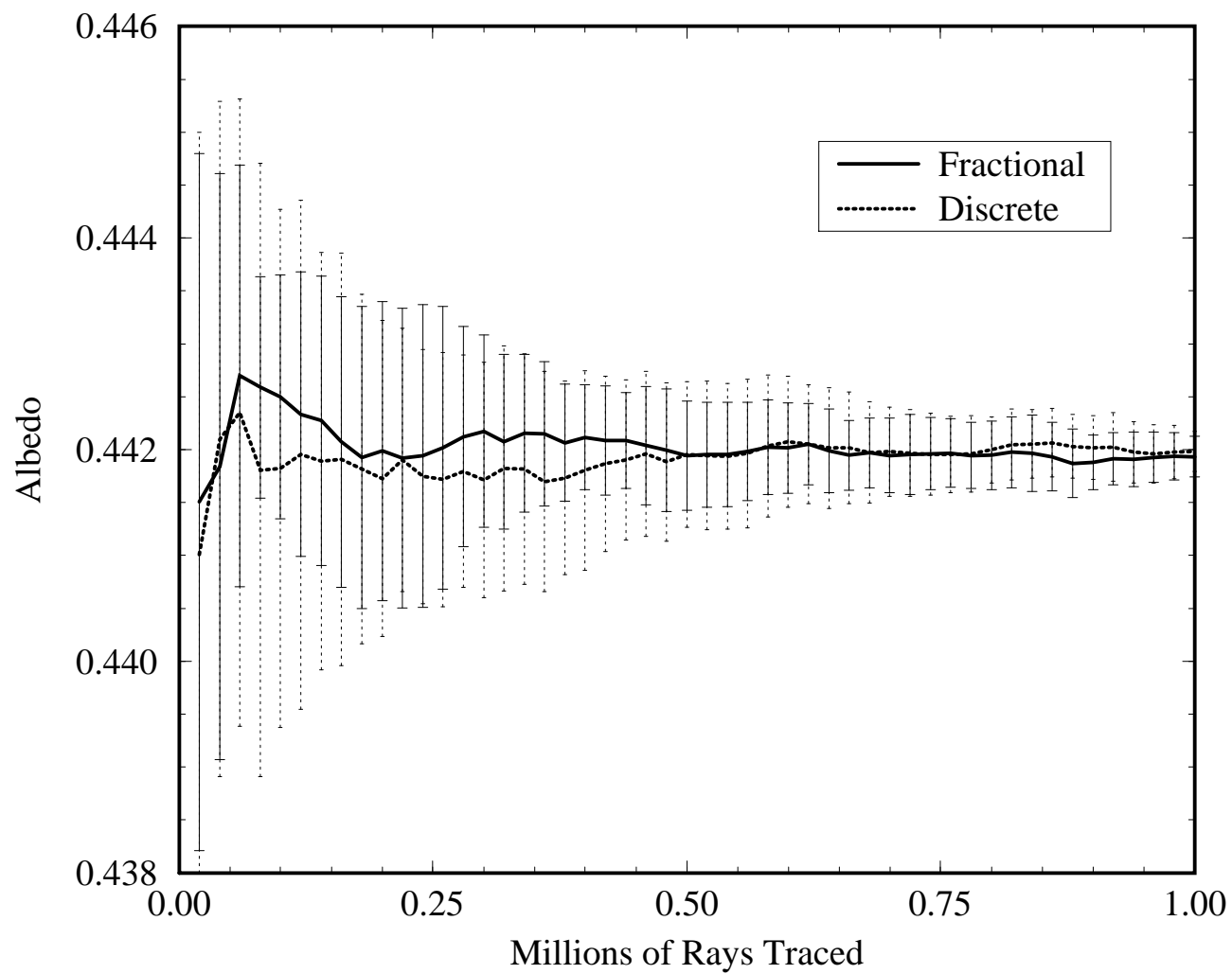


Figure 5.2 Convergence comparison between discrete ray absorption and fractional ray absorption.

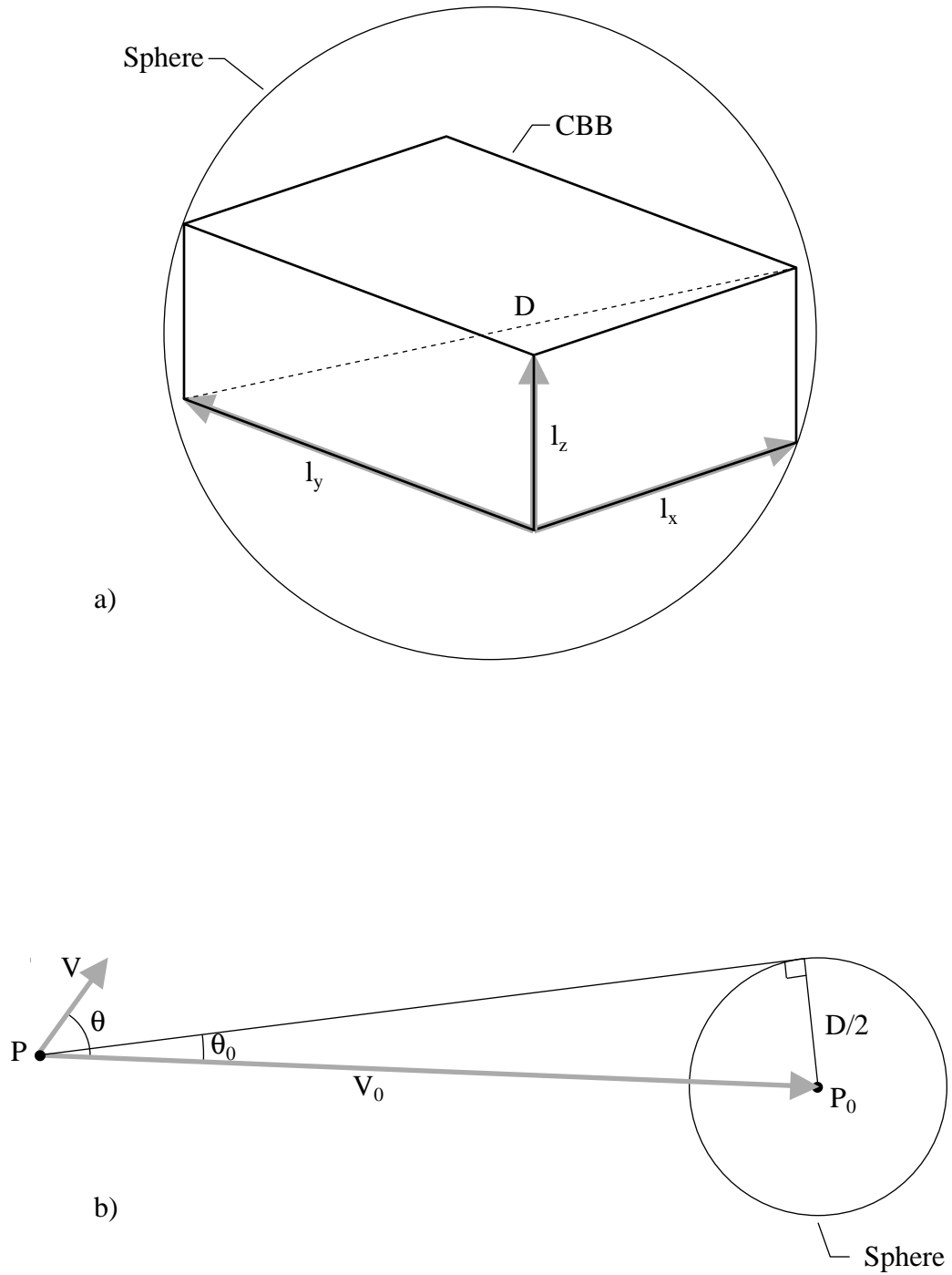


Figure 5.3 Definition of (a) the sphere around CBB and (b) the vector geometry for cloud-ray intersection acceleration technique.

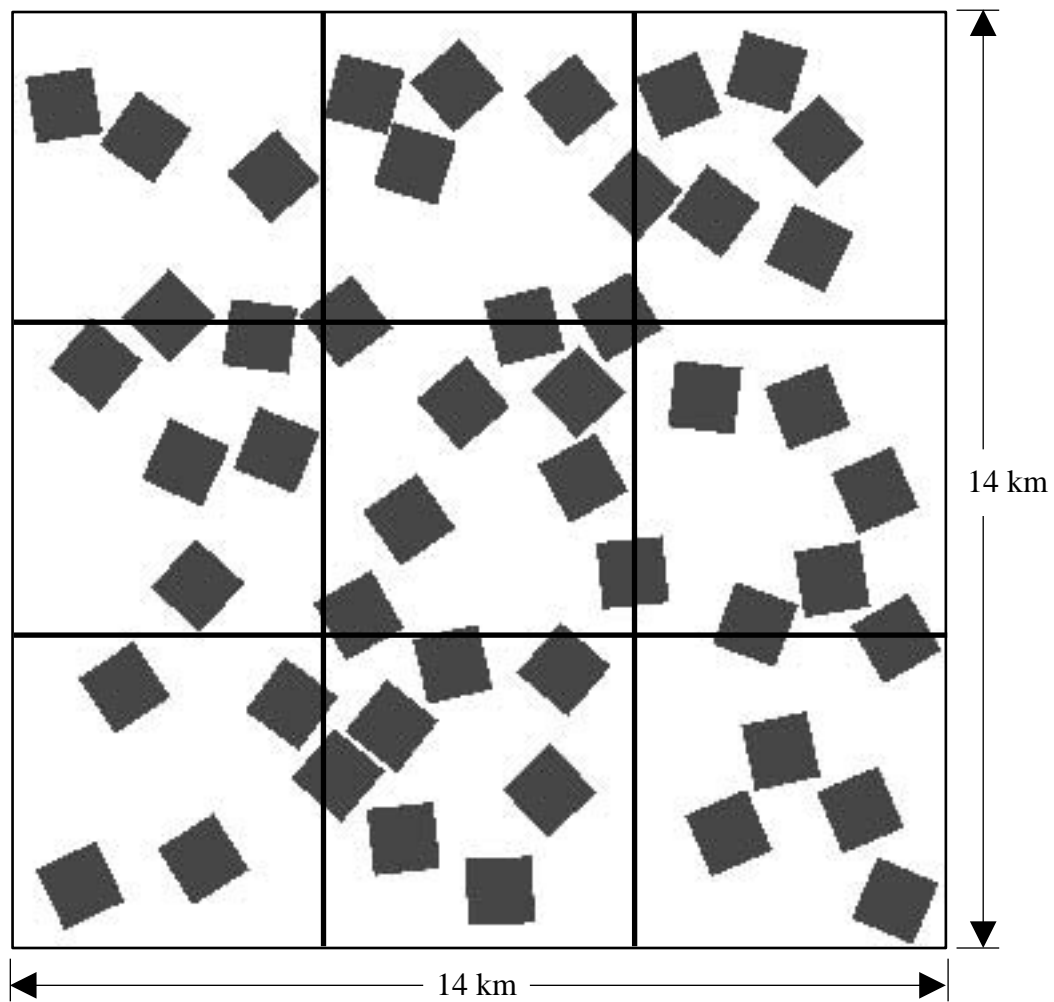


Figure 5.4 Atmospheric 3 by 3 grid system superimposed on the cloud field of Figure 4.16 for study of cloud placement acceleration method.

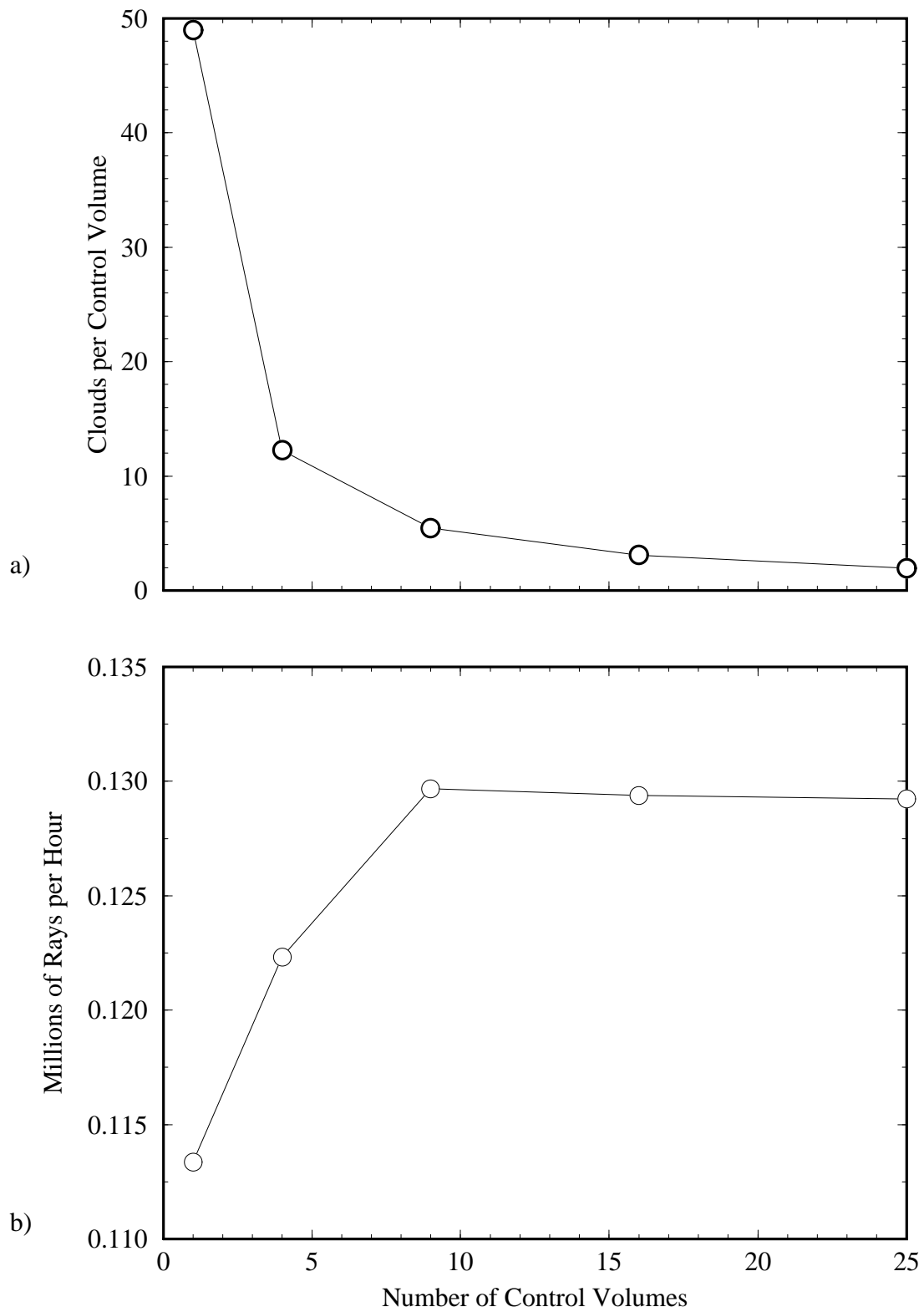


Figure 5.5 Illustration of (a) the number of clouds per atmospheric control volume and (b) the corresponding model performance.

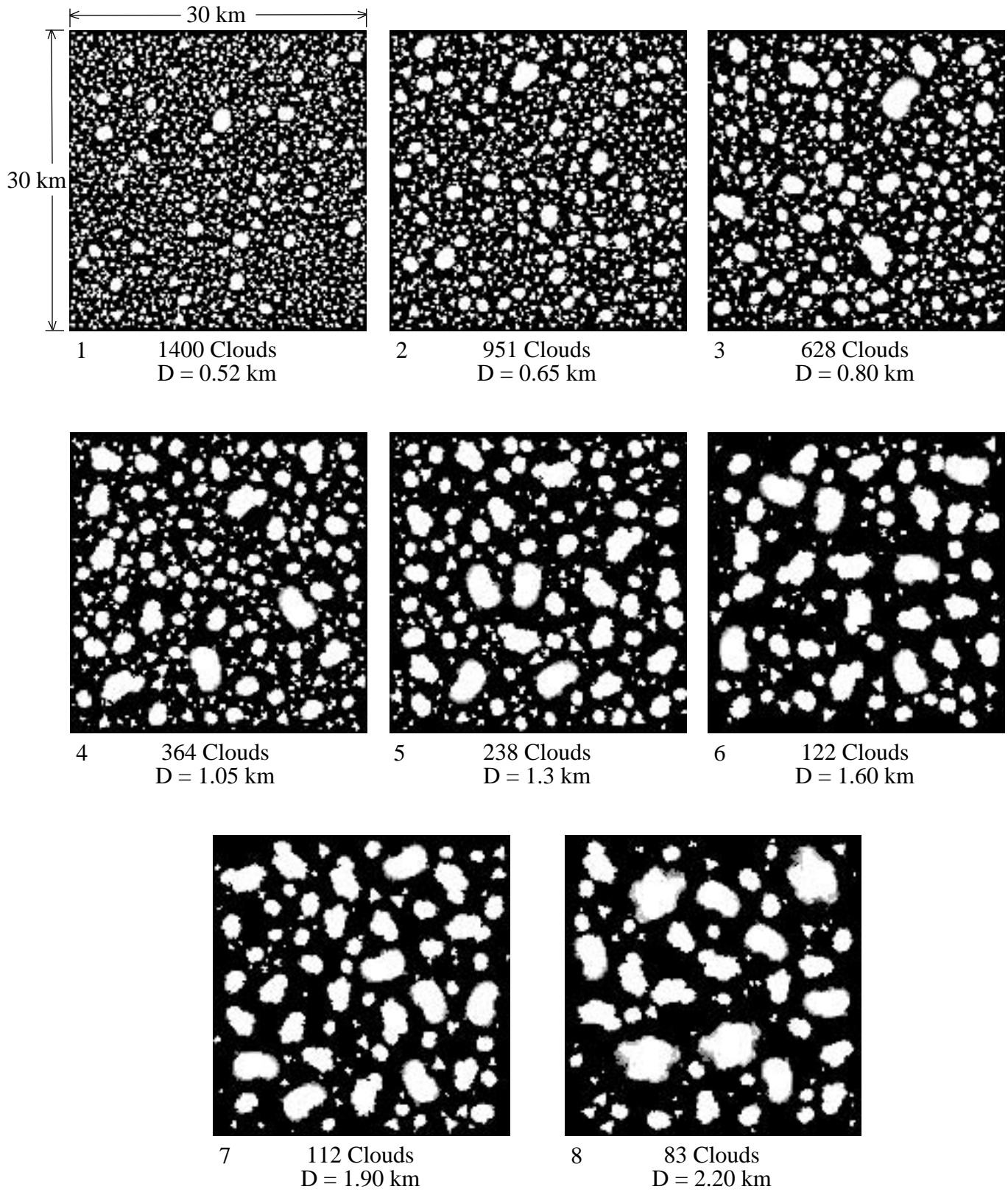


Figure 6.1 The eight scenes used in the cloud size sensitivity study with 35 percent cloud cover and 45 deg solar zenith angle.

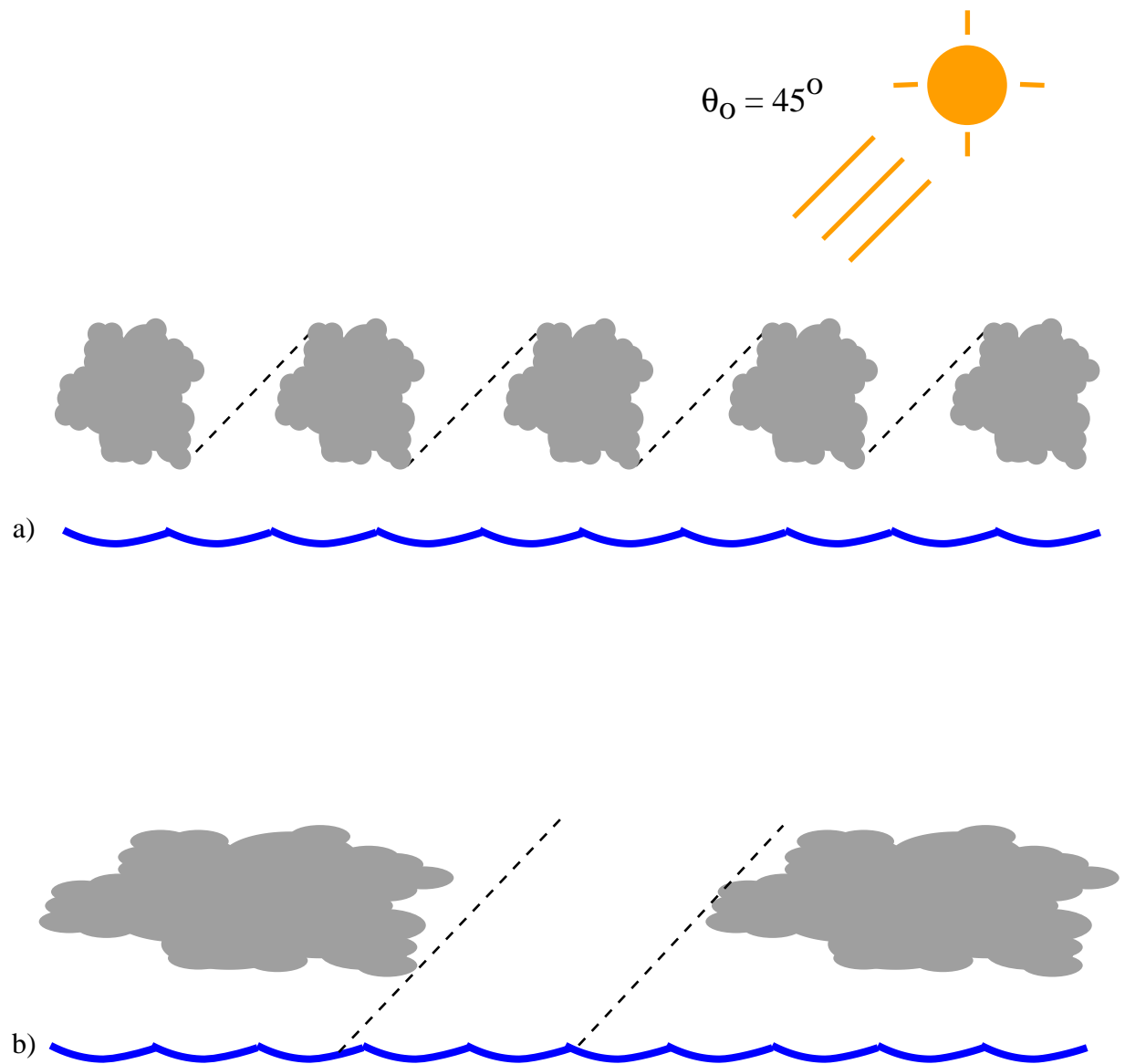


Figure 6.2 An example of the extremes in cloud size variation with (a) maximum and (b) minimum cloud-to-cloud interaction.

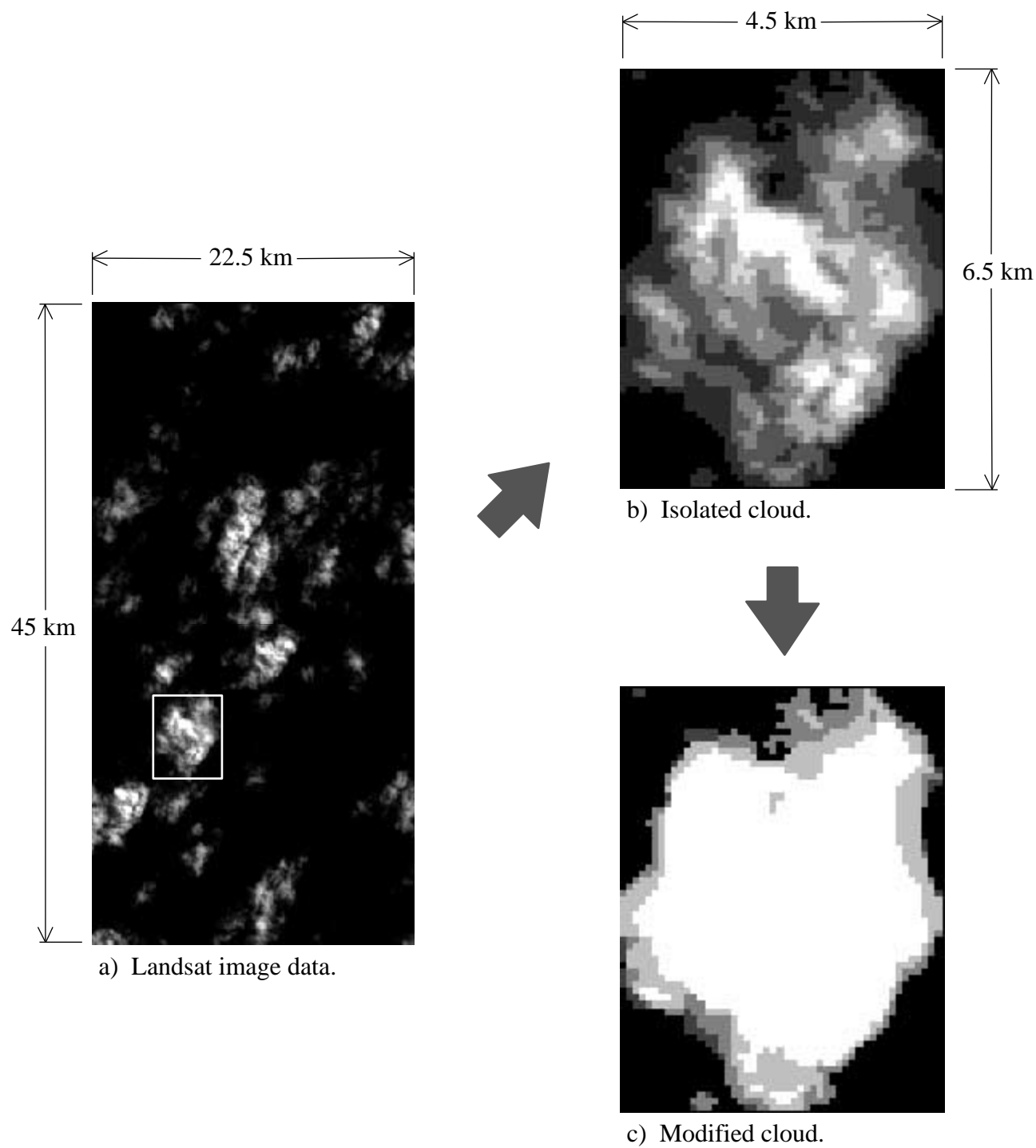


Figure 6.3 Extraction of cloud morphology from Landsat imagery and simplification to eliminate horizontal variations of vertical thickness.

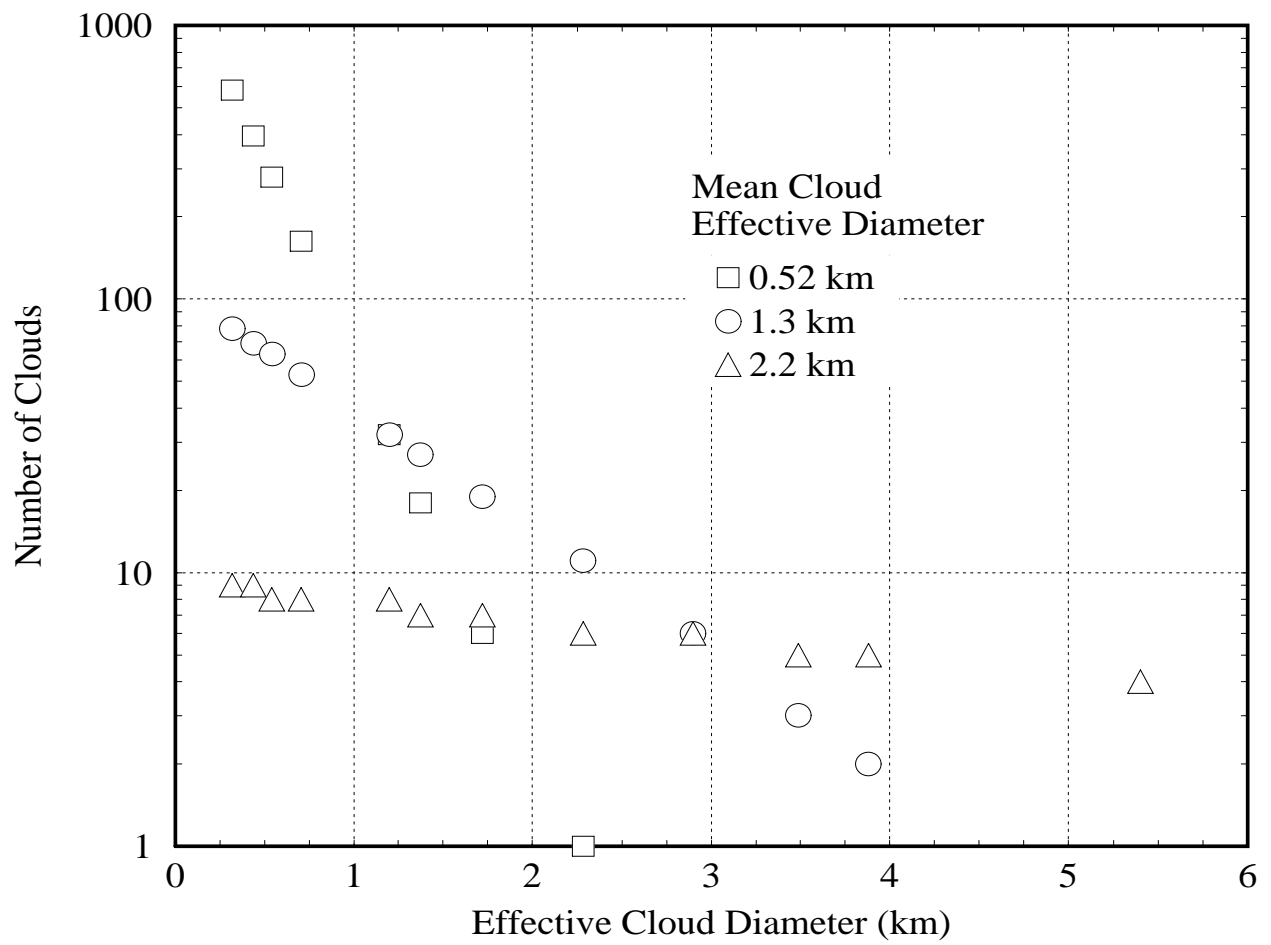


Figure 6.4 Cloud number density distributions for various mean cloud diameters.

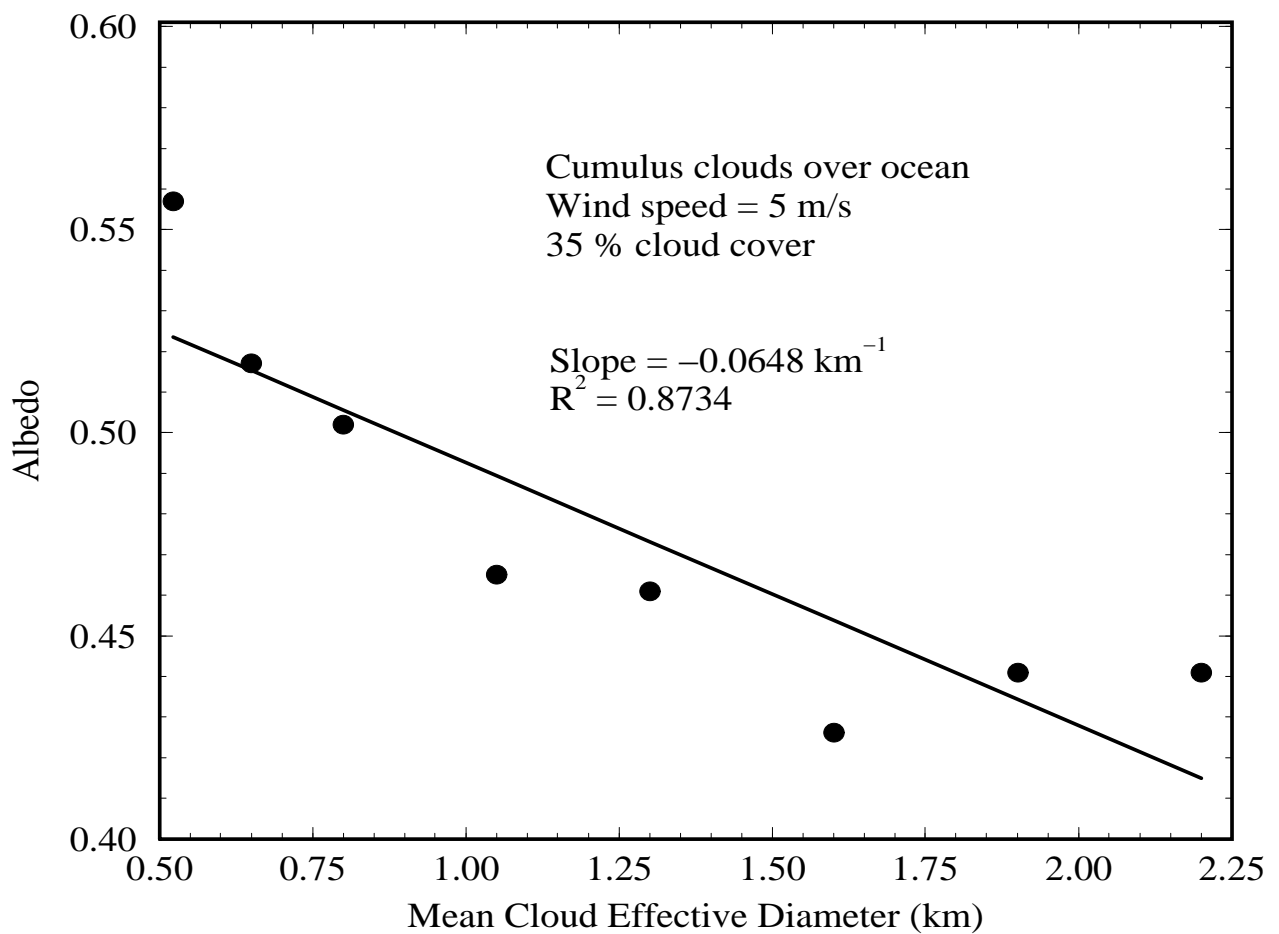


Figure 6.5 Albedo versus mean cloud diameter for 35 percent cloud cover, 45 deg solar angle and an ocean surface.

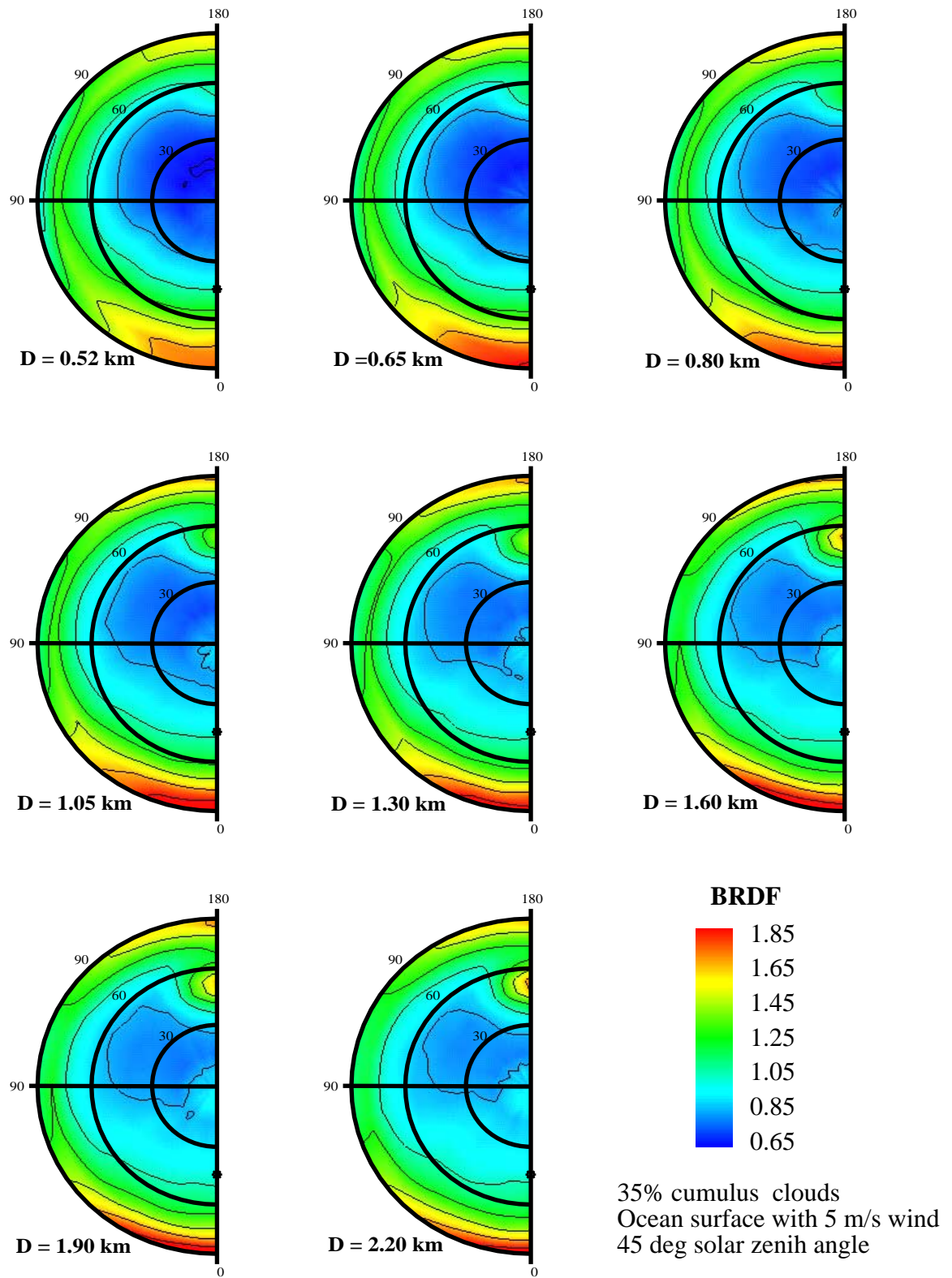


Figure 6.6 BRDF results for variation of mean cloud size for 35 percent cumulus cloud cover, 45 deg solar zenith angle and an ocean surface with 5 m/s wind speed.

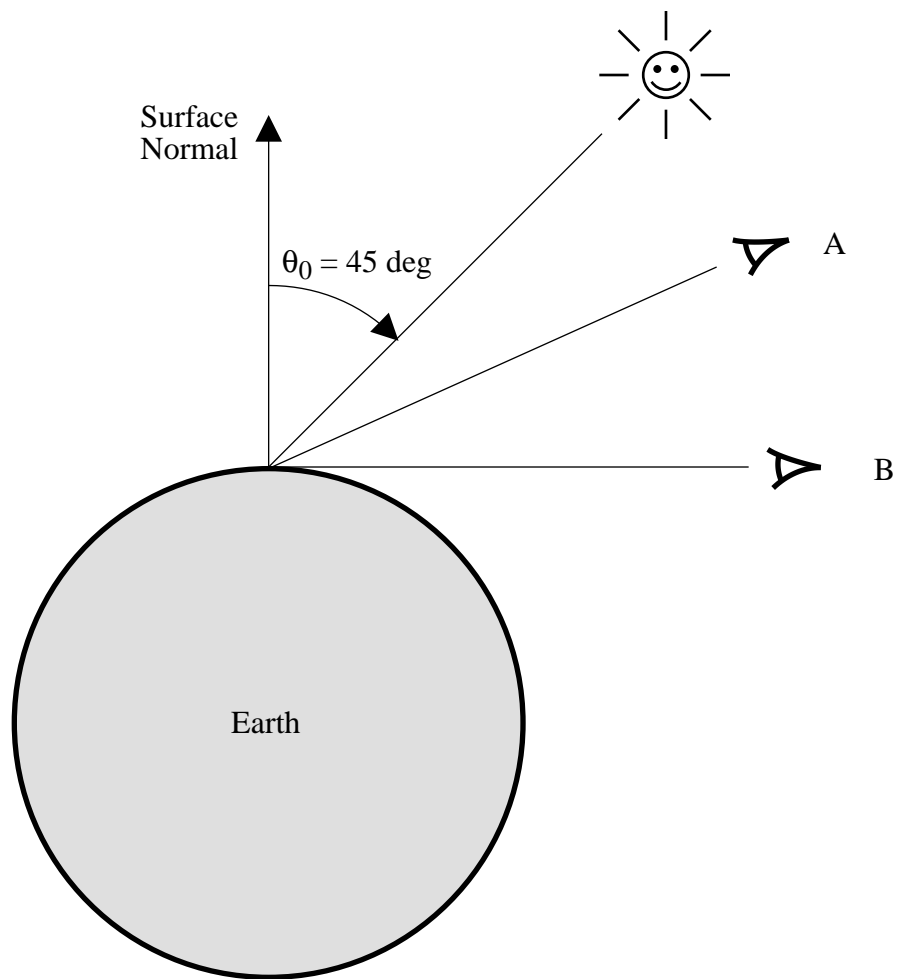


Figure 6.7 Limb brightening implies that view B is "brighter" than view A.

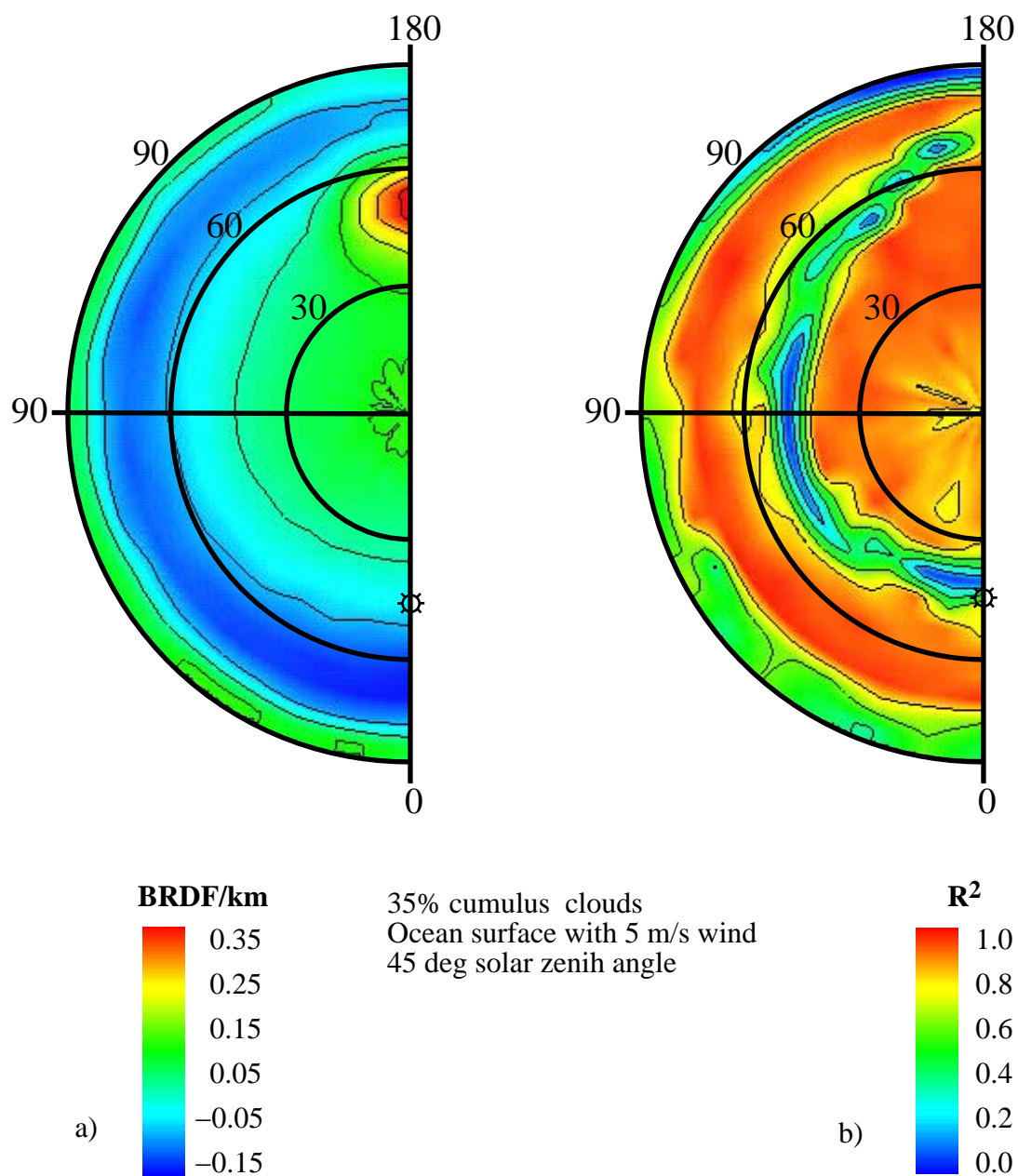


Figure 6.8 BRDF sensitivity to cloud size (a) and correlation coefficient (b) for 35 percent cumulus cloud cover, 45 deg solar zenith angle and ocean surface with 5 m/s wind speed

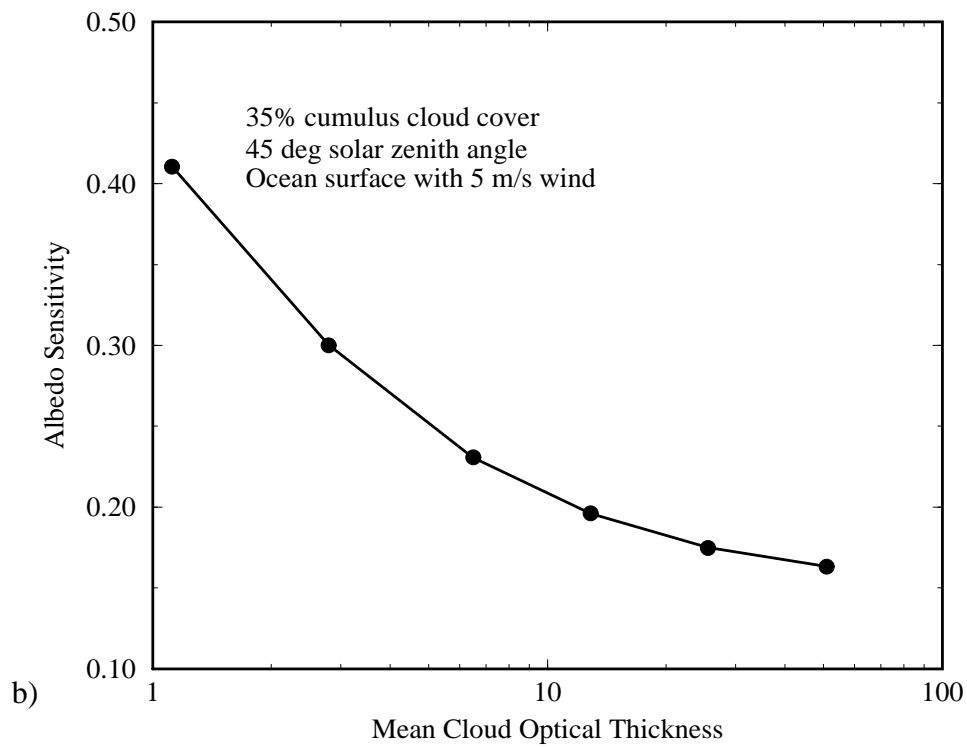
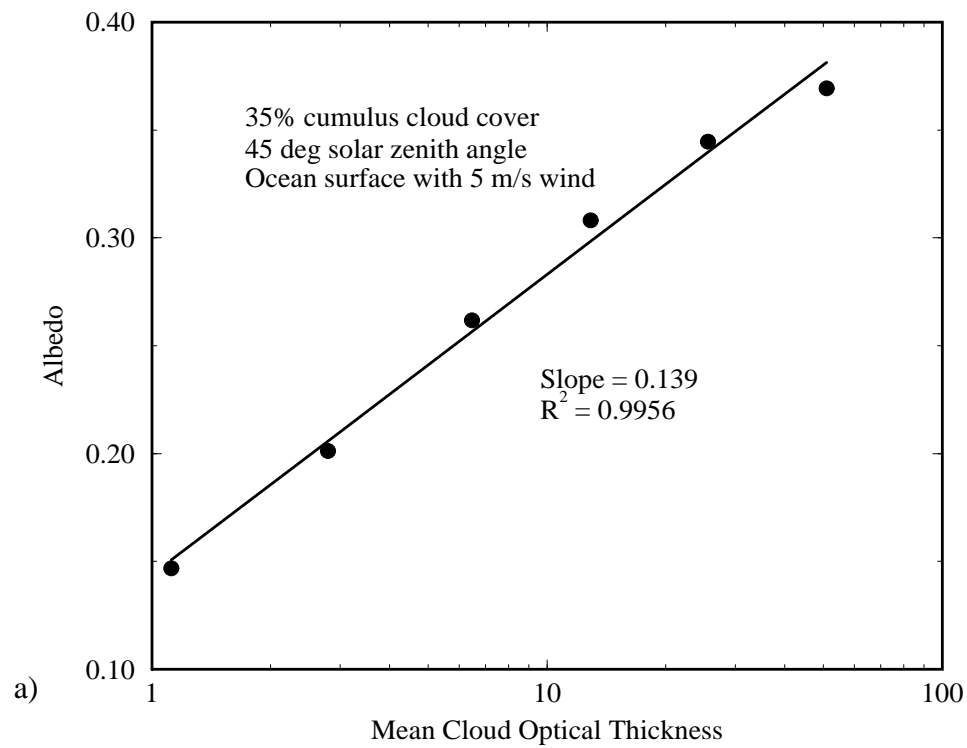


Figure 6.9 Scene (a) albedo and (b) albedo sensitivity to optical thickness as a function of cloud optical thickness for 35 percent cloud cover and 45 deg solar angle.

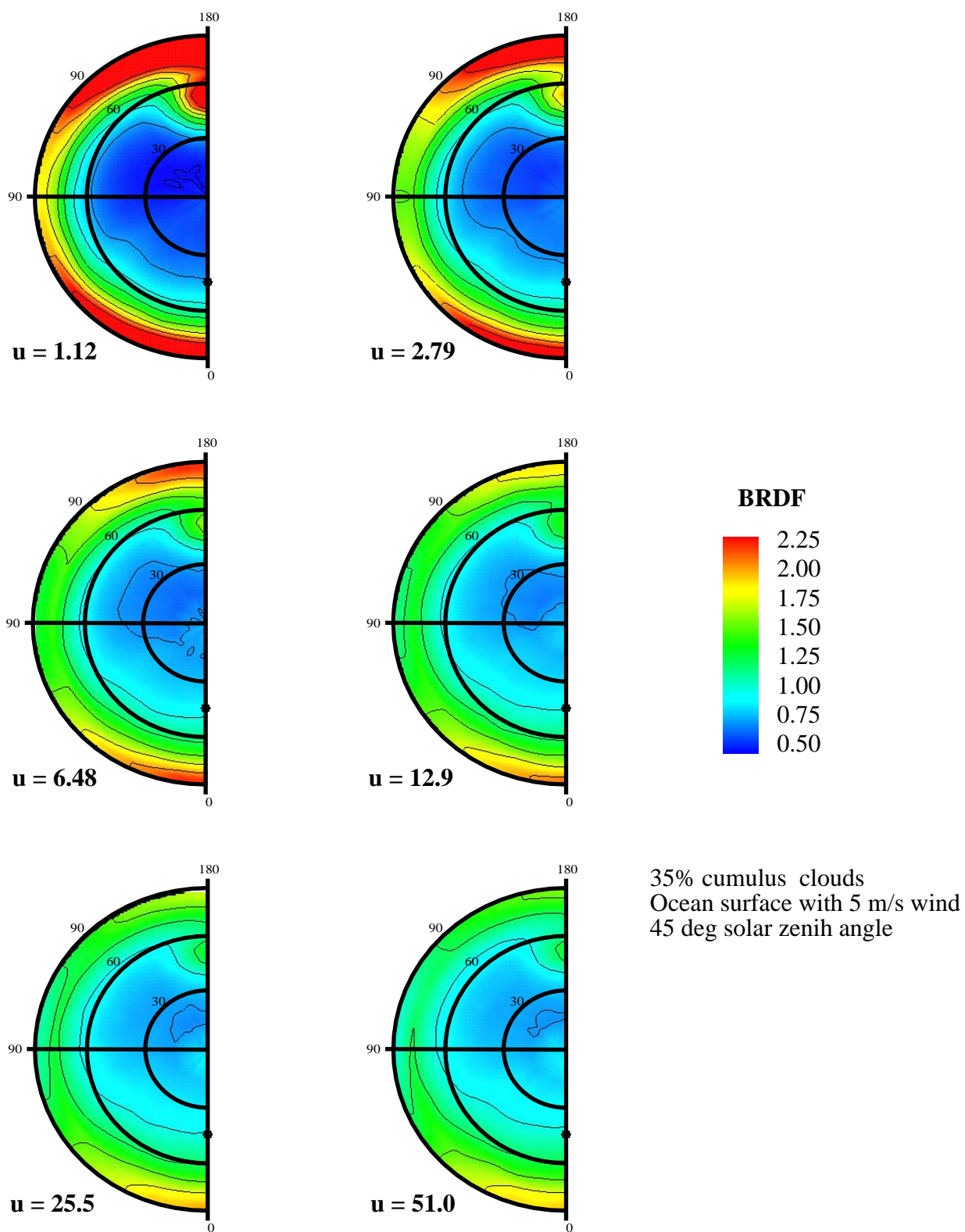


Figure 6.10 BRDF results for variation in mean cloud optical thickness for 35 percent cloud cover, 45 deg solar angle and an ocean surface.

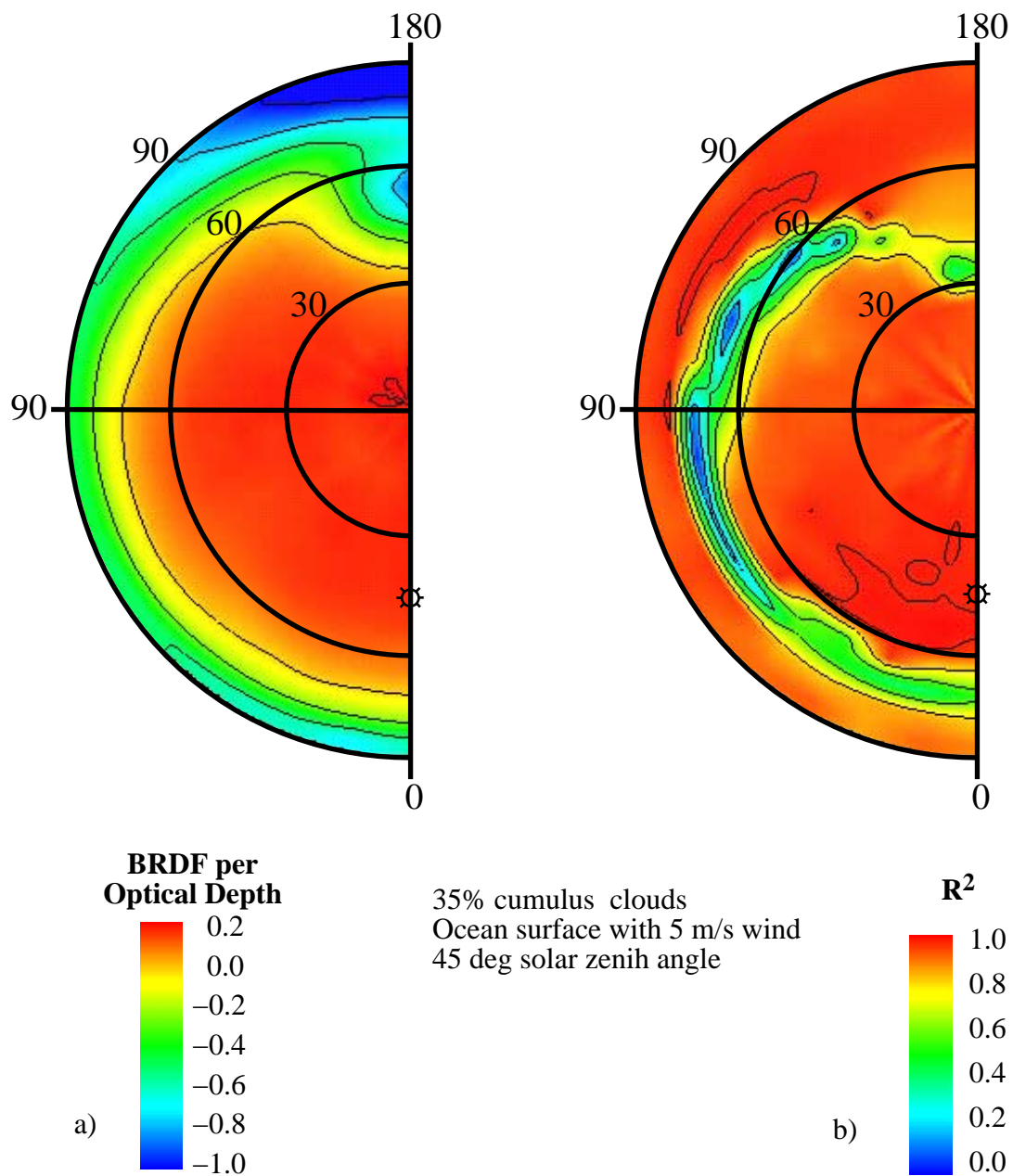


Figure 6.11 (a) BRDF sensitivity parameter and (b) correlation coefficient for 35 percent cloud cover, 45 deg solar zenith angle and ocean surface.

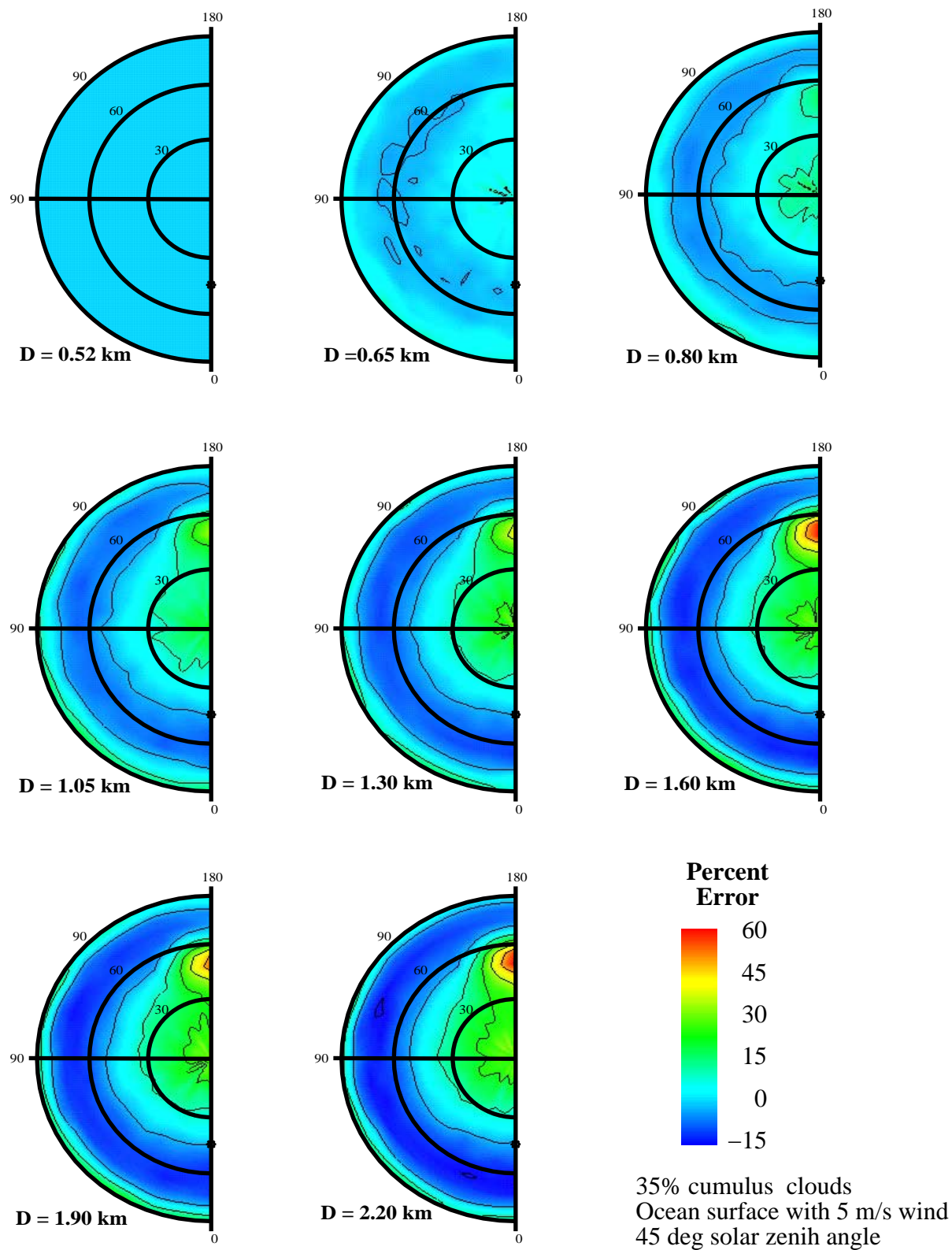


Figure 6.12 Flux retrieval error with cloud size variation for 35 percent cloud cover, 45 deg solar zenith angle and an ocean surface.

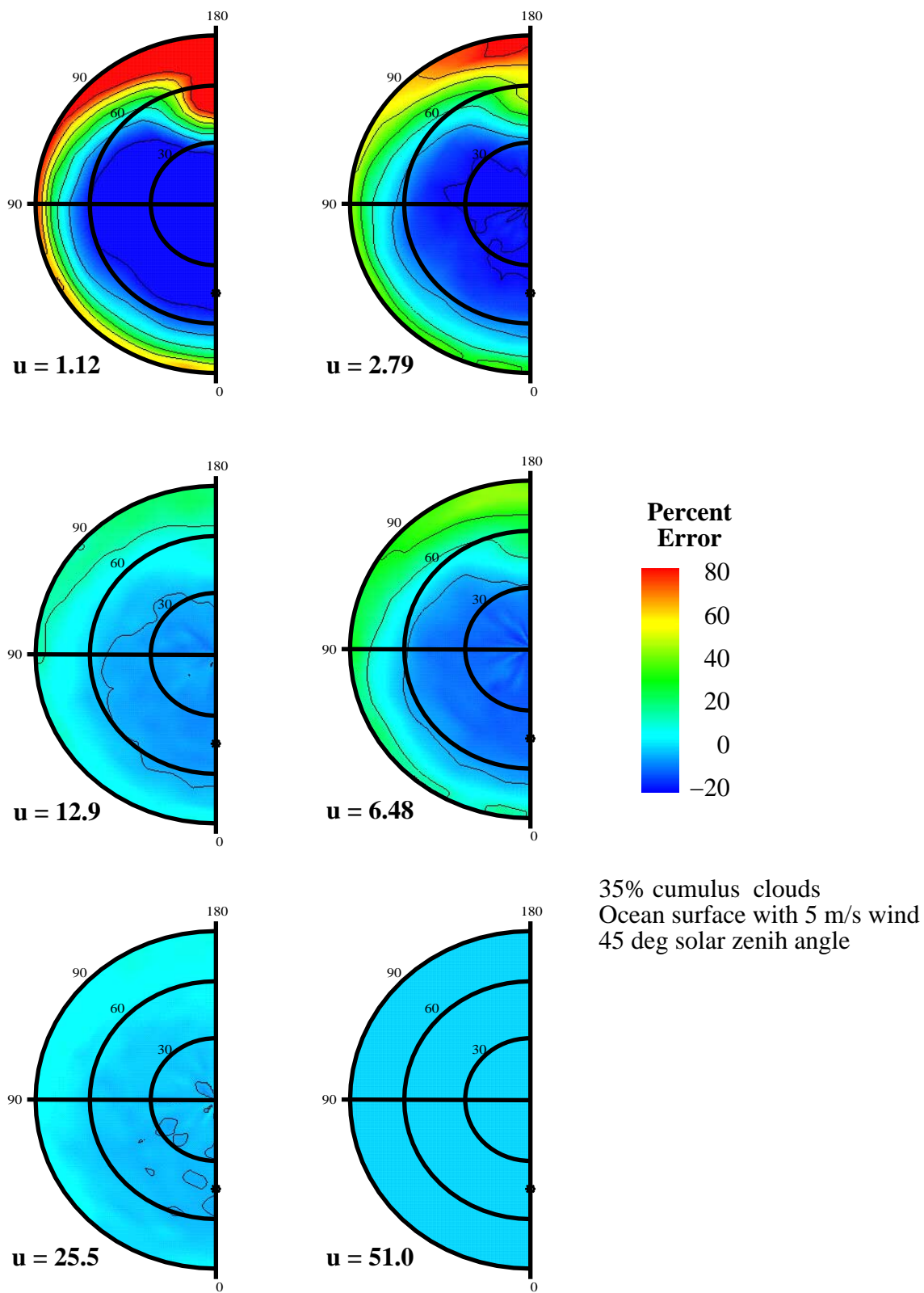


Figure 6.13 Flux retrieval error for cloud optical thickness variation for 35 percent cloud cover, 45 deg solar angle and an ocean surface.

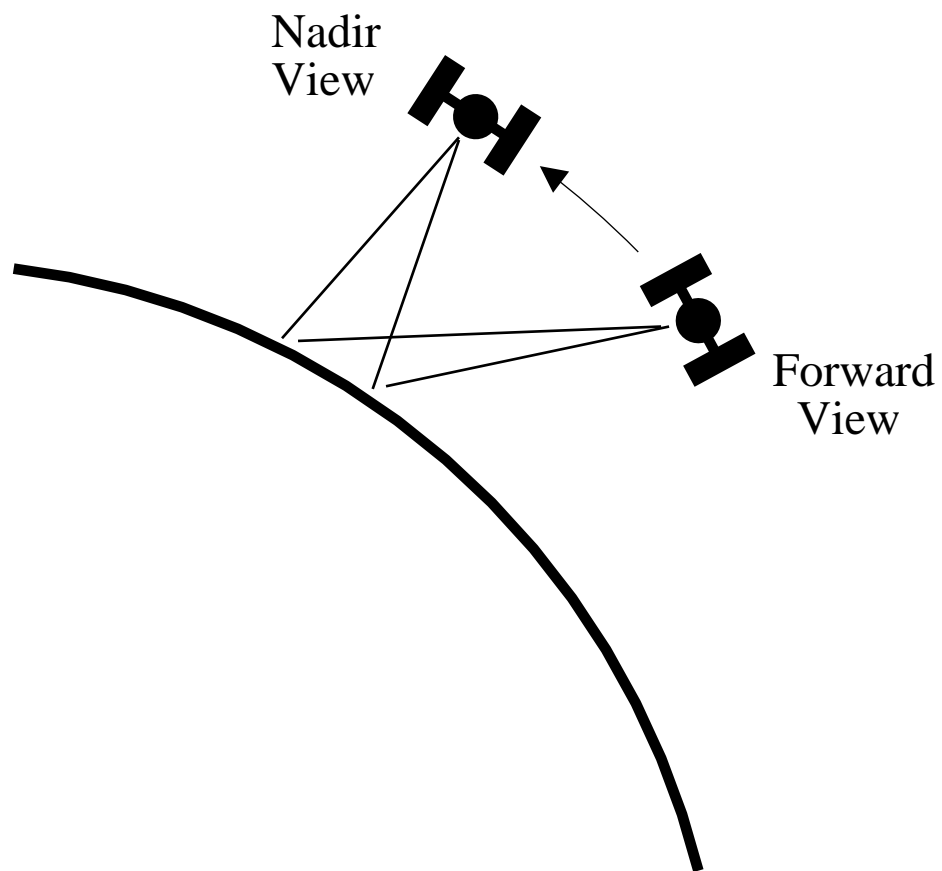


Figure 6.14 The ATSR earth-viewing geometry.

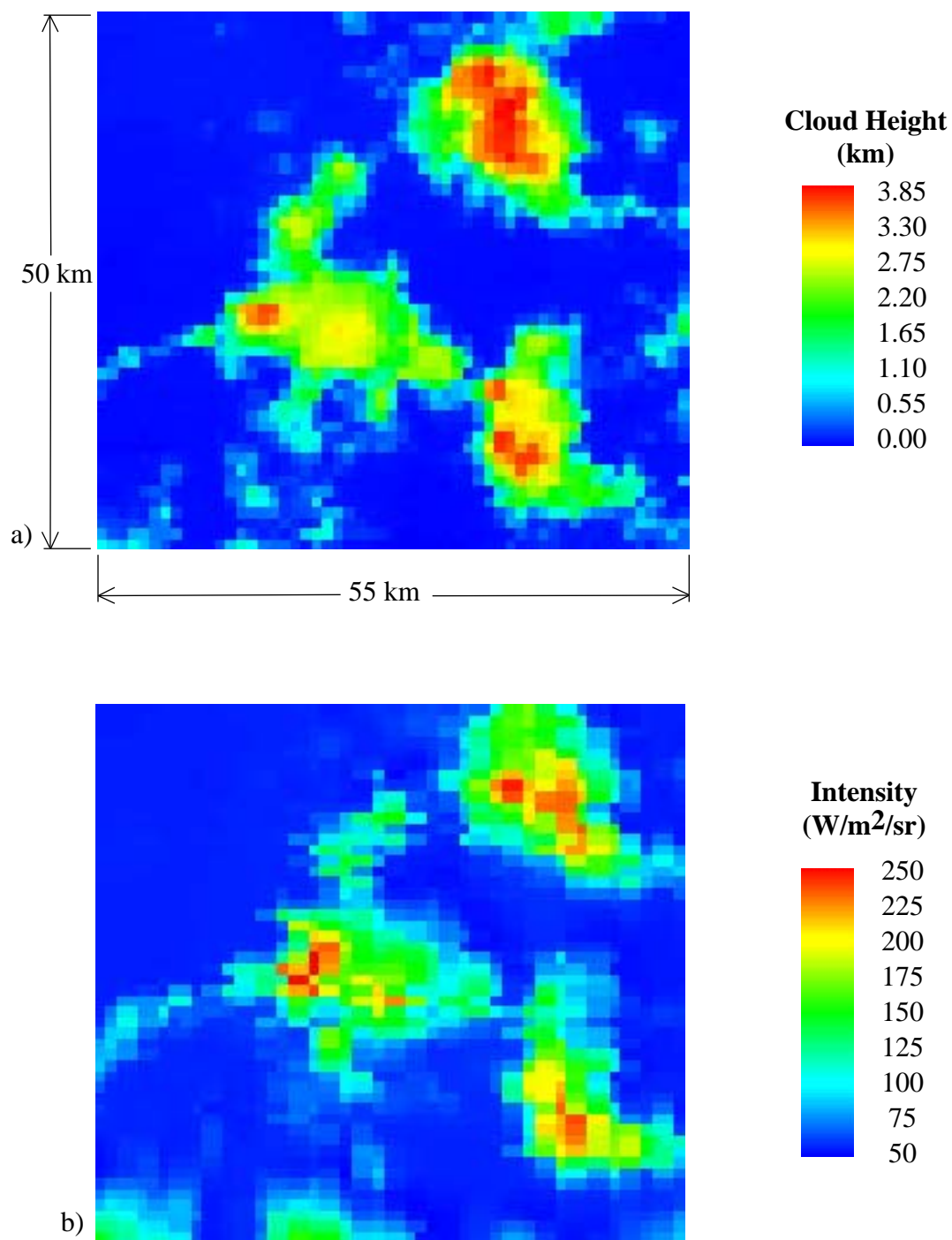


Figure 6.15 The ATSR imager data showing (a) cloud height from the 11 μm thermal channel and (b) forward view from 0.55 μm channel.

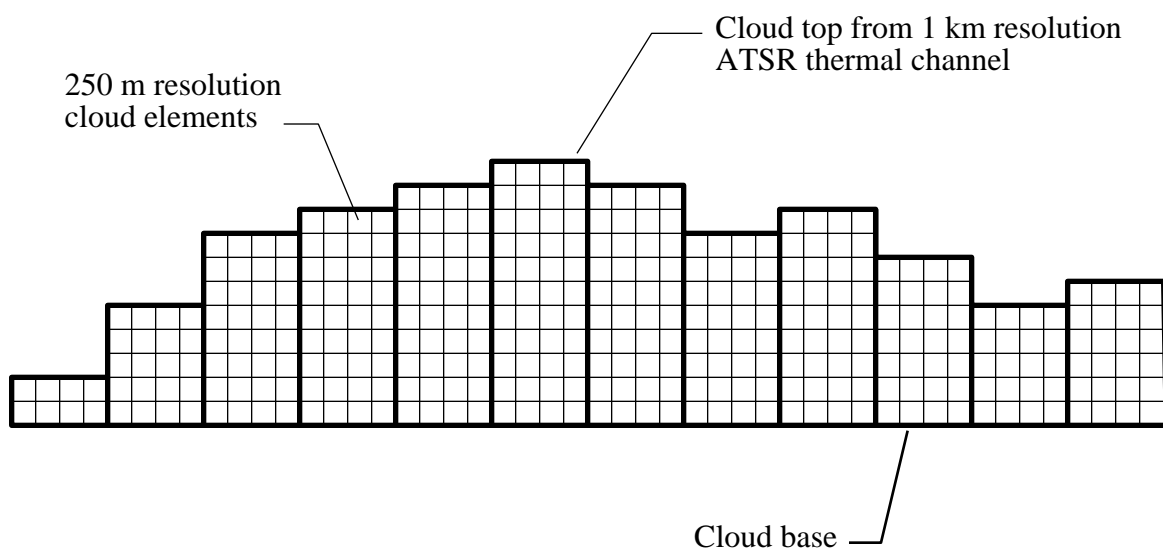
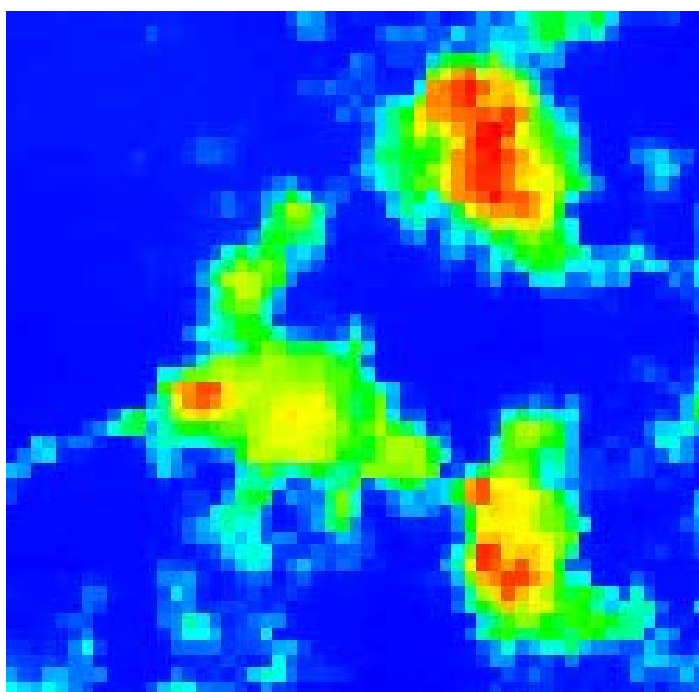
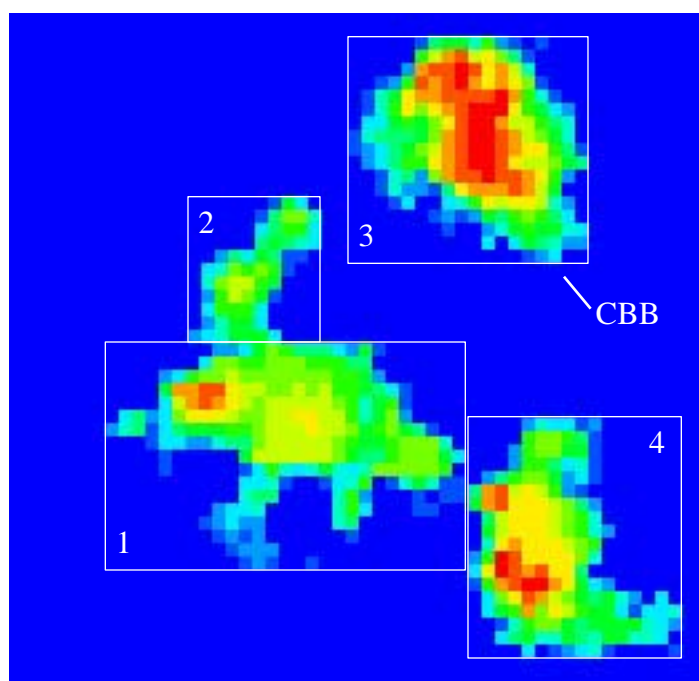


Figure 6.16 Construction of a cloud from ATSR cloud-top height information.



a)



b)

Figure 6.17 The (a) ATSR cloud field and the (b) corresponding model cloud field showing cloud bounding boxes (CBB).

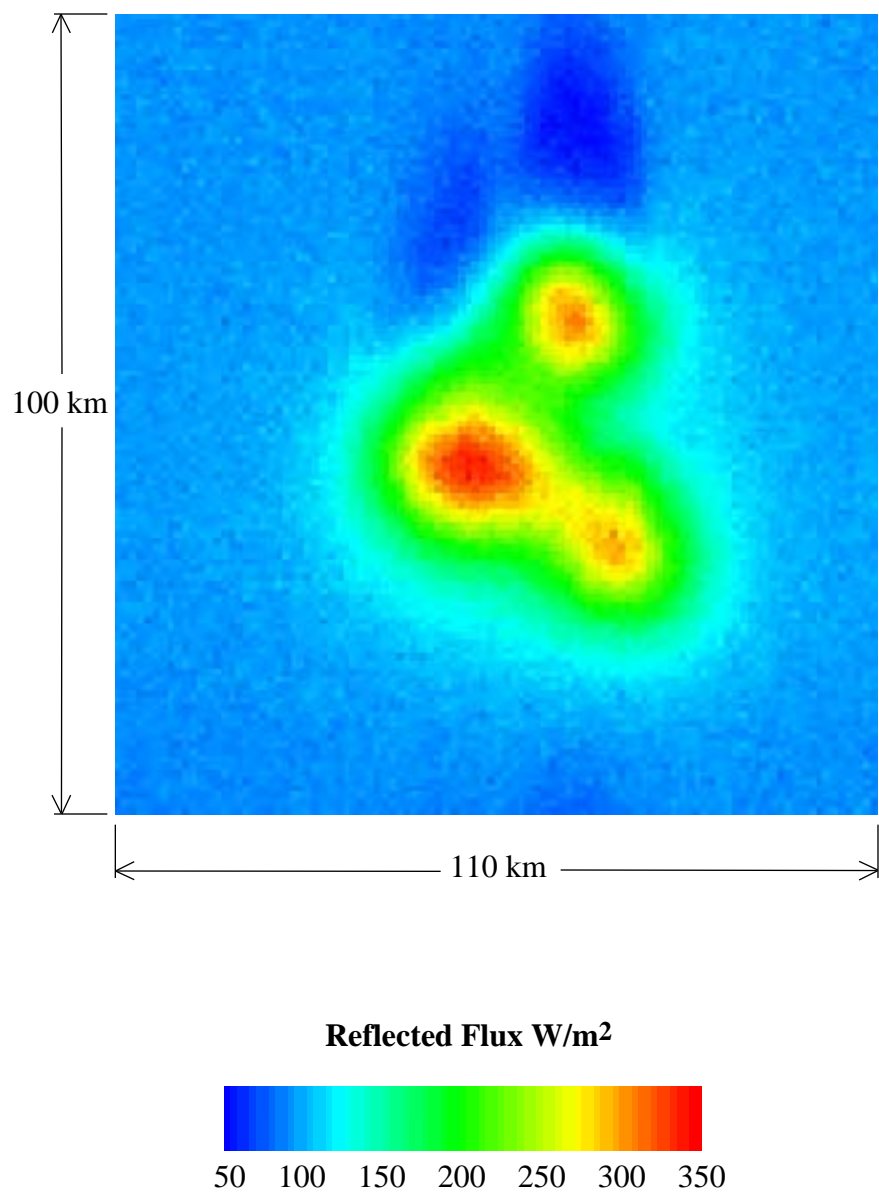


Figure 6.18 Predicted reflected flux distribution from ATSR model cloud field.

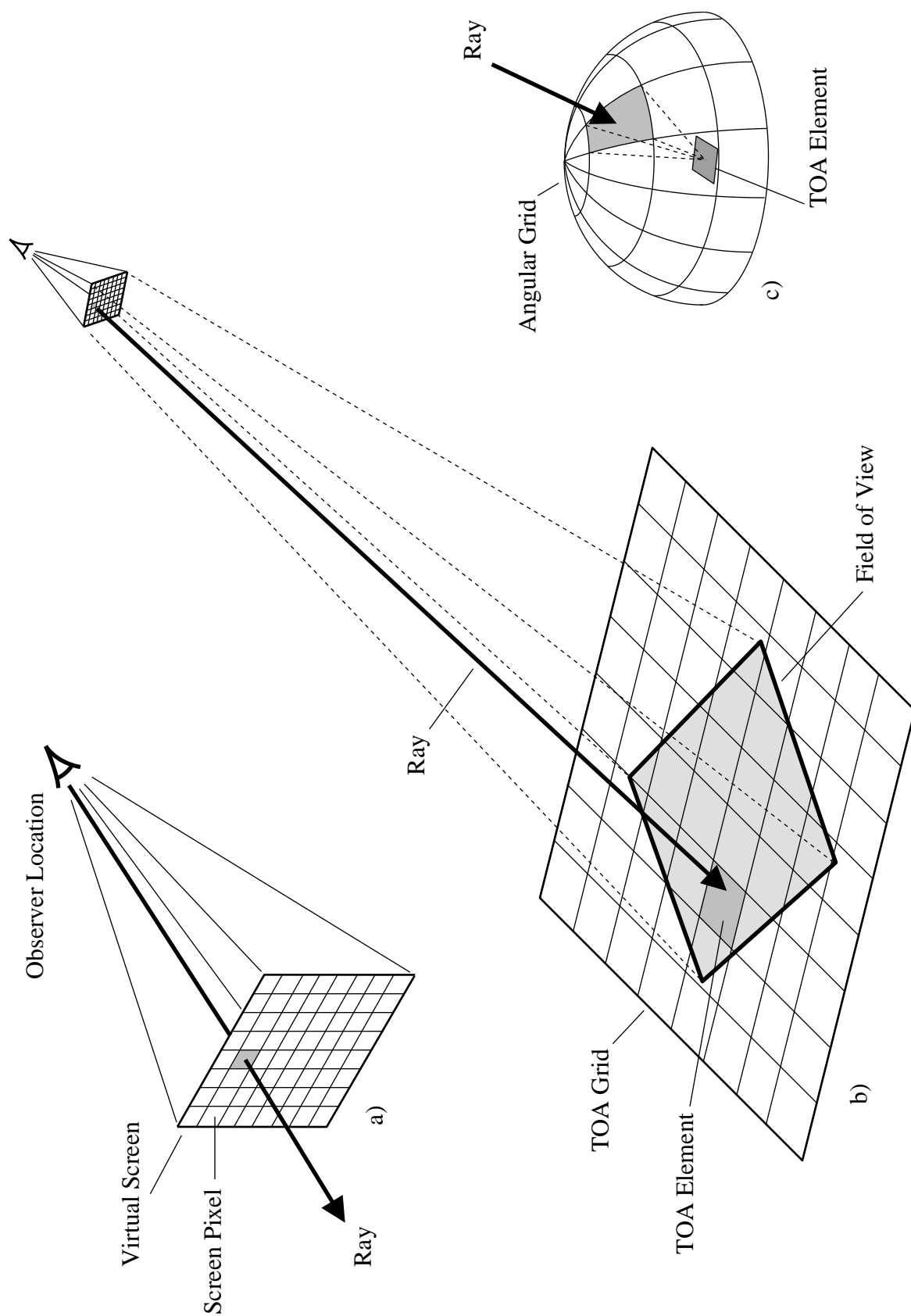
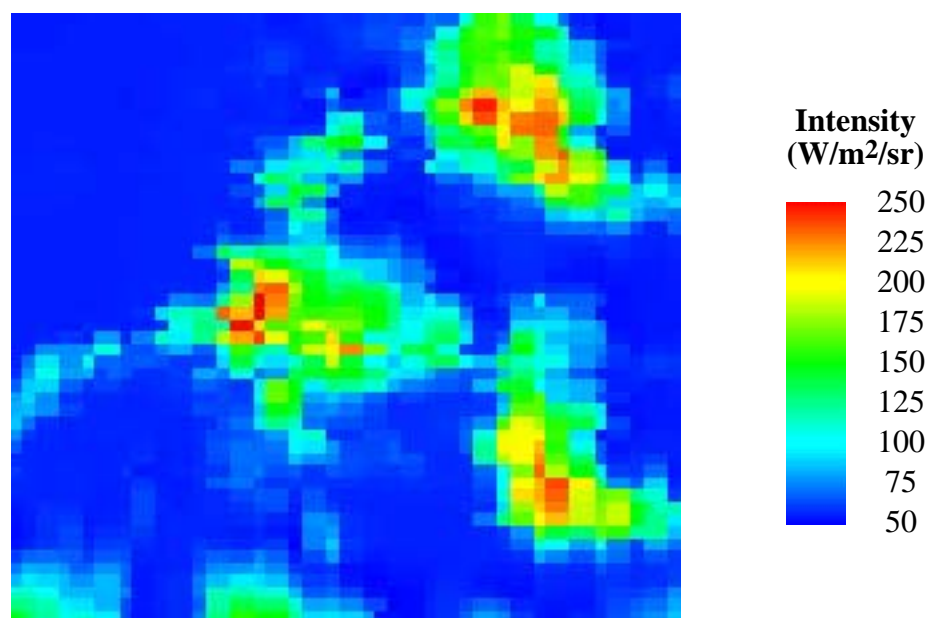
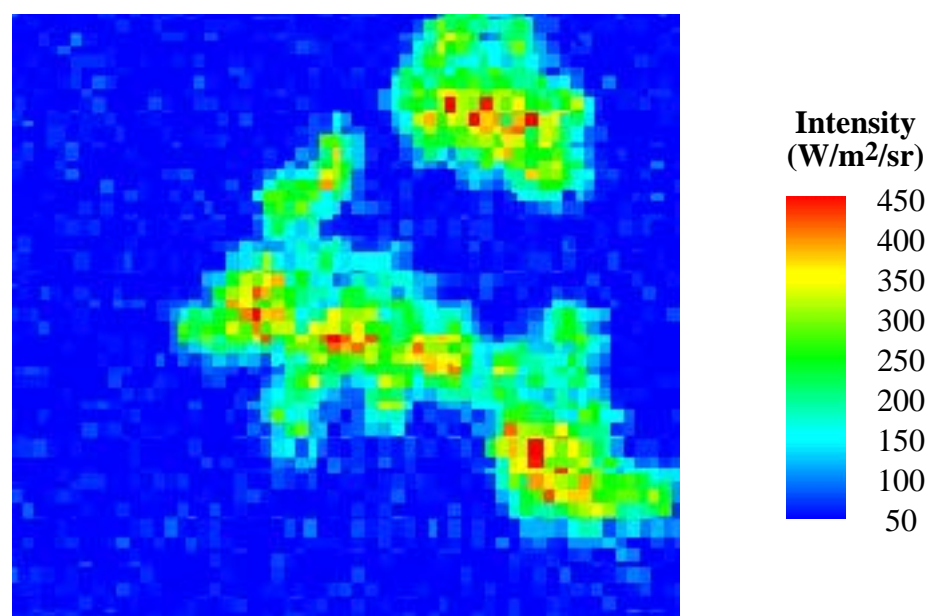


Figure 6.19 Virtual screen geometry showing (a) ray passing through screen pixel and (b) arriving at the TOA grid through (c) a radiation field angular bin.

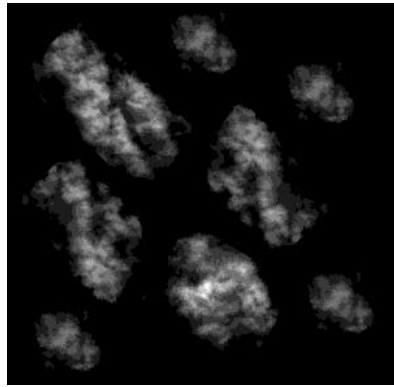


a)

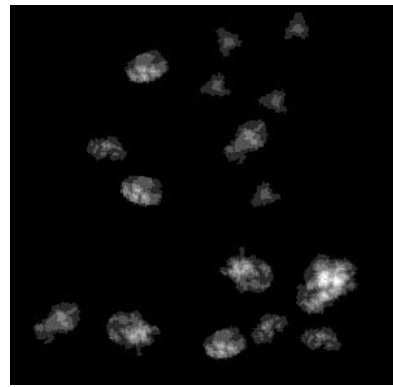


b)

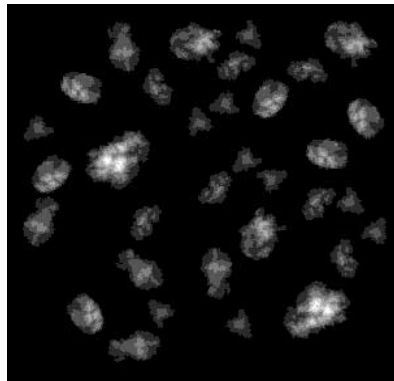
Figure 6.20 Comparison of (a) ATSR forward view with (b) the corresponding model-predicted view.



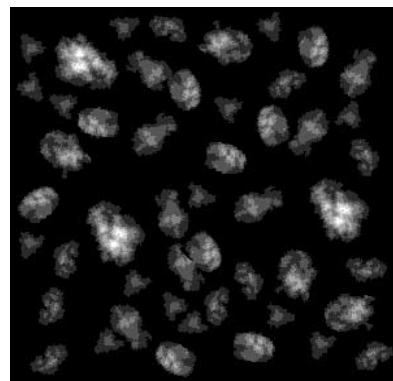
a) 30 percent Stratocumulus



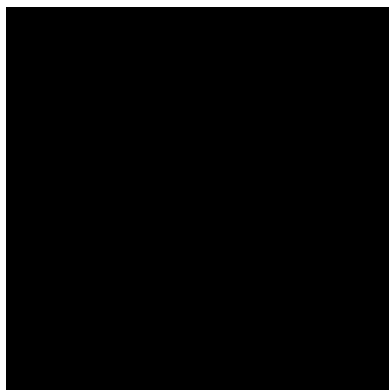
b) 10 percent Cumulus



c) 20 percent Cumulus



d) 30 percent Cumulus



e) Clear sky

Figure 6.21 Five cloud scenes used to create larger mosaic scenes.

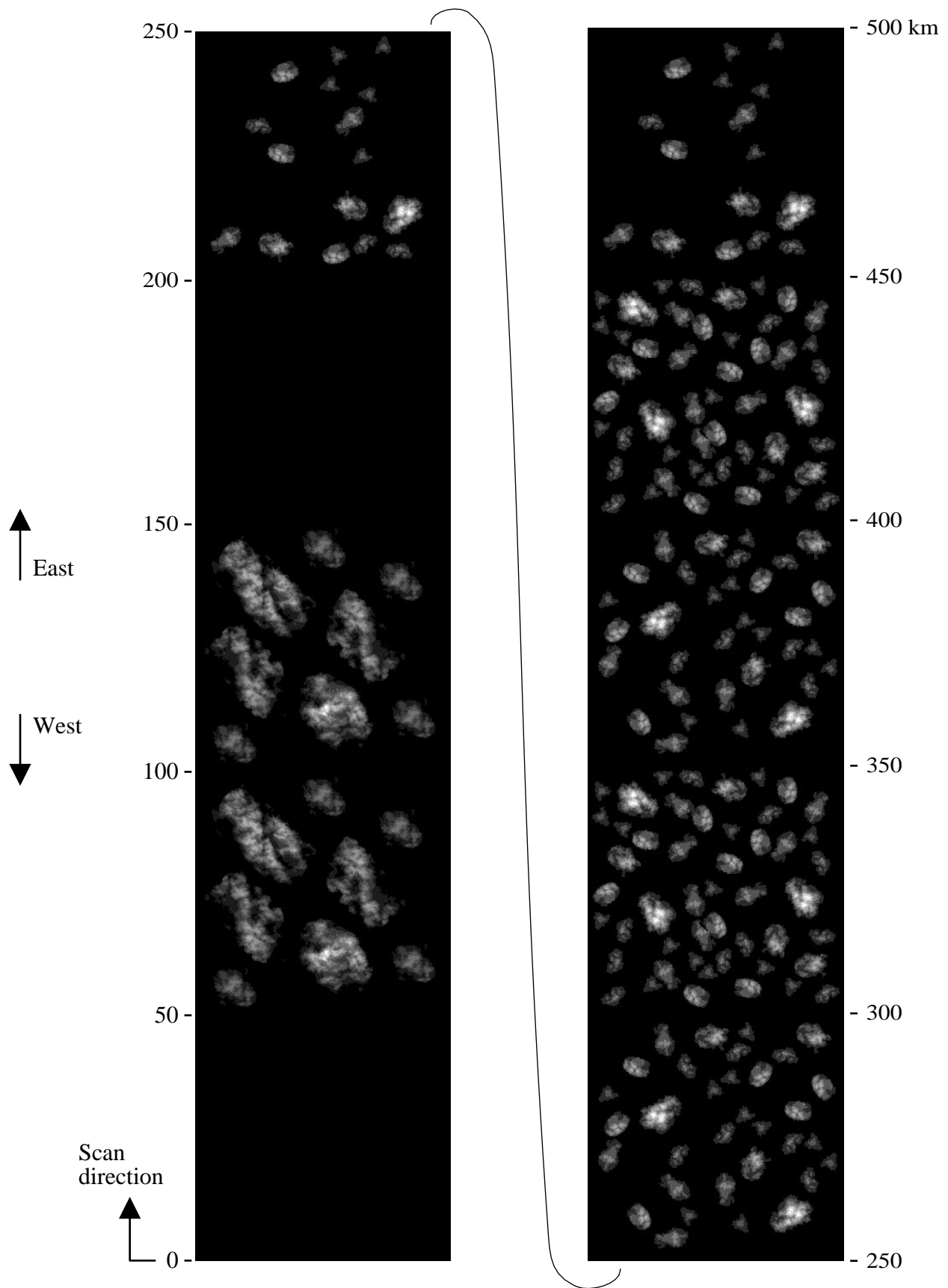


Figure 6.22 Mosaic scene constructed from sequences of individual scenes of cumulus and stratocumulus clouds over an ocean surface..

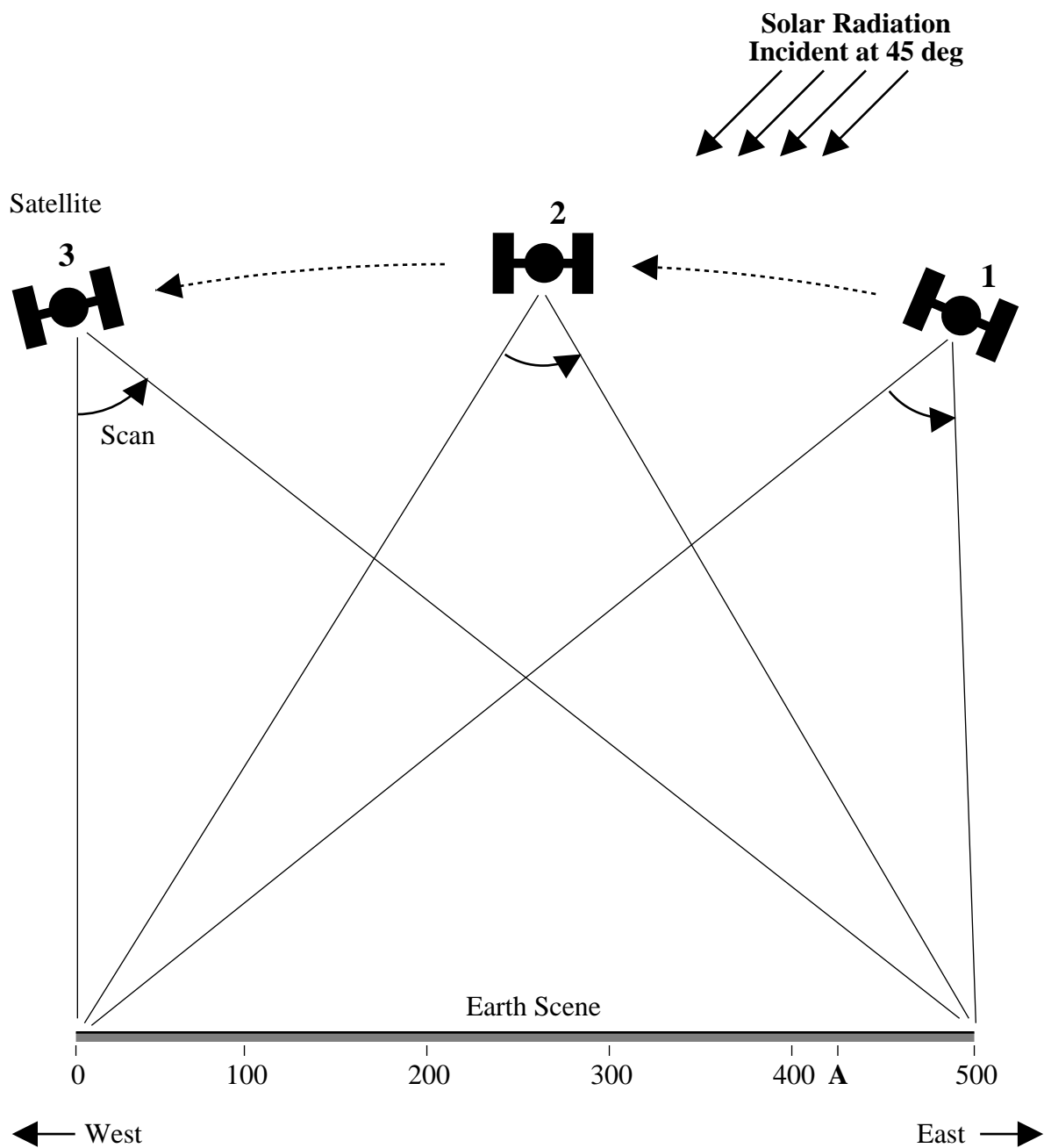


Figure 6.23 Schematic representation of a radiometer scanning a 500-km earth scene from three different 800 km altitude orbital positions.

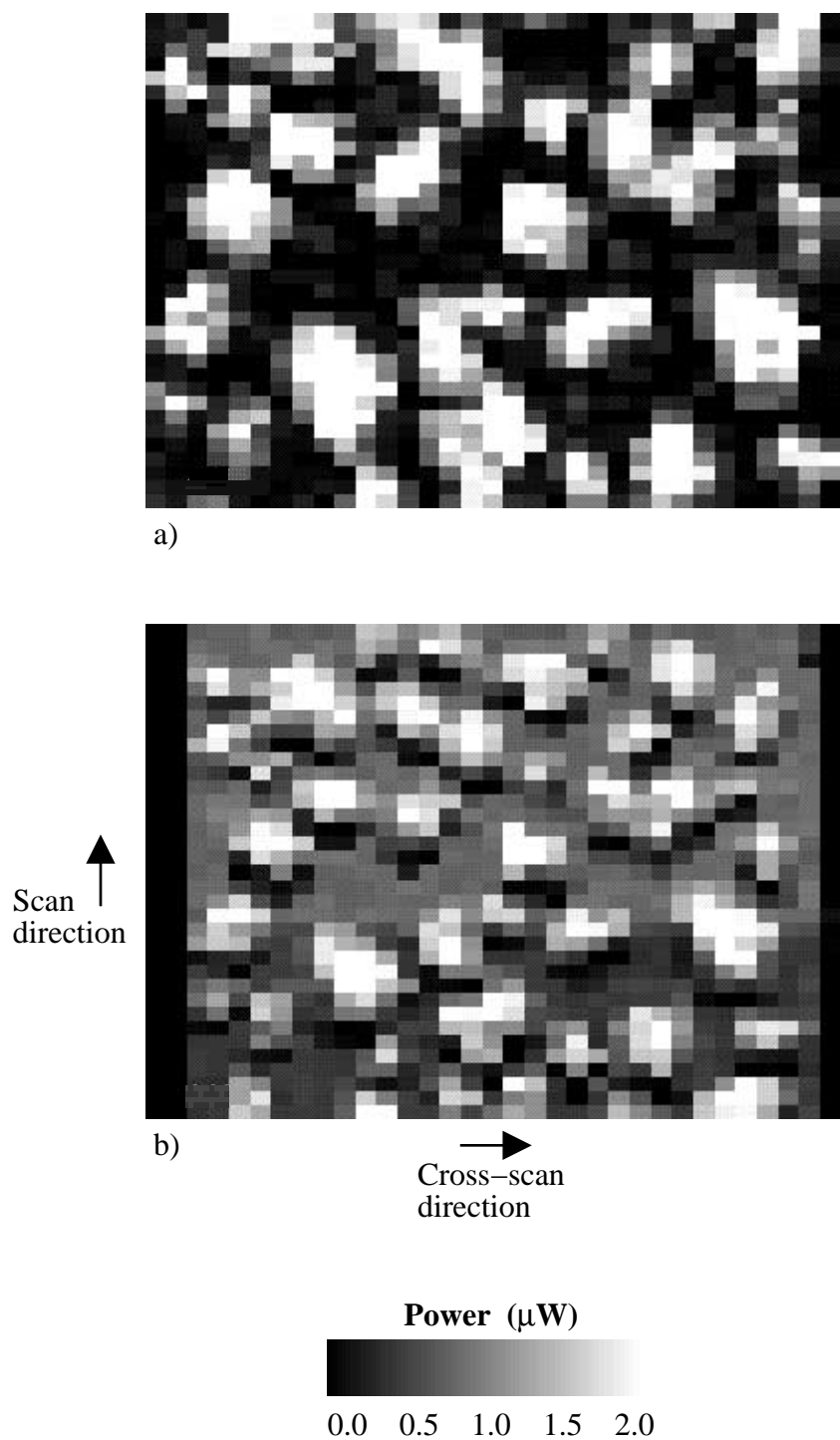


Figure 6.24 Power fields incident to instrument aperture from a TOA position of 425 km input to the CERES optical model from orbits (a) 1 and (b) 3.

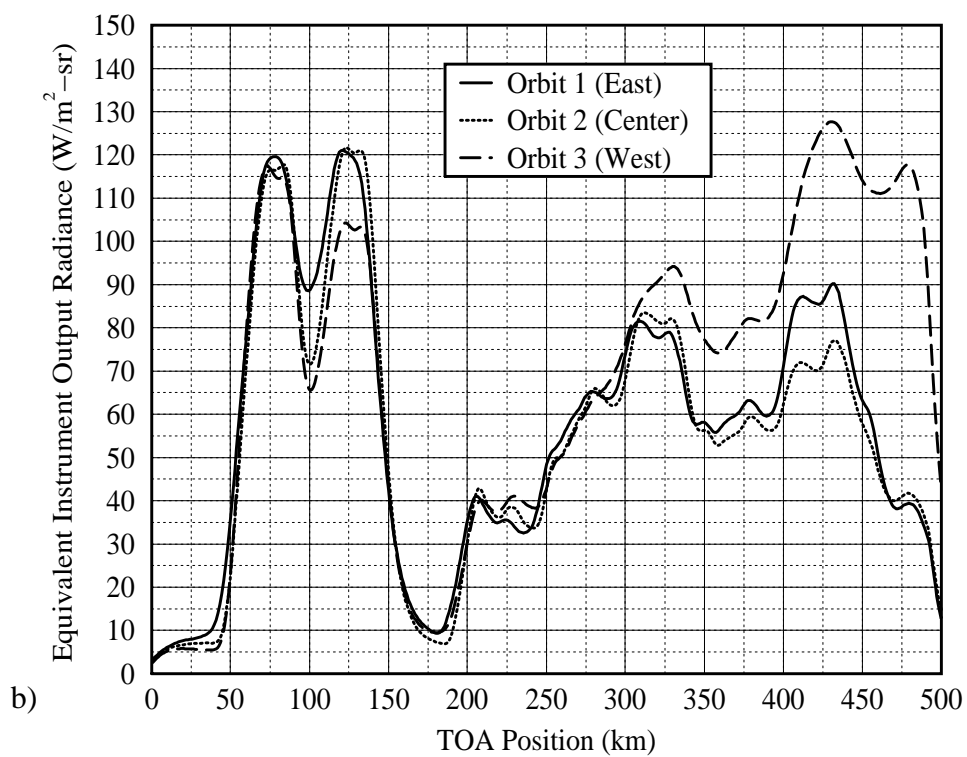
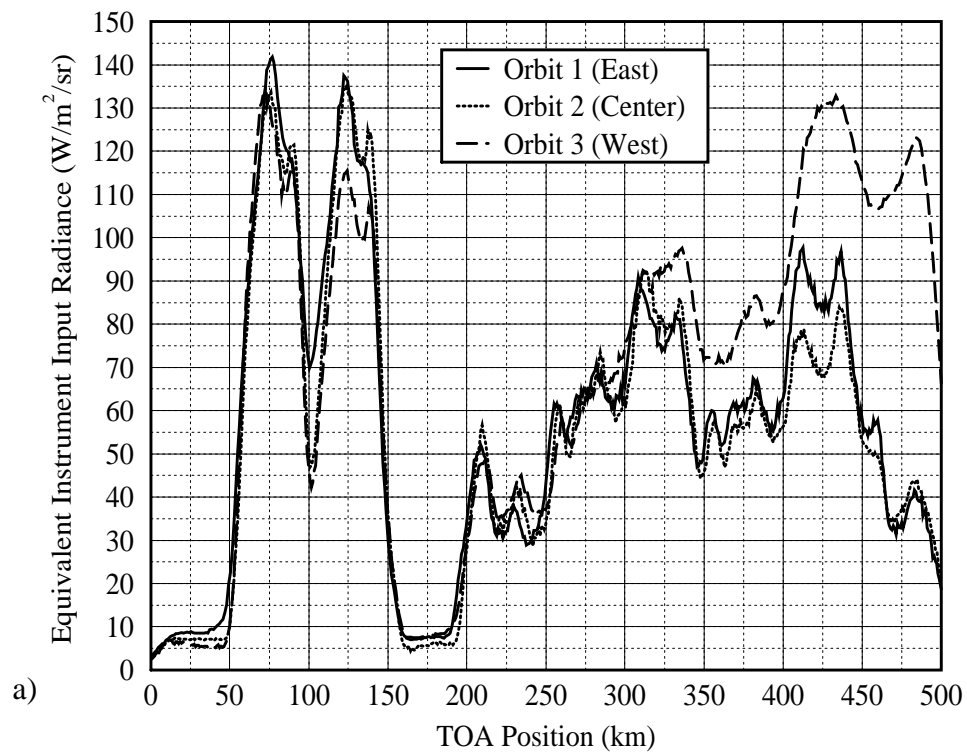


Figure 6.25 (a) Equivalent incident intensity and (b) calibrated instrument response.

References

Abbot, C.G., (1920) "The Larger Opportunities for Research on the Relations of Solar and Terrestrial Radiation," *Proceedings of the National Academy of Science in the United States of America*, Vol. 6, pp. 82 - 95.

Ahrens, C.D., (1991) **Meteorology Today: an Introduction to Weather, Climate, and the Environment**, 4th ed., West Publishing Co.

Aida, M., (1976) "Scattering of Solar radiation as a Function of Cloud Dimension and Orientation," *Journal of Quantitative Spectroscopy and Radiation Transfer*, Vol. 17, pp. 303 - 310.

Anonymous, (1976) **U.S. Standard Atmosphere**, United States Committee on Extensions to the Standard Atmosphere, U.S. Government Printing Office.

Arking, A., and S. Vemury, (1984) "The Nimbus-7 ERB Data Set, A Critical Analysis," *Journal of Geophysical Research*, Vol. 89, pp. 5089 - 5097.

Barkstrom, B.R., and J.B. Hall Jr, (1982) "Earth Radiation Budget Experiment (ERBE): An Overview," *J. Energy*, vol. 6, no. 2, pp. 141 - 146..

Bayazitoglu, Y., and J. Higenyi, (1979) "The Higher-Order Differential Equations of Radiative Transfer: P_3 Approximation," *AIAA Journal*, Vol. 17, No. 4, pp. 424 - 431.

Bongiovi, R.P., (1993) **A Parametric Study of the Radiative and Optical Characteristics of a Scanning Radiometer for Earth Radiation Budget Applications Using the Monte-Carlo Method**, Master of Science Thesis, Virginia Polytechnic Institute and State University.

Cess, R.D., (1976) "Climate Change: An Appraisal of Atmospheric Feedback Mechanism Employing Zonal Climatology," *Journal of Atmospheric Science*, Vol. 33, pp. 1831 - 1843.

Cess, R.D. and G.L. Potter, (1988) "A Methodology for Understanding and Intercomparing Climate Feedback Processes in General Circulation Models," *Journal of Geophysical Research*, Vol. 93, pp. 8305 - 8314.

Cess, R.D, et al, (1989) "Interpretation of Cloud-Climate Feedback as Produced by 14 Atmospheric General Circulation Models," *Science*, Vol. 245, pp. 513 - 516.

Cess, R.D., M.H. Zhang, P. Minnis, L. Corsetti, E.G. Dutton, B.W. Forgan, D.P. Garber, W.L. Gates, J.J. Hack, E.F. Harrison, X. Jing, J.T. Kiehl, C.N. Long, J.J. Morcrette, G.L. Potter, V. Ramanathan, B. Subasilar, C.H. Whitlock, D.F. Young, Y. Zhou, (1995) "Absorption of Solar Radiation by Clouds: Observations Versus Models," *Science*, Vol. 267, pp. 496 - 499.

Chapman, D.D., (1992) **A Monte-Carlo Simulation of Jet Exhaust Nozzle Thermal Radiative Signatures**, Master of Science Thesis, Virginia Polytechnic Institute and State University.

Charlock, T.P. and V. Ramanathan, (1985) "The Albedo Field and Cloud Radiative Forcing Produced by a General Circulation Model with Internally Generated Cloud Optics," *Journal of Atmospheric Science*, Vol. 42, pp. 1408 - 1429.

Claussen, M. (1982) "On the Radiative Interaction in Three-Dimensional Cloud Fields, *Beitr. Phys. Atmos.*, Vol. 55, pp. 158 - 169.

Cox, C and W. Munk, (1954a) "Measurement of the Roughness of the Sea from Photographs of the Sun's Glitter," *Journal of the Optical Society of America*, Vol. 44, No. 11, pp. 838 - 850.

Cox, C and W. Munk, (1954b) "Statistics of the Sea Surface Derived from Sun Glitter," *Journal of Marine Research*, Vol. 13, pp. 199 - 227.

Cox, C and W. Munk, (1955) "Some Problems in Optical Oceanography," *Journal of Marine Research*, Vol. 14, pp. 63 - 78.

Davies, R., (1978) "The Effect of Finite Geometry on the Three Dimensional Transfer of Solar Irradiance in Clouds," *Journal of Atmospheric Science*, Vol. 35, pp. 1712 - 1725.

Davies, R., (1984) "Reflected Solar Radiances from Broken Cloud Scenes and the Interpretation of Measurements," *Journal of Geophysical Research*, Vol. 89, No. D1, pp. 1259 - 1266.

Deirmendjian, D., (1969) **Electromagnetic Scattering on Spherical Polydispersions**, Elsevier, New York.

Eskin, L.D., (1981) **Application of the Monte-Carlo Method to the Transient Thermal Modeling of a Diffuse-Specular Radiometer Cavity**, Master of Science Thesis, Virginia Polytechnic Institute and State University.

Flamant, P., G. Brogniez, M. Desbois, Y. Fouquart, J.F. Flobert, J.C. Vanhoutte, and U. Nat Singh, (1989) "High Altitude Cloud Observations by Ground-Based Lidar, Infrared Radiometer and Meteosat Measurements," *Annales Geophysicae*, Vol. 7, pp. 1 - 10.

Fouquart, Y., J.C. Buriez, and M. Herman, (1990) "The Influence of Clouds on Radiation: A Climate Modeling Perspective," *Reviews of Geophysics*, Vol. 28, pp. 145 - 166.

Green, R.N., B.A. Wielicki, J.A. Coakley, III, L.L. Stowe, and P.O. Hinton, (1994) "CERES Inversion to Instantaneous TOA Fluxes", *CERES Algorithm Theoretical Basis Document*, Subsystem 4.5.

Gube, M., J. Schmetz, and E. Raschke, (1980) "Solar Radiative Transfer in a Cloud Field" *Beitr. Phys. Atmos.*, Vol. 1, pp. 24 - 34.

Haeffelin, M.P., (1993) **A Numerical Study of Equivalence in Scanning Thermistor Bolometer Radiometers for Earth Radiation Budget Applications**, Master of Science Thesis, Virginia Polytechnic Institute and State University.

Haeffelin, M.P., (1996) **Error Propagation Through Radiometric Channels and Subsequent Interpretation of Data**, Doctor of Philosophy Dissertation, Virginia Polytechnic Institute and State University.

Halton, J.H., (1970) "A Retrospective Survey of the Monte Carlo Method," *SIAM Review*, Vol. 12, No. 1, pp. 1 - 63.

Harshvardhan, (1982) "The Effect of Brokenness on Cloud-Climate Sensitivity," *Journal of Atmospheric Science*, Vol. 39, pp. 1853 - 1861.

Hartmann, D.L. and D.A. Short, (1980) "On the Use of Earth Radiation Budget Statistics to Studies of Clouds and Climate," *Journal of Atmospheric Science*, Vol. 37, pp. 1233 - 1250.

Hartmann, D.L. and V. Ramanathan, A. Berroir, and G.E. Hunt, (1986) "Earth radiation Budget data and Climate Research," *Reviews of Geophysics*, Vol. 24, pp. 439 - 468.

Hansen, J.E., (1971) "Multiple Scattering of Polarized Light in Planetary Atmospheres. Part II: Sunlight Reflected by Terrestrial Water Clouds," *Journal of Atmospheric Science*, Vol. 28, pp. 1400 - 1426.

House, F.B., A. Gruber, G.E. Hunt, and A.T. Mecherikunnel, (1986) "History of Satellite Missions and Measurements of the Earth Radiation Budget (1057 - 1984)," *Reviews of Geophysics*, Vol. 24, No. 2, pp. 357 - 377.

Hunt, G.E., K. Robert, A.T. Mecherikunnel, (1986) "A History of Presatellite Investigation of the Earth's Radiation Budget," *Reviews of Geophysics*, Vol. 24, No. 2, pp. 351 - 356.

James, F., (1990) "A Review of Pseudorandom Number Generators," *Computer Physics Communications*, Vol. 60, pp. 329 - 344.

Kandel, S.R., (1994) "Earth Radiation Balance and Climate: Why the Moon is the Wrong Place to Observe the Earth," *Advances in Space Research*, Vol. 14, No. 6, pp. 223 - 232.

Kite, A., (1987) "The Albedo of Broken Cloud Fields," *Quarterly Journal of the Royal Meteorological Society*, Vol. 113, pp. 513 - 531.

Kopia, L.P., and R.B. Lee, (1990) "Earth Radiation Budget Experiment (ERBE) Scanner Instrument," **Long Term Monitoring of the Earth's Radiation Budget**, SPIE Proceedings Series, Vol. 1299, pp. 27 - 39.

Liou, K.N., (1985) "Influence of Cirrus Clouds on Weather and Climate Processes: A Global Perspective," *Monthly Weather Review*, Vol. 114, pp. 1167 - 1199.

Liou, K.N., (1992) **Radiation and Cloud Processes in the Atmosphere**, Oxford University Press, 487 pp.

Levi, B.G., (1995) "Clouds Cast a Shadow of Doubt on Model of Earth's Climate," *Physics Today*, Vol. 48, No. 5, pp. 21 - 23.

Meekins, J.L., (1990) **Optical Analysis of the ERBE Scanning Thermistor Bolometer Radiometer Using the Monte-Carlo Method**, Master of Science Thesis, Virginia Polytechnic Institute and State University.

Mahan, J.R. and L.D. Eskin, (1984) "The Radiation Distribution Factor - It's calculation Using Monte-Carlo and An Example of It's Application," **First U.K. National Heat Transfer Conference**, Yorkshire, England, July 4 - 6.

McCartney, E.J., (1976) **Optics of the Atmosphere: Scattering by Molecules and Particles**, John Wiley & Sons, New York, 408 pp.

McKee, T.B. and S.K. Cox, (1974) "Scattering of Visible Radiation by Finite Clouds," *Journal of Atmospheric Science*, Vol. 31, pp. 1885 - 1892.

Meekins, J.L., (1990) **Optical Analysis of the ERBE Scanning Thermistor Bolometer Radiometer Using the Monte-Carlo Method**, Master of Science Thesis, Virginia Polytechnic Institute and State University.

Mie, G., (1908) "Beiträge zur Optik Tüber Medien, Speziell Kolloidaler Metallösungen", *Ann. Physik*, Vol. 25, pp. 377 - 445.

Minnis, P., P.W. Heck, D.F. Young, C.W. Fairall, and B.J. Snider, (1992) "Stratocumulus Cloud Properties Derived from Simultaneous Satellite and Island-Based Instrumentation During FIRE," *Journal of Applied Meteorology*, Vol. 31, p. 317.

Modest, M.F. (1990) "The Improved Differential Approximation in Radiative Transfer in Multidimensional Media," *Journal of Heat Transfer*, Vol. 112, No. 3, pp. 819 - 821.

Ohring, G. and P. Clapp, (1980) "The Effect of Change in Cloud Amount on the Net Radiation at the Top of the Atmosphere," *Journal of Atmospheric Science*, Vol. 37, pp. 447 - 454.

Nguyen, T.K. (1994) **Optimization of Radiometric Channel Solar Calibration for the Clouds and the Earth's Radiant Energy System (CERES) Using the Monte-Carlo Method**, Master of Science Thesis, Virginia Polytechnic Institute and State University.

Parol, F., J.C. Buriez, D. Crétel, Y. Fouquart, (1994) "The Impact of Cloud Inhomogeneities on the Earth Radiation Budget: the 14 October 1989 I.C.E. Convective Cloud Case Study," *Annales Geophysicae*, Vol. 12, pp. 240 - 253.

Plank, V.G., (1969) "The Size Distribution of Cumulus Clouds in Representative Florida Populations," *Journal of Applied Meteorology*, Vol. 8, pp. 46 - 67.

Priesendorf, R.W. and R.L. Stephens, (1984) "Multimode Radiative Transfer in Finite Optical Media, I, Fundamentals," *Journal of Atmospheric Science*, Vol. 41, pp. 709 - 724.

Priestley, K.J., J.R. Mahan, T.K. Nguyen, M.P. Haeffelin, (1995) "Numerical Simulation of Ground Calibration of the CERES Thermistor Bolometer Radiometers," EOS/SPIE European Symposium on Satellite Remote Sensing II, Paris, France, September 25-29.

Ramanathan, V., R.D. Cess, E.F. Harrison, P. Minnis, B.R. Barkstrom, E. Ahmad, and D. Hartmann, (1989a) "Cloud-Radiative Forcing and Climate: Results from the Earth Radiation Budget Experiment," *Science*, Vol. 243, pp. 1 - 140.

Ramanathan, V. and B.R. Barkstrom, and E.F. Harrison, (1989b) "Climate and the Earth's Radiation Budget," *Physics Today*, Vol. 42, pp. 22 - 32.

Raschke, E., T.H. Vonder Haar, M. Pasternak, and W.R. Bandeen, (1973) "The Radiation Balance of the Earth-Atmosphere System from Nimbus 3 Radiation Measurements," NASA TN D-7249, 73 pp., NTIS N7321702.

Schneider, W.H., (1972) "Cloudiness as a Global Climatic Feedback Mechanism: The Effects of the Radiation Balance and Surface Temperature of Variations in Cloudiness," *Journal of Atmospheric Science*, Vol. 29, pp. 1413 - 1422.

Schuster, G., (1995) NASA Langley Research Center, Atmospheric Sciences Division, Radiation Sciences Branch, Personal Communication, June.

Seigel, R. and Howell J.R. (1992) **Thermal Radiation Heat Transfer**, 3rd ed., Hemisphere Publishing Corp., Washington, D.C.

Smith, G.L., D. Rutan, and T.D. Bess, (1992) "Atlas of Albedo and Absorbed Radiation Derived from Nimbus 7 Earth Radiation Budget Data Set - November 1985 to October 1987," NASA Reference Publication 1281.

Stephens, G.L., and T.J. Greenwald, (1991) "The Earth's Radiation Budget and its relation to Atmospheric Hydrology. 2. Observations of Cloud Effects," *Journal of Geophysical Research*, Vol. 96, pp. 15325 - 15340.

Suomi, V.E., (1957) "The Radiation Balance of the Earth from a Satellite," *American International Geophysical Year*, Vol. 6, pp. 331 - 340.

Suttles, J.T., R.N. Green, P. Minnis, G.L. Smith, W.F. Staylor, B.A. Wielicki, I.J. Walker, D.F. Young, V.R. Taylor, L.L. Stowe, (1988) "Angular Radiation Models for Earth-Atmosphere System. Part I: Shortwave Radiation," NASA Reference Publication 1184, Vol. 1.

Suttles, J.T., R.N. Green, G.L. Smith, B.A. Wielicki, I.J. Walker, V.R. Taylor, L.L. Stowe, (1989) "Angular Radiation Models for Earth-Atmosphere System. Part II: Longwave Radiation," NASA Reference Publication 1184, Vol. 2.

Suttles, J.T., B.A. Wielicki, and S. Vemury, (1992) "Top of the Atmosphere Radiative Fluxes: Validation of ERBE Scanner Inversion Algorithm Using Nimbus-7 ERB Data," *Journal of Applied Meteorology*, Vol. 31, pp. 784 - 796.

Taylor, V.R., and L.L. Stowe, (1984) "Reflectance Characteristics of Uniform Earth and Cloud Surfaces Derived from Nimbus 7 ERB," *Journal of Geophysical Research*, Vol. 89, No. D4, June 4, pp. 4987 - 4996.

Tira, N.E., (1991) **A Study of the Thermal and Optical Characteristics of Radiometric Channels for Earth Radiation Budget Applications**, Doctor of Philosophy Dissertation, Virginia Polytechnic Institute and State University.

Turk, J.A., (1994) **Acceleration Techniques for the Radiative Analysis of General Computational Fluid Dynamic Solutions Using Reverse Monte-Carlo Ray Tracing**, Doctor of Philosophy Dissertation, Virginia Polytechnic Institute and State University.

van de Hulst, H.C., (1981) **Light Scattering by Small Particles**, Dover Publications, Inc., New York.

Villeneuve, P.V. and J.R. Mahan, (1995) "Sensitivity of Earth-Atmospheric Bidirectional Reflectivity Functions to Variations in Cloud Parameters," EOS/SPIE European Symposium on Satellite Remote Sensing II, Paris, France, September 25-29.

Villeneuve, P.V., D.D. Chapman, and J.R. Mahan, (1994) "Use of the Monte-Carlo Ray-Trace Method as a Design Tool for Jet Engine Infrared Visibility Suppression," 6th AIAA/ASME Thermophysics and Heat Transfer Conference, Colorado Springs, Colorado, June 20-23.

Walkup, M., (1996) **A Study of Earth Radiation Budget Radiometric Channel Performance and Data Interpolations Protocols**, Master of Science Thesis, Virginia Polytechnic Institute and State University.

Watts, P., (1995), *Rutherford Appleton Laboratory*, Personal Communication.

Welch, R.M., and B.A. Wielicki, (1986) "The Stratocumulus Nature of Fog," *Journal of Climate and Applied Meteorology*, Vol. 25, pp. 101 - 111.

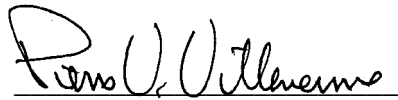
Welch, R.M., and W.G. Zdunkowski, (1986) "The Effect of Cloud Shape on Radiative Characteristics," *Beitr. Phys. Atmos.*, Vol. 54, pp. 482 - 491.

Wielicki, B.A and R.N. Green, (1989) "Cloud Identification for ERBE Radiation Flux Retrieval," *Journal of Applied Meteorology*, Vol. 28, pp. 1133 - 1146.

Wielicki, B.A., R.M. Welch, (1986) "Cumulus Cloud Properties Derived Using Landsat Satellite Data," *Journal of Climate and Applied Meteorology*, Vol. 25, pp. 261 - 276.

Vita

Pierre Villeneuve was born in Montreal, Québec, Canada on March 30, 1968. He spent most of his childhood near Cornwall, Ontario. On December 27, 1983, he moved with his family to Greeneville in the Volunteer state of Tennessee. He earned his Bachelor of Science degree in Mechanical Engineering from the University of Tennessee, Knoxville, in August of 1990. He then entered the graduate program at Virginia Polytechnic Institute and State University, Blacksburg, and completed his Master of Science degree in Mechanical Engineering in August of 1992. He continued at Virginia Tech to pursue his Doctor of Philosophy, which he completed in June, 1996. He was then hired by Los Alamos National Laboratory as a postdoctoral fellow to work in the area of remote sensing science.

A handwritten signature in black ink, reading "Pierre V. Villeneuve". The signature is written in a cursive style with a large initial "P" and "V".

Pierre V. Villeneuve